DISSERTATION

15 83

Simultaneous printing of tissue and customized bioreactor

Simultanes Drucken von Gewebe und angepasstem Bioreaktor

Doctoral thesis for a doctoral degree
at the Gradute School of Life Sciences (GSLS),
Julius-Maximilians-Universität Würzburg,
Section Biomedicine

submitted by
Marius E. Gensler
born in Bad Mergentheim

Würzburg 2022

Submitted on: ....

Members of the thesis committee:

Chairperson: Prof. Dr. rer. nat. Christian Janzen

Primary Supervisor: Prof. Dr.-Ing. Jan Hansmann

Supervisor (Second): Prof. Dr.-Ing. Aldo R Boccaccini

Supervisor (Third): Prof. Dr. med. Thomas Dandekar

Date of Public Defence: ....

Date of Receipt of Certificates: ....

to Jakob,
for friendship that has endured temporal and local separation

Contents

Abstract

Additive manufacturing processes such as 3D printing are booming in the industry due to their high degree of freedom in terms of geometric shapes and available materials. Focusing on patient-specific medicine, 3D printing has also proven useful in the Life Sciences, where it exploits the shape fidelity for individualized tissues in the field of bioprinting. In parallel, the current systems of bioreactor technology have adapted to the new manufacturing technology as well and 3D-printed bioreactors are increasingly being developed.

For the first time, this work combines the manufacturing of the tissue and a tailored bioreactor, significantly streamlining the overall process and optimally merging the two processes. This way the production of the tissues can be individualized by customizing the reactor to the tissue and the patient-specific wound geometry. For this reason, a common basis and guideline for the cross-device and cross-material use of 3D printers was created initially. Their applicability was demonstrated by the iterative development of a perfusable bioreactor system, made from polydimethylsiloxane (PDMS) and a lignin-based filament, into which a biological tissue of flexible shape can be bioprinted. Cost-effective bioink-replacements and *in silico* computational fluid dynamics simulations were used for material sustainability and shape development. Also, nutrient distribution and shear stress could be predicted in this way pre-experimentally.

As a proof of functionality and adaptability of the reactor, tissues made from a nanocellulose-based Cellink® Bioink, as well as an alginate-based ink mixed with Me-PMeOx$_{100}$-*b*-PnPrOzi$_{100}$-EIP (POx) (Alginate-POx bioink) were successfully cultured dynamically in the bioreactor together with C2C12 cell line. Tissue maturation was further demonstrated using hMSC which were successfully induced to adipocyte differentiation. For further standardization, a mobile electrical device for automated media exchange was developed, improving handling in the laboratory and thus reduces the probability of contamination.

Zusammenfassung

Additive Fertigungsverfahren wie der 3D-Druck boomen in der Industrie aufgrund ihres hohen Freiheitsgrads in Bezug auf geometrische Formen und verfügbare Materialien. Mit Blick auf die patientenspezifische Medizin hat sich der 3D-Druck auch in den Biowissenschaften bewährt, wo er die Formtreue für individualisierte Gewebe im Bereich des Bioprinting nutzt. Parallel dazu haben sich auch die derzeitigen Systeme der Bioreaktortechnologie an die neue Fertigungstechnologie angepasst, und es werden zunehmend 3D-gedruckte Bioreaktoren entwickelt.

In dieser Arbeit werden erstmals die Herstellung des Gewebes und ein maßgeschneiderter Bioreaktor kombiniert, wodurch der Gesamtprozess erheblich gestrafft und beide Verfahren optimal zusammengeführt werden. Auf diese Weise kann die Herstellung der Gewebe individualisiert werden, indem der Reaktor an das Gewebe und die patientenspezifische Wundgeometrie angepasst wird. Aus diesem Grund wurde zunächst eine gemeinsame Basis und Leitlinie für den Geräte- und Materialübergreifenden Einsatz von 3D-Druckern geschaffen. Deren Anwendbarkeit wurde durch die iterative Entwicklung eines perfundierbaren Bioreaktorsystems aus Polydimethylsiloxan (PDMS) und einem Lignin-basierten Filament demonstriert, in das ein biologisches Gewebe mit flexibler Form gedruckt werden kann. Kostengünstige Biotintenalternativen und emphin silico Computational Fluid Dynamics Simulationen wurden für eine materialschonende Formentwicklung verwendet. Nährstoffverteilung und Scherspannung konnten auf diese Weise präexperimentell vorhergesagt werden.

Als Beweis für die Funktionalität und Anpassbarkeit des Reaktors wurden Gewebe aus einer Cellink® Bioink auf Nanocellulosebasis sowie einer Tinte auf Alginatbasis, welche mit Me-PMeOx$_{100}$-*b*-PnPrOzi$_{100}$-EIP (POx) gemischt wurde (Alginat-POx-Bioink), erfolgreich zusammen mit C2C12-Zelllinie dynamisch im Reaktor kultiviert. Die Gewebereifung wurde außerdem mit hMSC demonstriert, die erfolgreich zur adipozyten Differenzierung induziert wurden. Zur weiteren Standardisierung wurde ein mobiles elektrisches Gerät für den automatischen Medienwechsel entwickelt, welches die Handhabung im Labor verbessert und damit die Wahrscheinlichkeit einer Kontamination deutlich verringert.

Abbreviations

Abbreviation	Meaning
2D	Two dimensional
3D	Three dimensional
C2C12	Murine myoblast celllinie
Ca^{2+}	Calcium ions
$CaCl_2$	Calcium chloride
CAD	Computer aided design
CFD	Computational fluid dynamics
CO_2	Carbon dioxide
D10	DMEM with 10 % FCS and 1 % Pen/Strep
DMEM	Dulbecco's modified eagle medium
DMSO	Dimethyl sulfoxide
EDTA	Ethylenediaminetetraacetic acid
EtOH	Ethanol
FCS	Fetal calf serum
FD water	Fully demineralized water
FDM (syn. FFF)	Fused deposition modeling
FFF (syn. FDM)	Fused filament fabrication
H_2O_2	Hydrogen peroxide
HE	Hematoxylin and eosin
IBMX	3-Isobutyl-1-methylxanthine

IF	Immune fluorescence
LDH	Lactate dehydrogenase
Mg^{2+}	Magnesium ions
hMSC (pl. hMSCs)	Human mesenchymal stem cell
MTT	3-(4,5-dimethylthiazol-2-yl)-2,5-diphenyltetrazolium bromide
NC	Negative control
PBS^{-}	Phosphate buffered saline without Ca^{2+} and Mg^{2+}
PBS^{+}	Phosphate buffered saline with Ca^{2+} and Mg^{2+}
PC	Positive control
PCB	Printed circuit board
PDMS	Poly(dimethylsiloxane)
Pen/Strep	Penicillin/Streptomycin
PFA	Paraformaldehyde
PLA	Polylactic acid
POx	Me-PMeOx$_{100}$-*b*-PnPrOzi$_{100}$-EIP
rH	Relative Humidity
RM	Regenerative Medicine
rpm	Rounds per minute
RT	Room temperature
sccm	Standard cubic centimeters per minute
SLA	Stereolithography
SLS	Selective laser sintering
TDS	Transport of diluted specimen

TE	Tissue Engineering
UV	Ultra violet
VH_2O_2	Vaporized hydrogen peroxide

1 Introduction

1.1 Tissue Engineering

The term Tissue Engineering (TE) was defined for the first time in 1993 as an interdisciplinary field that combines the principles of Life Sciences and engineering for development and generation of biological constructs able to maintain or restore natural tissue function [1]. These artificial generated tissues can be used either as test systems for medical drugs, cosmetics or classification of hazard chemicals, or as a transplant in the field of Regenerative Medicine (RM). Used as a test system, the tissue construct aims to replace and reduce the amount of animal tests by simultaneously increasing correlation to the human organism [2–4]. Animal tests still show the gold standard in science, but luckily have been decreasing in Germany from 3.08 mio animals in 2012 to 2.2 mio animals in 2019 which is similar to the amount of animals used for scientific experiments back in 2003/2004 [5].

In the context of RM, tissue-engineered artificial organs and tissues are translated to patient-specific implants, counteracting the disproportionality of 3518 transplanted organs compared to 9463 people on the waiting list in 2020 in Germany [6], as shown in the dogma of Tissue Engineering (Fig. 1). In the past decades, a variety of tissue substitutes were developed successfully like e.g. bladder tissue [7–9], trachea [10–12], meniscus [13], skin [14, 15], and arteries manufactured by patient derived stem cells [16–18].

To achieve proper tissue function, suitable usage and combination of cells, scaffold material, and growth factors is crucial [19–21]. To address this issues, stem cells, for example, are used as a high potential cell source for generating complex constructs due to their self-renewal and multipotent abilities [22–24]. However, acquisition and culture of stem cells tend to be costly and difficult in handling compared to somatic cells. These somatic cells (so-called primary cells) can be isolated from patients biopsy for generating a personalized tissue construct and thereby reducing the risk of tissue rejection [25]. Beside the cell source, the used scaffold material also has to meet the specific requirements of the cells and properties of the later tissue [26, 27]. *In vivo*, the extra cellular matrix (ECM) forms a highly specific local niche for each cell, that can be altered in its composition. That way, biological and physical properties like, stiffness, pore size, and else can be customized by the cell itself [28]. *In vitro*, the tissue scaffold has to provide a microenvironment to the cells *in vitro* as closely related to the *in vivo* conditions as possible [29]. A three dimensional (3D) environment is crucial for complex tissue maturation and functionality [19, 20].

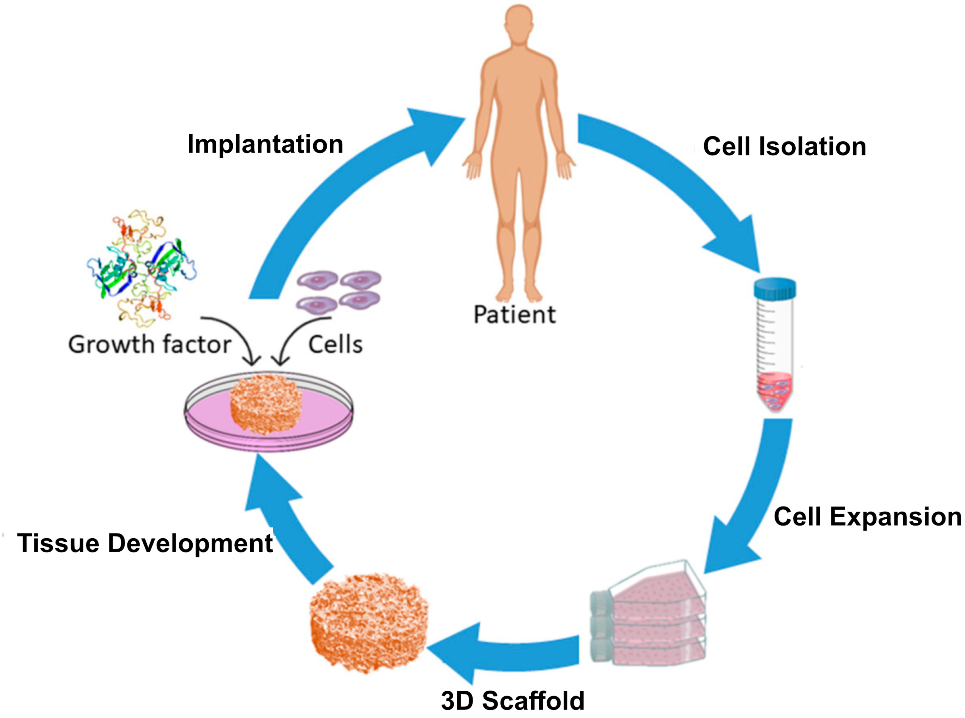

Figure 1: Dogma of Tissue Engineering and Regenerative Medicine. From patient-specific cell isolation to *in vitro* cell expansion, 3D scaffold construction and tissue development or maturation, and finally implantation to the patient. Figure taken from Asadian *et al.* [30].

A variety of scaffolds are used to generate this kind of environments, showing common properties like biocompatibility, possibility for cell adhesion, certain pore sizes for migration, and nutrient transport. As long as these properties are met, the scaffold material can be biological as well as artificial originated [19, 21, 25, 31]. Both types of scaffolds have their advantages and disadvantages: biological scaffolds, like decellularized tissues, require a harvest from animals and are hardly standardizable, making it nearly impossible to use them as transplants [29]. Those scaffolds in contrast tend to show a more natural biocompatibility compared to artificial scaffolds. Especially degradation of the scaffold *in vivo* could lead to immune rejection and has to be addressed [32–34]. Due to this, efforts are made to increase standardization in biological materials. For example, gelatine is used as a highly standardized and versatile material today [35–37], but also bacterial nanocellulose [38–40] or collagen I [41–43] are commonly used as biological scaffold material [44].

1.2 Bioreactors

Beside the initial tissue generation, tissue maturation is usually needed subsequently to ensure proper tissue function. Therefore, usage of various bioreactor systems has been established in TE to provide an *in-vivo*-like tissue-specific environment *in vitro*. The term 'bioreactor' is not concretely defined and used for a broad variety of systems in pharmacy, agriculture and medicine. In a medical context, bioreactors are containers able to hold a fabricated tissue, provides an *in-vivo*-like environment, and it protects it from contaminations and other external influences [45–48].

To meet this need, the used material has to be biocompatible and further must behave inert towards other materials in the system. Additionally, more complex bioreactor systems ensure proper nutrient supply and removal of waste products by dynamically perfusing the tissue construct with medium. Even though the design of bioreactors is indefinetly versatile, subcategories have been summarized according to the way how dynamics are applied to the bioreactor [49, 50]: Spinner flasks create dynamics by rotation of the medium around the cells and tissues in a glass bottle. Rotating wall vessels in contrast show a rotation of the whole bioreactor to generate dynamics inside. Perfusion bioreactors aim for a more *in-vivo*-like situation, where the tissue is perfused with channel-like structures, simulating *in vivo* blood vessels. Implementing this kind of *in-vivo*-like blood flow is mandatory to overcome limitations by nutrient diffusion which is preventing generation of larger tissues [51]. By applying a dynamic flow, shear stress is generated inside the vessels, which is a crucial factor for e.g. endothelial cells [52–54]. This way, the bioreactor system also has to keep a constant pH-value [55], which can either be done by adding HEPES-buffer to the medium or by application of sterile CO_2-exchange. Further requirements have been discussed in literature [56, 57]. In the past, bioreactors have been designed to serve a variety of different tissues and applications, reducing the manufacturing costs and enhancing the versatility of such systems.

Nevertheless, attempts are made for quite some time now for bioreactors designed for more specific and complex tissues. This is necessary since novel tissues and building blocks demand specialized mechanical and biological environments. Also here the economical factor comes into play which has led to reusable bioreactors mostly manufactured from metals, glass or inert plastics.

1.3 Additive Manufacturing

1.3.1 3D Printing

Considering bioreactor manufacturing, subtractive methods still show the gold standard. Unfortunately common subtractive methods like milling and grinding are usually time- and cost-intensive and are not suitable for prototyping or small batch production [58–60]. A smart economic tool to overcome these limitations is 3D printing, which has evolved with incredible speed in the last years. 3D printers and materials have become more affordable and handling was improved, so that even private households can easily access this new technology [61–64]. All in all, a high variety of different printing techniques have been developed so far, making it difficult to distinguish them clearly. As a result, efforts were taken towards a standardized nomenclature which is published in DIN EN ISO 52900 [65]. The three most used techniques in 3D printing are fused deposition modeling (FDM), also called fused filament fabrication (FFF), stereolithography (SLA) and selective laser sintering (SLS) (Fig. 2).

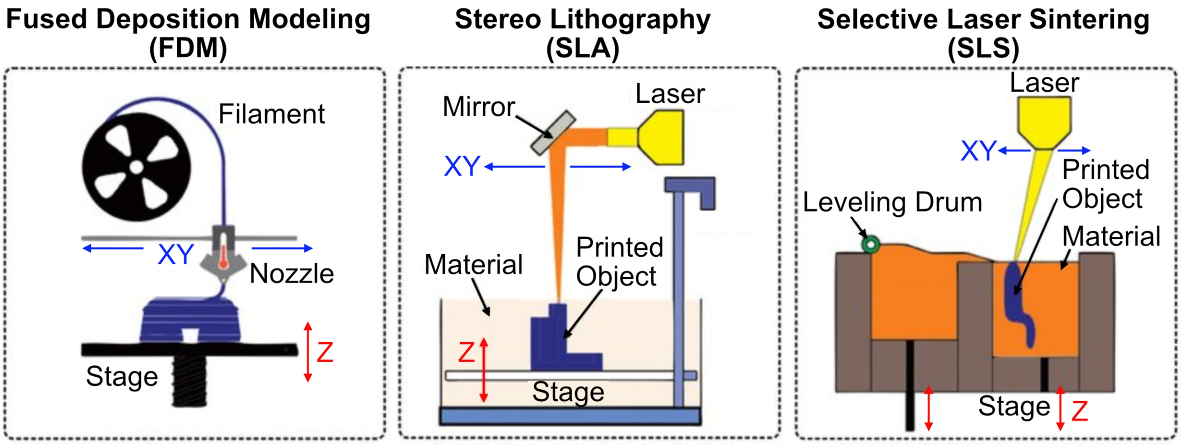

Figure 2: Schematic visualization for three most used printing techniques. Image adapted from Gul *et al.* [66].

FDM uses thermoplastic filaments that are fed into a heated printhead where it is melted and subsequently squeezed through a nozzle. SLA in contrast uses photosensitive resins which are crosslinked by a laser or any other light source. SLS technique in addition uses powdered materials, which are melted and fused together by a laser. Advantages and disadvantages of those printing techniques have been addressed in a previous paper [67] and are explained in detail in the following work.

Common for all 3D printing techniques is the digital preparation of the geometrical shape: In a first step, a geometry is modeled by computer aided design (CAD) and transferred into a so-called standard triangulation language (STL) file. This format shows a common standard that is accessible by every 3D printing software. In this file-format, surfaces are decomposed to triangles which makes it possible to save a geometry as a mathematical-like function with a low data size. This way, the geometry is then processed in a so-called slicer-software. Within this software the geometry gets translated into a machine-specific set of commands and coordinates, called Gcode. The Gcode is specifically generated for every individual printer and material since it contains information about every single setting that is done in the printer- or slicer-software [68–71].

Since 3D printing shows an extraordinary high degree of freedom, complex hollow structures, undercuts or advanced channel geometries can be crafted that would not be possible by subtractive methods. Using this technique, first attempts for 3D-printed bioreactors and bioreactor-like structures have already been realized [72–76]. Still, this selective achievements show, that designing tailored bioreactor geometries for 3D printing is not a straight forward process and requires detailed knowledge about the individual capabilities and limitations of the printer device. Especially complex geometries including channels, overhangs and small sections, 3D printers highly differ in quality. Additionally, crucial requirements like tightness and leakage-proof of the entire bioreactor setup has to be mentioned according to the used printing technique and device.

1.3.2 Bioprinting

A special area of the production of biological constructs within RM and TE is the field of biofabrication [77]. Biofabrication focuses mainly on the production of living tissues and organs using cells and scaffolds as building blocks and novel manufacturing processes. Together with the currently rising additive technologies of 3D printing, bioprinting forms a synergistic intersection [77, 78]. Beside several variations there are three major groups for bioprinting techniques available that are closely related to common 3D printing techniques (Fig. 3):

Extrusion-based bioprinting generates 3D models by deposition of hydrogels, forming the desired object and thereby the method is closely related to FDM printing. Depending on the technical realization of the distinct device, material extrusion printing can be subclassed into pneumatic, mechanical or solenoid printing [79, 80].

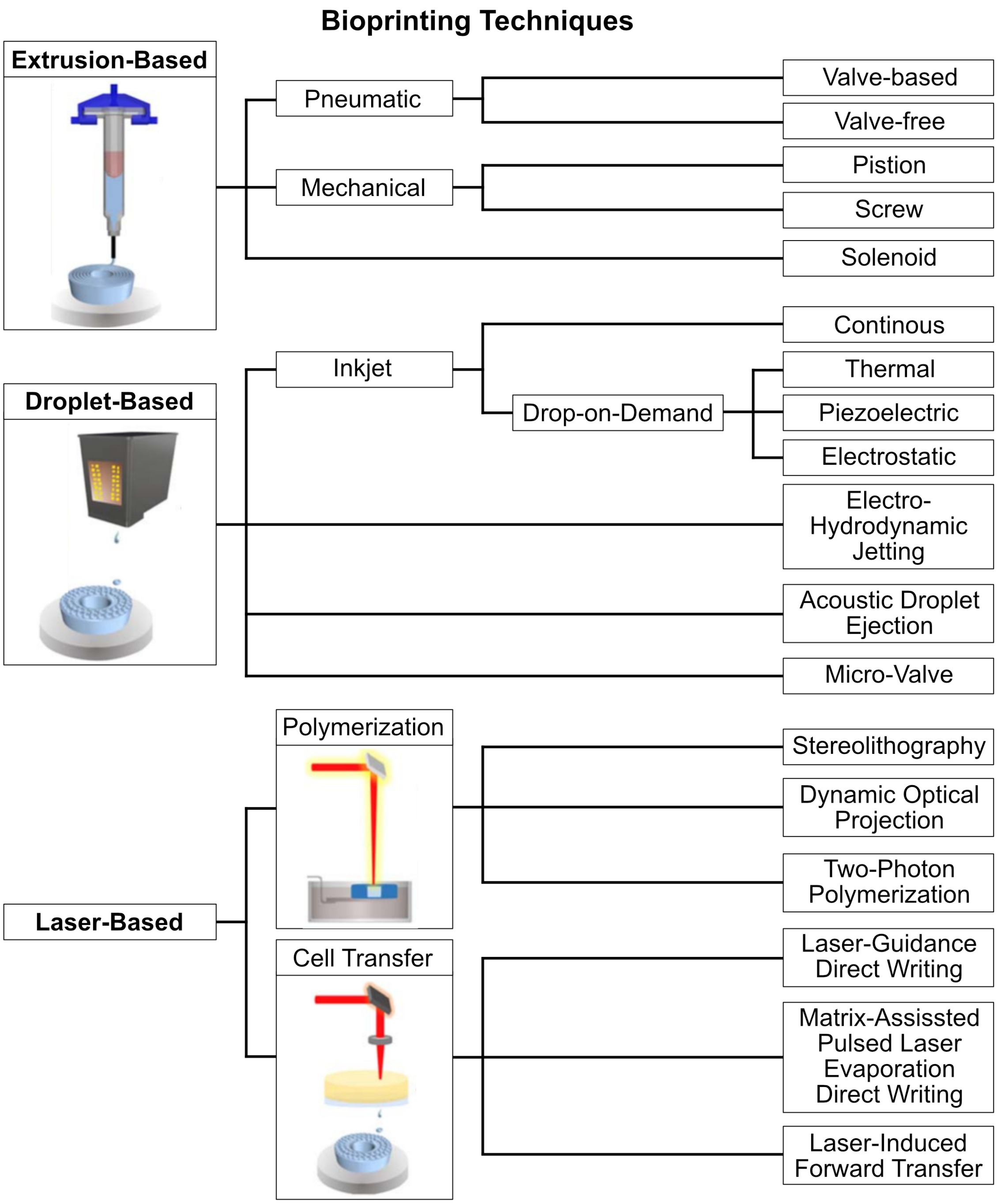

Figure 3: Classification of bioprinting technologies by Ozbolat *et al.* 2017 [80]. Image adapted from Sun *et al.* [79].

Different to that, the group of droplet-based bioprinting techniques form small distinct droplets of the bioink for printing onto the printbed layer by layer. This techniques can further be divided into Inkjet Bioprinting, Electro-hydrodynamic Jetting, Acoustic Droplet Ejection, and

Micro-valve Bioprinting [78–82]. Laser-based bioprinting is closely related to SLA printing by using laser-induced material polymerization. Common variations of this technique are process-involving photopolymerization and processes based on cell transfer [79, 80].

Biological hydrogel materials used by bioprinting are referred to as 'bioink' and defined in detail by Groll *et al.* [83]. Tissue engineering and biofabrication make great claims to bioinks, which can be subdivided into physical, biological and economical requirements: First of all, the bioink identifies itself by the possibility to print [84–87]. This means it has to be viscous enough to keep its geometrical integrity after printing, but must not apply to much sheer force to the cells during the actual printing process, which has to be conducted between 4 °C and 37 °C due to the cells mixed into the inks [88, 89].

All in all, the bioink has to provide a beneficial environment for the individual embedded cells during tissue maturation. This includes cell-induced reorganization of the scaffold, cell attachment and proliferation, as well as proper nutrient supply [88, 90–92]. Often, cell-induced scaffold reorganization leads to shrinkage of the scaffold and has to be addressed during the bioink development. The issue of proper nutrient supply can be overcome by geometrical solutions like including tissue perfusion. Additionally, bioinks need to have a realistic economical availability and price, or may generated individually. Most important, composition and quality may not variate between batches.

During the last years, a variety of bioinks have been published and some of them have also become commercial available [93]. Commonly used basic materials for bioinks are e.g. gelatine, alginate, and nanocellulose [94, 95], but also synthetic materials [96]. These materials get mixed or chemically adapted in different ways to improve their properties towards bioink-usage [84–87].

Bioprinted solutions for RM have already been realized for e.g. bone and skull implants [97–101]. These studies show, that especially stiff tissues can be bioprinted in a sufficient size and functionality for transplantation. Additionally, focus on the maturation process is often neglected and performed only in static conditions. Two major reasons can be stated for this: first, the lack of bioreactors that are easily adaptable to the individual transplant, and second the transfer of a freshly printed construct into such a system. Even when crosslinked, bioprinted constructs show a rather weak integrity compared to fully matured constructs and thereby have to be handled more carefully.

1.3.3 Combined Printing

To overcome these shortcomming just meantioned, the techniques of conventional 3D printing and bioprinting can be combined. With this, a tailored bioreactor can be printed for a tissue construct which is printed directly into the bioreactor within the same device at the same process. This way the freshly bioprinted construct doesn't have to be transferred.

Combining conventional 3D printing methods with bioprinting is a rather new idea in the field of biofabrication and bioreactors [102–104]. Due to a lack of standardized terms, this technique is often referred to as 'simultaneous printing'. To go more in detail, this can be further subdivided into three different approaches: first of all 'sequential printing', which is a process were the geometry is printed in a common 3D printer and afterwards transferred to a bioprinter for generating the bioprinted component. In contrast to that, 'combined printing' refers to the method for having a thermoplastic printhead and a bioprinting printhead installed in the same device. In this case, the different parts are still printed after each other automatically but within the same device without manual intervention. In a third method, which can be called 'true simultaneous printing', the thermoplastic printed part and the biological part are printed layer by layer at the same time in the same device.

Clearly, the overall degree of automation is increasing within these methods which is important when translating the process from the lab to an economical setting and application in the clinics. In this context labautomation is a key-technology for the marketable realization.

1.4 Labautomation

In recent history, some key-technologies have been made, causing a rapid change in production, also referred to as 'industrial revolutions' [105]. Industry and politicians nowadays have identified two of those revolutions linked to the past, a third revolution which we are experiencing right now, and a future revolution called 'Industry 4.0' [106]: The first revolution is defined by the usage of steam engines in the 18th century, while the second one is referred to the usage of electricity in the 19th century. The third revolution, also called 'digital revolution', was beginning in the 1970s after the definition of the term 'labautomation' by the chemical industry, which switched from manual synthesis to automated process plants [107, 108]. These plants took over basic operations like stirring, tempering, dosing and similar. To do so, sensors and actuators, like pumps and valves, where combined with devices like probes, thermostats, heaters and so on. This was possible due to the upcoming computer systems which were used to control those individual units in a meaningful manner. Our current industry is characterized by the usage of microchips, computer-based intelligence and robots. The fourth revolution that has yet to come, also referred to as the 'internet of things', forecasts artificial intelligence and network communication being the motor for product plants and assembly lines [106, 109]. The technological progress can be stated by the degree of automation which correlates with the ability of machines to work independent without human intervention. Aim of this is the relief of human workers from dangerous and risky labor, as well as demotivating routine actions, but also to increase the complexity and quality of the manufactured products. A multitude of devices with different degrees of automation can be found in Life Science labs today: Plate readers for quantification of fluorescence, luminescence or optical density, PCR-cyclers for amplification of DNA and RNA fragments, embedding-machines for paraffin-embedding of tissues, and staining-centers for automated histological sample staining.

According to this, it is only logic, that bioreactor systems and incubators have also already been equipped with automation solutions like e.g. controlling atmosphere, pump speed, and dynamics [110–113]. An increase of the degree of automation for bioreactor systems enhances the complexity and quality of the tissue-engineered constructs and is thereby inevitable for the progress of TE and RM.

1.5 State of the Art of Bioprinted Tissues

A prominent achievement in bioprinting, which also got public attention, was the bioprinting of a personalized human heart (Fig. 4) [114]: In their work they firstly isolated cells from omental tissue biopsy of a patient and redifferentiated them to induced pluripotent stem cells. Afterwards the cells were differentiated into cardiomyocytes and endothelial cells, the two most important cell types in heart tissue beside neuronal cells. As a bioink they used a personalized hydrogel derived from the decellulariced extracellular matrix from the biopsy [115]. By performing computerized tomography (CT), they got intel on the specific geomety of the vessels of the patient. As described before, they used CAD techniques to generate a tissue model prior to printing. In this special case they bioprinted the tissue into a support bath, crosslinked it by increasing the temperature and resolved it from the support bath. Even though, the heart only had a size of roughly 2.5 cm, their work shows the high potential of biofabrication.

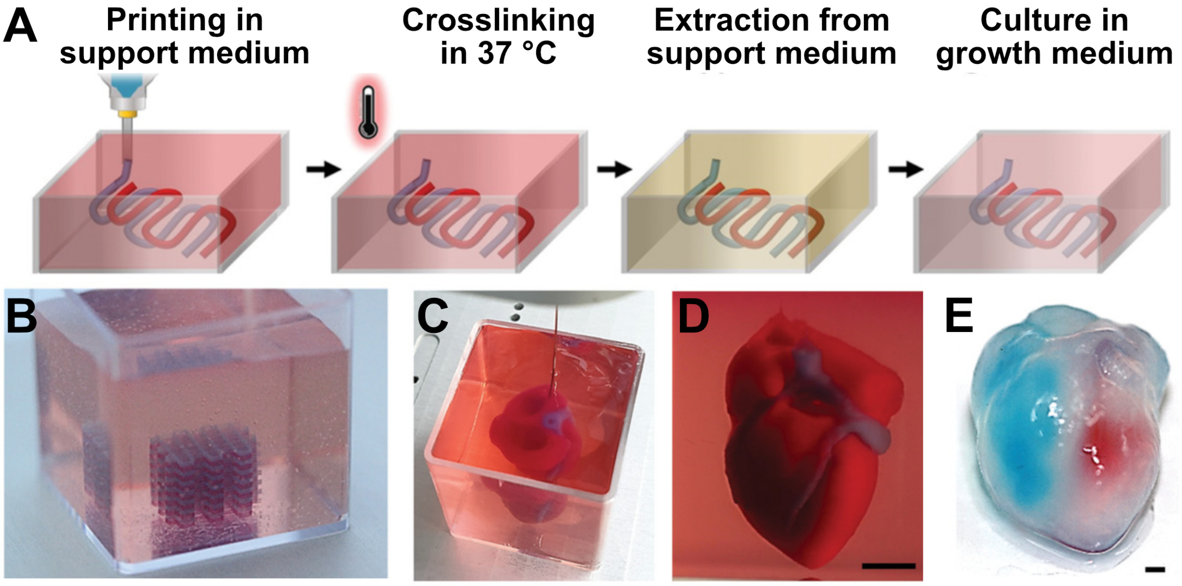

Figure 4: State of the art bioprinted human heart. (A) 3D printing concept including the printing process within a support bath, followed by crosslinking and transfer from the support bath into growth medium. (**B**) A simplified multilayer construct printed inside the support bath. (**C+D**) A printed heart construct within a support bath. Scale = 5 mm. (**E**) Ventricles injected with red and blue dyes for demonstrating hollow chambers and the functional septum. Scale = 1 mm. Image adapted from Noor *et al.* [114].

Still, current limitations of the bioprinting process are also identifiable: they had to remove the crosslinked tissue from the support path in order to perform additional experiments. Also, no maturation or perfusion was performed. In accordance to recent developments in biofabrication, 3D printing has found its way to bioreactor manufacturing. The high degree of freedom and the rather cheap materials support complex geometries as well as trial-and-error studies. Also, current publications lack a combination of 3D printing of bioreactors and bioprinting of the tissue constructs.

1.6 Aim of the Study

The successful fabrication of a human heart by the principle of bioprinting using patient-derived cells and bioink material has demonstrated the feasibility of such an approach for generating artificial tissues and organs with high shape fidelity. Their work, representative of the many previous biofabrication projects, paves the way for bench to bed translation of future projects.

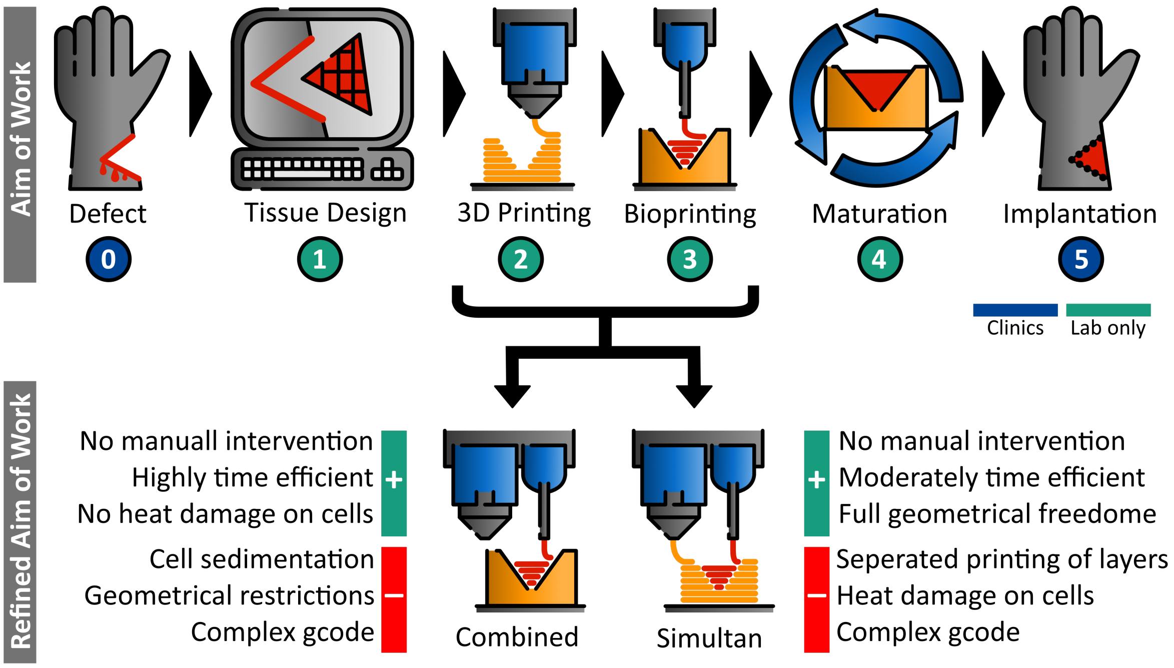

Figure 5: Graphical aim of work. Workflow for 3D printing of tailored bioreactors includes identification of defect geometry (**0**) and redesiging the part by CAD (**1**). Followed by designing and printing of a tailored tissue container/bioreactor (**2**) and the bioprinting of the desired tissue (**3**). Finally, the tissue is matured within the bioreactor system (**4**) and implanted to the patient (**5**). Further, 3D printing and bioprinting steps can be refined by combined or simultaneous printing approaches. Step 0 and 5 are clinical work only and are of no focus in this work.

However, besides the successful fabrication of such tissues and the aquisition of primary material, issues such as tissue maturation still remain unanswered for bioprinted tissues. A number of projects in the past have researched solution strategies for perfusing artificial tissues and established the profound field of bioreactor technology. Currently, a majority of these solutions are still based on traditional, inflexible geometries and components, and in some cases obstruct patient-specific customization.

Therefore, the main goal of this study is to link both sub-areas, incorporating modern additive manufacturing techniques, in order to ensure the shape fidelity and thus the patient-specific adaptation of such a system. The dogma of TE and RE shall be extended by a novel set of techniques for patient-specific tissue generation, as shown in figure 5, addressing steps like tissue design, bioreactor development and printing, as well as bioprinting of the tissue and perfused tissue maturation. To achieve this, available 3D printing technologies and devices, as well as materials are first classified and standardized for their suitability in biological systems using appropriate parameters and test procedures. A guideline for the analysis of 3D printing devices and materials represents a partial success of this work. This guideline will then be used as a basis for generating a suitable bioreactor geometry for combined 3D printing. The development will focus on parameters such as perfusability and nutrient supply, as well as printability and shape fidelity of the tissues, while reducing printing time and material consumption.

In a second milestone, the combination of the two printing processes will be realized. This involves using the shape fidelity of the system to sequentially print a set of different tissue shapes directly into the bioreactor. In order to provide a sustainable process, this will be achieved using commercially available and environmentally compatible bioink alternatives. Since the patient-specific production of tissues involves small to single batch sizes, and mostly limited sources for primary material, a pre-experimental *in silico* simulation system will be implemented to evaluate the nutrient supply of an individual tissue shape without the use of valuable biological materials.

For the final realization of the overall process, bioreactor and tissue will be produced in a sequential printing process and its functionality, such as tissue maturation, will be implemented with different bioinks: commercial nanocellulose-based Cellink® Bioink and and self-produced mix from Me-PMeOx$_{100}$-*b*-PnPrOzi$_{100}$-EIP (POx) [116] and alginate, which was developed by Hu et al. [117]. The novel POx-polymer and the ink have already been characterizied and used for various applications [118–123].). Flexibility will further be stated by using different cell-sources such as celllinies (C2C12) and primary cells (hMSC). In a final milestone, bench to bed translation will then be advanced by increasing the standardizability and reducing the handling hurdles for clinical staff as well as the financial effort to support them. For this purpose, an automation system for the 3D-printed reactor system will be realized.

2 Materials

2.1 Equipment

Table 2: Equipment

Item	**Company**
O_2 Generator	Kröber Medizintechnik GmbH (GER)
Accu-jet Pro	Brand GmbH & Co KG (GER)
Air filter, sterile	Sartorius AG (GER)
Autoclaving device DX-45	Systec GmbH (GER)
Bioprinter nozzles	Nordson medical (USA)
Cedex Bio Analyzer	F. Hoffmann-La Roche AG (CH)
Cell culture flask 25 | 75 | 150 cm^2	TPP (GER)
Centrifugation tubes 15 | 50 ml	Greiner Bio-One (GER)
Centrifuge	Eppendorf (GER)
Clean Bench	Thermo Fisher Scientific (GER)
Counting Chamber	Paul Marienfeld GmbH & Co KG (GER)
Cover Slips	Thermo Fisher Scientific (GER)
Cryo tubes	Nunc (GER)
Disposable bag (autoclavable)	Melag (GER)
Drying Oven 70 °C	MEDITE Medical GmbH (GER)
Drying Oven 37 °C	Memmert GmbH & Co. KG (GER)
Embedding cassettes	Sakura Fineteck (NL)
Embedding center	Leica Camera AG (GER)

Formlabs Form Cure	Formlabs (USA)
Formlabs Form Wash	Formlabs (USA)
Formlabs Form2 printer	Formlabs (USA)
Freezer $-20\,^{\circ}\mathrm{C}$	Liebherr (GER)
Freezer $-80\,^{\circ}\mathrm{C}$	Kendro (GER)
Glass slides	Thermo Fisher Scientific (GER)
Ice machine	Scotsman (IT)
Incubator	Thermo Fisher Scientific (GER)
Injection cannulas SUPRA	Ehrhardt GmbH (GER)
Inkredible+™ bioprinter	CELLINK AB (SWE)
Liquid nitrogen storage tank	Jutte Ohst german-cryo GmbH (GER)
LUER tube fittings, diverse	Nordson medical (USA)
Microscope EVOS XL	Thermo Fisher Scientific (GER)
Microscope Keyence	Keyence GmbH (GER)
Microtome	Leica (GER)
Molds (HE)	Sakura Fineteck (NL)
Mr. Frostie™	Nalge Nunc Inter. Cor. (USA)
OEM pumps Ismatec®	Cole-Parmer GmbH (GER)
OEM pumps Spetec®	Spetec GmbH (GER)
Oven HERATHERM	Thermo Fisher Scientific (GER)
Parafilm M	Bemis Inc. (USA)
Pasteur Pipettes	Brand (GER)
Peripheral venous catheder	B. Braun Melsungen AG (GER)

Petri dish with glass base	Thermo Fisher Scientific (GER)
Petri dishes	Greiner Bio-One (GER)
Pico P100 plasma device	Diener electronic GmbH & Co. KG (GER)
Pipette tips 10 | 100 | 200 | 1000 µl	Eppendorf (GER)
Pipettes 5 | 10 | 25 | 50 ml	Greiner Bio-One (GER)
Prescision scale	Satorius Weighing Technology GmbH (GER)
Printer cartridges 3 ml	Nordson medical (USA)
Pumping tubes	Cole-Parmer GmbH (GER)
Raise3D Pro 2	Raise 3D Technologies Inc. (USA)
Reaction vessels 1.5 | 2 ml	Sarstedt (GER)
Rocking shaker	neoLab (GER)
Scale	Kern & Sohn GmbH (GER)
Scalpel holder + blades	Bayha (GER)
Sealing gaskets	Arcus GmbH (GER)
Silicone hoses (Tygon®)	IDEX Health & Science GmbH (GER)
Sinterit Lisa Pro	Sinterit sp. z o.o. (PL)
Sinterit Sandblaster	Sinterit sp. z o.o. (PL)
Smartphone Pixel XL	Google Inc. (USA)
Sterilisation bag Stericlin®	Vereinigte Papierwarenfabriken GmbH (GER)
Syringes 2 | 5 | 10 | 20 ml	Becton, Dickinson and Company Corp. (USA)
Tecan plate reader	Tecan Trading AG (CH)
Tweezers	Assisstent (GER)
Ultra sonic bath	Branson Ultrasonics (USA)

Vacuum casting machine	J. Schüchel®(GER)
Vacuum pump system	Integra Biosciences (GER)
Water Bath	Julabo Labortechnik (GER)
Water purification device Milli-Q	Merck KGaA (GER)
Well plates 6 | 12 | 24 | 48 | 96	TPP (GER)
Well plate 96, clear bottom	Greiner Bio-One (GER)
Zwick Z010	Zwick Roell AG (GER)

2.2 Chemicals

Table 3: Chemicals

Chemical	**Company**	**Order No.**
$CaCl_2$	Sigma-Aldrich	A8960
Cellink® Bioink	CELLINK AB	IKC200000303
Crosslinking agent	CELLINK AB	CL1010006001
Descosept	Dr. Schuhmacher	N-20338
Dexamethason	Sigma-Aldrich	D4902
DMEM (1X) + GlutaMAX™-I	Thermo Fisher Scientific	61965-026
DMEM/F12 (1:1) (1x)	Thermo Fisher Scientific	31331-028
DMSO	Sigma-Aldrich	D8418
Dublisil® 15	Dreve Deutschland	D4806
Dublisil® 22+	Dreve Deutschland	D4531
Dublisil® 30	Dreve Deutschland	D4502
EDTA	Sigma-Aldrich	E5134

Entelan®	Merck	1.079.610.500
Eosin	MORPHISTO	10177.01000
Ethanol	Sigma-Aldrich	32205
FCS (Bio&Sell)	Bio & Sell	BS.FCS 0.500 EUA
FCS (Biochrom)	Merck	S 0615
Green-TEC Pro Filament	Extrudr | FD3D	GTP175X800NAT
H_2O_2 60 %	Thermo Fisher Scientific	10336280
Hematoxylin	MORPHISTO	10231.01000
IBMX	AppliChem	A0695
Indomethacin	Sigma-Aldrich	I7378
Insulin	Sigma-Aldrich	I9278
Isopropyl alcohol	Carl Roth	6752.5
MTT	Sigma-Aldrich	M2128
PA12 Smooth v2	Sinterit sp. z o.o.	5904722229310
Paraffin	Carl Roth	5642.6
PBS^-	Sigma-Aldrich	D8537
PBS^+	Sigma-Aldrich	D8662
Pen/Strep 100X	Sigma-Aldrich	P4333
PLA Filament - Black	Filamentworld	PLA175XBLK1
Resin Dental SG	Formlabs	RS-F2-DGOR-01
Resin Clear	Formlabs	FLGPCL04
Resin Model V2	Formlabs	RS-F2-DMBE-02
Roti-Histofix® 4 % (PFA)	Carl Roth	P087.3

Sylgard^{TM}-I 184 Silicone	DOW Silicones Deutschland	001004229002
Trypan Blue	Sigma-Aldrich	T8154
Trypsin	SERVA Electrophoresis	37289.02
Trypsin/EDTA	Thermo Fisher Scientific	15400-054
Water bath ingredient	Carl Roth	AN93.1
Xylene	Carl Roth	9713.3

2.3 Cells & Tissues

Table 4: Cells & Tissues

Cell type	**Source Tissue**	**Patient No.**	**Passage used**
hMSC	Human bone marrow (male)	P48	3
C2C12	Murine myoblast	Celllinie	Not Applicable

2.4 Assays

Table 5: Assays

Kit	**Company**	**Order No.**
Cedex Kit Glucose Bio	Roche	6343732001
Cedex Kit Lactate Bio	Roche	6343759001
Cedex Kit LDH Bio	Roche	6343767001
CellTiter-Glo® Luminescent Cell Viability Assay	Promega	G7570
LIVE/DEAD^{TM} Viability/Cytotoxicity Kit	Life Technologies	L3224

2.5 Solutions & Media

Table 6: Solutions & Media

Solution	Supplements	Concentration
C2C12 Medium	FCS (Biochrom)	100 ml/l
(D10)	Penicillin/Streptomycin 100X	10 ml/l
	solved in DMEM (1X) + GlutaMAX^{TM}-I	
	stored at 4 °C	
Dexamethason	Dexamethason	3.925 g/l
(Stock Solution)	*solved in Ethanol*	
	stored at −80 °C	
Dexamethason	Dexamethason (Stock Solution)	1:10
(Working Solution)	*solved in Ethanol*	
	stored at −20 °C	
IBMX	3-Isobutyl-1-Methylxanthine (IBMX)	0.1111 g/ml
(Working Solution)	*solved in Dimethyl sulfoxide (DMSO)*	
	stored at −20 °C	
Indomethacin	Indomethacin	0.035 78 g/ml
(Working Solution)	*solved in Dimethyl sulfoxide (DMSO)*	
	stored at −20 °C	
MSC Medium	FCS (Bio&Sell)	100 ml/l
(for expansion culture)	Penicillin/Streptomycin 100X	10 ml/l
	solved in DMEM/F12 (1:1) (1X)	
	stored at 4 °C	

MSC Medium	FCS (Bio&Sell)	100 ml/l
(for adipose	Dexamethason (Working Solution)	1 ml/l
differentiation)	IBMX (Working Solution)	1 ml/l
	Insulin	1 ml/l
	Indomethacin (Working Solution)	1 ml/l
	solved in DMEM (1X) + GlutaMAX^{TM}-I	
	stored at 4 °C	
PFA + $CaCl_2$ 0.3M	$CaCl_2$	33.3 g/l
($PFA/CaCl_2$)	*solved in Roti-Histofix® 4 % (PFA)*	
	stored at room temperature	

2.6 Software

Table 7: Software

Software	Version	Company
Affinity Designer	1.10	Serif Ltd.
Affinity Photo	1.10	Serif Ltd.
Arduino IDE	1.8.16	Arduino LCC
BZ-II Analyzer	BZ-9000	Keyence GmbH
Citavi	6.10	Swiss Academic Software
COMSOL Multiphysics	5.3	COMSOL Multiphysics GmbH
GraphPad Prism	6.0.7 & 9.2.0	GraphPad Software Inc.
ideaMaker	3.4.2 - 4.2.0	Raise3D Technologies Inc.

ImageJ	1.53g	National Institute of Health
Microsoft Suite	365 Single	Microsoft Deutschland GmbH
PreForm	3.0.1 - 3.19.0	Formlabs
Repetier-Host	2.2.2	Hot-World GmbH & Co. KG
Sinterit Studio 2019	1.4.5.0	Sinterit sp. z o.o.
SolidWorks® Premium	2017	Dassault Systèmes SolidWorks Corp.
Tecan i-control	2.0.10.0	Tecan Trading AG
testXpert II	V3.1	Zwick Roell AG
Ultimaker Cura	4.2.1 & 4.3	Ultimaker

2.7 Dockingsstation Parts

Table 8: Dockingstation Parts

Item	Company
2-Relais module 5 V	AZ-delivery
3/2-Pinch valve PSK-1615W 12 V	BMT Fluid Control Solutions
Arduino UNO R3 Microcontroller	Elegoo
Battery charge indicator	Chanketch ETCH
Cable 14AWG 1.5 mm^2	NorthPada Direct
Capacitor 16 V 1000 µF	Reichelt
Dupont Cable Connector Crimp Set	FeiHong
Female PINs set for PCB	KYYKA-EU
Jumper cable set 560 pieces	QIMEI-SHOP

LCD screen 16x2 with I^2C module	AZ-delivery
LED strip 6000 K 12 V 120 LEDs/m	Onforu-EU
LiFePO4 battery pack 12.8 V 3 A h	Just Battery Technology
ON/OFF Switch	GLyu EU
Peristaltic pump with NEMA 17 stepper motor	Aiwend
Potentiometer button	Weisser Berg
Power jack sockets	RUNCCI-YUN
Power supply unit 14 V 4 A	FXLING EU
PWM solar controller 12 V 5 A	Y-SOLAR DE
Rotary encoder module	AZ-delivery
Schottkydiode 1N5820 20 V 3 A	Reichelt
Screw M3x14 A2 ISO 7380-1	Schrauben24.de
Screw terminal block set for PCB	ANKKY
Stainless steel button waterproof	Larcele Store
Stepper motor driver modul DRV8825	Fruitscher
WAGO cable connectors	Outlet4Life
Prototype PCB for Arduino UNO R3	DollaTek

3 Methods

3.1 Cell Culture

3.1.1 C2C12

C2C12 celllinie was cultured and expanded in D10 medium (Tab. 6, p. 32) by seeding 1000 cells per cm^2 into cell culture T-flasks (TPP, GER). Cells were stored in an incubator (Thermo Fisher Scientific, GER) at 95 % rH, 37 °C and 5 % CO_2. Medium exchange was performed every second to third day.

At a confluency of $\geq$ 70 %, cells were passaged: Therefore, medium was removed and the cells were washed with PBS$^-$ once. Afterwards, the PBS$^-$ was replaced by Trypsin/EDTA (Thermo Fisher Scientific, GER) and incubated for 3 min at 37 °C to detach and separate the cells. By adding cell culture medium, the function of trypsin was blocked and the cells were counted using trypan blue (Sigma-Aldrich, GER) and a counting chamber (Paul Marienfeld GmbH & Co KG, GER). Cells were then seeded to a new T-flask.

For long term storage, the cells were detached from the cell culture flask as described above. After counting, the cells were resuspended in cell culture medium to a ratio of 1 mio cells per 900 µl and filled into cryo tubes (Nunc, GER) with 900 µl per tube. Next, 100 µl DMSO (Sigma-Aldrich, GER) was added to each tube. The tubes were transferred to a Mr. Frostie^{TM} (Nalge Nunc Inter. Cor., USA) and stored at −80 °C for 24 h. The next day, the tubes were transferred into a liquid nitrogen storage tank.

To thaw cells, a cryo tube was rinsed with preheated medium until the cell suspension was completely thawn. Then, the suspension was centrifuged to remove the DMSO from the cell suspension. 2000 cells/cm^2 were then seeded into T-flasks.

In general, cell culture medium was preheated to 37 °C prior to use and centrifugation steps were performed at 300 xg for 3 min at RT.

3.1.2 hMSC

2D cell culture of human mesenchymal stem cells (hMSCs) was performed by Christoph Malkmus, using the MSC expansion culture medium (Tab. 6, p. 32). For adipose differentiation, medium was changed to MSC differentiation medium (Tab. 6, p. 32).
In general, cell culture medium was preheated to 37 °C prior to use and centrifugation steps were performed at 300 xg for 3 min at RT.

3.2 Bioprinting Process

3.2.1 Gcode Generation

Gcodes for bioprinting were manually generated using Repetier-Host software (Hot-World GmbH & Co. KG, GER) for visual live feedback. For both bioinks (Alginate-POx and Cellink® Bioink), first layer height was set to 400 µm, following layer height after first was set to 600 µm, strand distance was set to 1 mm and the printing speed was set to 600 mm/min. Gcodes were manually adapted to printer-specific commands (Code 4, p. 120).

3.2.2 Bioink Preparation

Alginate-POX bioink was prepared ready-to-use by Lukas Hahn. In brief: The thermogelling AB diblock copolymer (Me-PMeOx$_{100}$-*b*-PnPrOzi$_{100}$-EIP), further reffered to as 'POx', comprising the hydrophilic poly(2-methyl-2-oxazoline) (PMeOx) block and thermoresponsive poly(2-*n*-propyl-2-oxazine) (PnPrOzi) block was synthesized as described by Lorson *et al.* [116]. Derived from Hu *et al.* [117], Alginate-POx bioink was generated by mixing 25 weight-% POx-polymer and 1 weight-% alginate in PBS$^-$ (diluted with Millipore water by a ratio of 1:3) over night at 4 °C. Alginate-POx bioink was stored short term (< 6 weeks) at 4 °C and long term (> 6 weeks) at −80 °C.
If frozen, the bioink was stored at 4 °C for 24 h to thaw it properly before usage. To prevent the POx-polymer from crosslinking, it was kept on ice during cell preparation. First, the required amount of bioink was filled into a 3-ml-printer-cartridge and connected to a double-

male LUER-fitting (both Nordson medical, USA). Then, cells were detached and counted as described in section 3.1. The required amount of cells were resuspended in 100 µl PBS$^-$ and filled into a 5-ml-syringe. The syringe was then connected to the LUER-fitting with the printer cartridge. The cells were mixed with the bioink homogeneously by pushing and retracting the piston of the syringe multiple times, ending with the mixed solution in the cartridge. Afterwards the mixed bioink was stored at 37 °C for 30 min for pre-crosslinking of the POx-polymer to increase viscosity and achieve a better printing behavior over all. After that, the bioink was installed into the bioprinter ready for bioprinting.

Commercial nanocellulose-based Cellink® Bioink (Cellink AB, SWE) was stored at 4 °C upon arrival according to manufacturer instructions. First, the required amount of cells were detached and counted as described in section 3.1 and further resuspended in 100 µl PBS$^-$. The cell suspension was then filled into a 5-ml-syringe. Both, the cartridge with bioink and the syringe with the cell suspension were connected via a double-male LUER-fitting (Nordson medical, USA). The cells were mixed with the bioink homogeneously by pushing and retracting the piston of the syringe multiple times, ending with the mixed solution in the cartridge. The mixed bioink was then directly installed to the bioprinter ready for bioprinting.

3.2.3 Bioprinting

Before bioink preparation, the Inkredible+™ bioprinter (Cellink AB, SWE) (Fig. 6 A) was prepared for bioprinting. Therefore, the pressure was adjusted according to the used bioink (47 - 70 kPa for Alginate-POx and 35 - 60 kPa for Cellink® Bioink) using the pressure valves (5) and the pressure indicators (1). Following, the axes were homed using an empty cartridge with a printing nozzle (7) installed to the printer. The homing was performed with a 3D-printed adapterplate (8) and the culture device, like a petri dish (Fig. 6 C) or 3D-printed tissue container (Fig. 6 D), installed. After homing, the bioink-cartridge (6) with cells was installed with a sterile nozzle (410 µm) (Nordson EFD, USA) into the printer. Next, the valve of the printer was toggled open and close manually to fill the nozzle with bioink material and to test the pressure settings. After all, the bioprinting process was started for the related Gcode. Due to heterogeneous behavior of the inks and temperature fluctuations, the printing pressure had to be readjusted during the process individually.

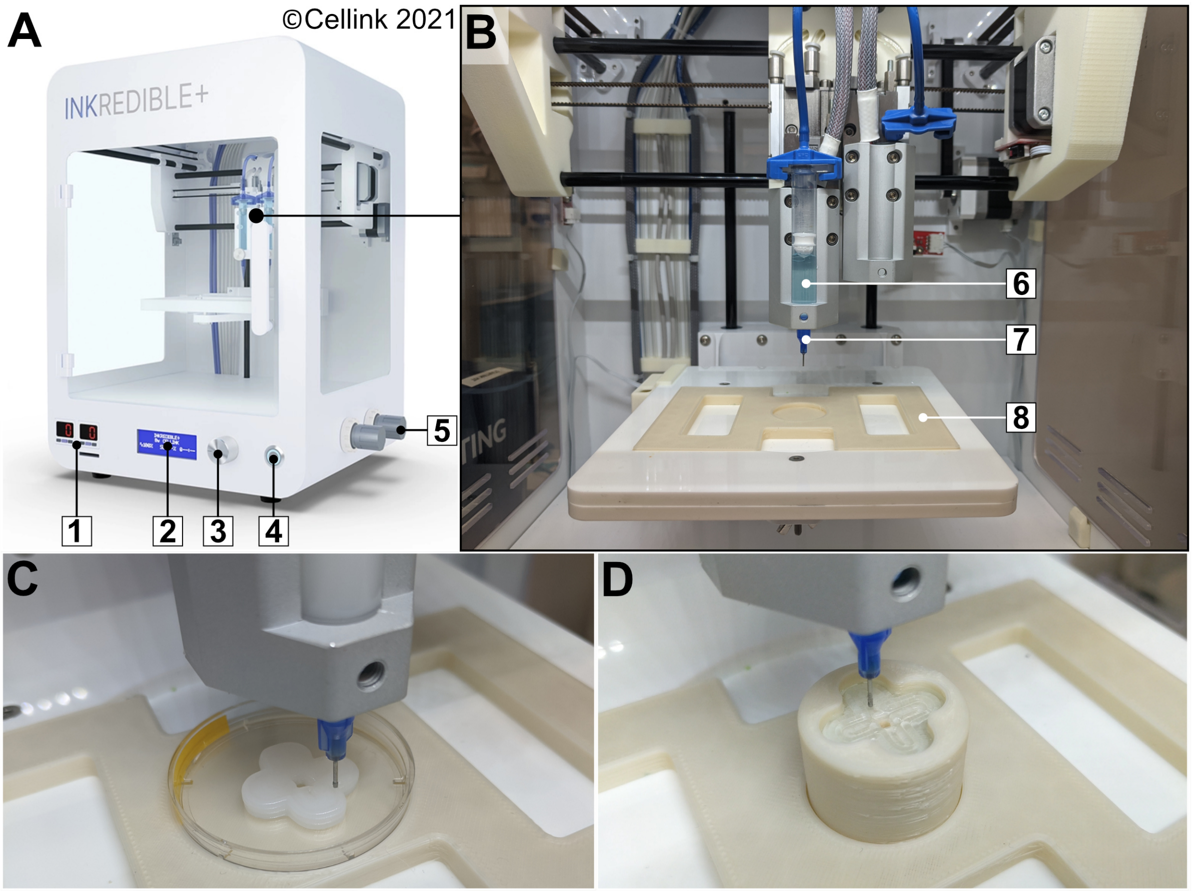

Figure 6: Bioprinting setup. (A) Inkredible+^{TM} bioprinter with indicated control units like pressure indicators (1), main screen with menu (2), navigation button (3), On/Off button (4) and pressure adjustment wheels (5). Image adapted from Cellink homepage [124]. **(B)** Bioprinter interior with indicated bioink cartridge (6), nozzle (7), and 3D-printed printbed adapter (8). **(C)** Printing of Cellink® Bioink into a petri dish. **(D)** Printing of Cellink® Start hydrogel into tissue container.

Once the printing process was completed, the container with the biofabricated construct was transferred to the clean bench and 1 - 2 ml crosslinking agent (Cellink AB, SWE) was applied on top of the biofabricated construct for 30 min. This way, the tissue was crosslinked with calcium ions. The tissue container was then transferred to the bioreactor system for dynamic culture of the biofabricated construct.

3.3 Computer Aided Design

Computer aided design was performed with Solidworks® Premium 2017 (Dassault Systèmes, France). Geometries used for computational fluid dynamics (CFD) simulation were saved as SLDPRT- or SLDASM-filetype and for 3D printing as STL-file.

3.4 3D Printing and Post-Processing

FDM printing was performed by transferring the STL-file into machine-specific Gcode using ideaMaker software (Raise3D Technologies Inc., USA). Therefore, printing parameters were set to 0.4 mm nozzle diameter, 200 µm layer height, 220 °C printing temperature, 60 °C printbed temperature, 50 mm/s printing speed and 33 % honeycomb infill ratio and type. Parts were printed with lignin-based material (Green-TEC Pro Filament - Nature, FD3D GmbH, AUT) by Raise3D Pro 2 printer (Raise3D Technologies Inc., USA). If required, support structure was removed mechanically after printing.

For SLA printing, STL-files were transferred to machine-specific Gcode using Preform software (Formlabs Inc., USA). For printing parameters, the predefined settings of the different materials were used. Layer height was set to 50 µm. Parts were then printed using Form 2 printer (Formlabs Inc., USA). After printing, uncrosslinked resign was removed by washing the parts with isopropanol (Carl Roth GmbH, Germany) according to the company protocol using Form Wash device (Formlabs Inc., USA) and subsequently cured with UV-light using Form Cure device (Formlabs Inc., USA) also according to protocol.

SLS was realized by transforming the STL-file into machine-specific Gcode using Sinterit Studio 2019 software (Sinterit sp. z o.o., PL). For printing Nylon-12-based material (PA12 Smooth, Sinterit sp. z o.o., PL), layer height was set to 125 µm, chamber temperature to 178 °C and laser power to 1.67 W. After printing the parts with Sinterit Lisa Pro printer, they were sandblasted using Sinterit sandblaster device (both Sinterit sp. z o.o., PL).

3.5 Analysis of Printing Accuracy and Limitations

After printing, the test bodies for accessing printer accuracy were imaged using light microscope EVOS XL (Thermo Fisher Scientific Inc., GER). Following, the pictures were processed by self-written Fiji (ImageJ) macros (Fig. 11, p. 54) to quantify X,Y and Z resolution (Code 1, p. 120) as well as feret diameter (largest diameter) and roundness factor of the channels (Code 2, p. 120). Angles were measured manually using the implemented angle measuring tool. Leakage was quantified by filling the related test bodies with 1 ml of water, followed by an incubation in a closed petri dish for 24 h. Weight was measured empty, filled, and after incubation and the relative amount of the remaining water calculated finally.

3.6 Sterilization Methods

Autoclaving was performed at 121 °C for 15 min by DX-45 autoclaving device (Systec GmbH, GER). Total process time was 1.5 h. For autoclaving, the parts were placed into autoclaving bags in order to ensure sterility after removing from the autoclaving device.

Second, vaporized hydrogen peroxide plasma treatment (VH_2O_2) was used as sterilization method as well. Therefore, the plasma cleaner device Pico P100 (Diener electronic GmbH & Co. KG, GER) was used. After preheating the chamber with oxygen plasma induced by 500 W at 0.3 bar and a flow of 12 standard cubic centimeters per minute (sccm) for 15 min, the foil-wrapped (Stericlin®, Vereinigte Papierwarenfabriken GmbH, GER) parts were placed into the chamber. A vaporizer unit was filled with 1.5 ml 60 % H_2O_2 (Thermo Fisher Scientific, GER) and also placed into the chamber, followed by an evacuation of the chamber to 4 mbar. After 75 min, the chamber was further evacuated to 0.4 mbar, plasma was induced at 300 W for 4 min. Then, the athmosphere was replaced with pure oxygen and plasma was induced a second time at 300 W for 5 min. At the end, the chamber was flooded with pure oxygen for 120 s and replaced by normal air afterwards. According to our results on biocompatibility, as described in section 4.1.3 (p. 59), plasma-sterilized parts were not used for direct cell contact experiments within the first two weeks after sterilization.

3.7 Mechanical Analysis

Quantification of the mechanical properties of a material was accessed by tension and bending tests using the material testing machine Z010 (Zwick Roell AG, GER). Tests were conducted referring to DIN EN ISO 527 [125] and 178 [126]. For all tests, a 10 kN measuring unit and a speed of 5 mm/min were used. Four-point-bending test was performed with a support span of 40 mm and a span length of 10 mm. Tensile and flexural strength were recorded and calculated using the related machine software testXpert II V3.1 (Zwick Roell AG, GER).

3.8 Biocompatibility Test

Examination of the biocompatibility of materials was adapted from DIN EN ISO 10993-5 [127]. First, squared platelets with an edge length of 1.72 cm and a thickness of 2 mm (about 6 cm^2 surface) were manufactured of the related materials, either 3D printed, as described in section 3.4, or casted as described in section 3.9.2. After that, the platelets were submerged for 24 h in ultra pure water for cleaning. They were autoclaved or plasma sterilized the next day as described in section 3.6 depending on the experiment, and incubated with D10 medium by a ratio of 1 ml per platelet. After 24 h incubation with the material, the medium was separated from the material and stored at 4 °C until usage.

At day one, 5 wells of a clear bottom 96 wellplate (Greiner Bio-One, GER) were seeded with 10.000 C2C12 cells for every material to be tested and filled up to 200 µl with D10 medium. For positive and negative control, additional wells were seeded the same way. The cells were incubated until the next day. Day two, the medium was replaced with 200 µl of the material-treated medium. For positive control, fresh D10 medium was used and 1 % SDS, solved in ultra pure water, as negative control. At the third day, the wells were washed with PBS$^-$ once and filled with 100 µl of D10 medium. Then, 100 µl of CellTiter-Glo® Luminescent Cell Viability Assay solution (Promega, GER) was added to each well. Luminescence quantification was done by a Tecan plate reader (Tecan Trading AG, CH): The wellplate was shaked first for 120 s at an amplitude of 2.5 mm and then incubated at RT for 10 min before the luminescence was measured. For analysis positive control was defined as 100 %.

3.9 Bioreactor System

3.9.1 Computational Fluid Dynamics Simulation

CFD simulations show a powerful tool for *in silico* and non-invasive prediction of physical behaviors like 3-dimensional flow field, shear stress, specimen concentration or similar. The equations used for this are based on the laws of mass conservation and momentum balance, which is also refereed to as 'Navier-Stokes equation' and continuity equation [128, 129]. CFD simulations were performed using finite element method software COMSOL Multiphysics (COMSOL Multiphysics GmbH, GER). To do so, a geometry-part of the medium-filled interior of the bioreactor was created by CAD, as described in section 3.3, and imported together with the tissue geometry file into the software and meshed to an extremely fine mesh size. Material of the tissue and medium part was defined as water.

For characterizing the medium flow velocity, as well as the shear stress, built-in Reynolds-averaged Navier-Stokes k-ϵ turbulence flow model was used in a steady-state study. Medium mass inflow was set to $1.5\,\mathrm{g/min}$ which was empirically measured for a pumping speed of $5\,\mathrm{rpm}$ at the device.

Glucose concentration within the tissue was calculated by using the built-in transport of diluted specimen (TDS) model in a steady-state study. Initial concentration of the tissue part was set to $0\,\mathrm{mol/m^3}$ and the medium to $25\,\mathrm{mol/m^3}$ (equals 4.5 mg/l glucose of D10 medium (Tab. 6, p. 32)). Diffusion coefficient of glucose in water was taken from Stein *et al.* [130] and set to $6 \times 10^{-10}\,\mathrm{m^2/s}$. The elimination rate of the glucose was adapted from Ahn *et al.* [131] and calculated to $-1.157 \times 10^{-4}\,\mathrm{mol/m^3\,s}$ (glucose consumption of 3×10^6 cells/ml).

3.9.2 PDMS Casting

To manufacture bioreactor parts made from poly(dimethylsiloxane) (PDMS) Sylgard$^{\mathrm{TM}}$-I 184 two-component Silicone (DOW Silicone Deutschland, GER), first the required geometry was designed as described in section 3.3 (Fig. 7 A) and SLA-printed with resin Model V2 (Formlabs, USA) as described in section 3.4 (Fig. 7 B). Two-component Dublisil® 15 (Dreve Deutschland, GER) was mixed by a ratio of 1:1 according to manufacturer protocol and used to create a negative mold of the printed part (Fig. 7 C).

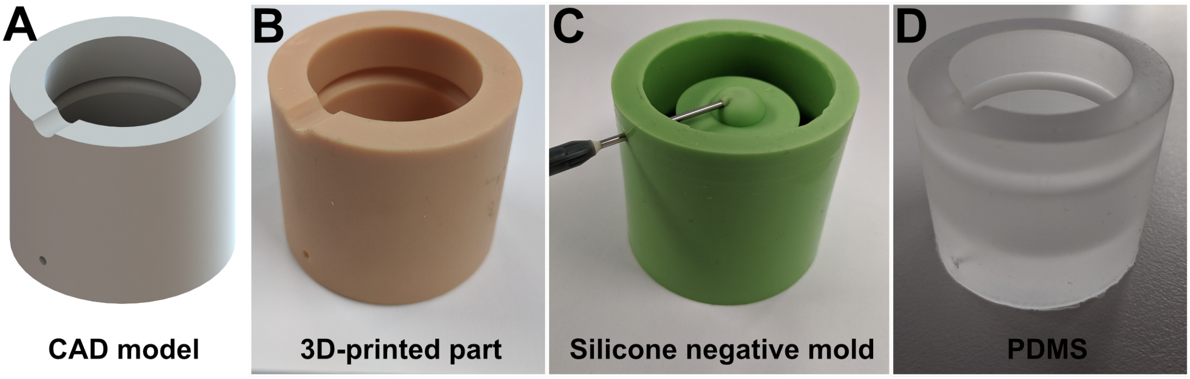

Figure 7: Stages of the PDMS manufacturing process. (A) CAD Model of a bioreactor part that is meant to be made from PDMS. **(B)** 3D-printed part made from Resin Model V2. **(C)** Negative mold of the 3D printed geometry, casted by Dublisil® 15 silicone. Stainless steel injection cannulas were applied to create channels within the final PDMS part. **(D)** Final PDMS casted part with channels.

To remove trapped air bubbles, the liquid mold was exposed to vacuum for a few seconds using a vacuum casting machine (J. Schüchel®, GER). After 30 min at RT the Dublisil® 15 was solidified and the printed part was separated from the negative mold. The negative mold was then vacuum-treated for 24 h to ensure full crosslinking of the Dublisil® 15 and reduce the amount of enclosed air within the mold. Sylgard™-I 184 was mixed to a ratio of 1:10 according to manufacturer protocol, followed by a vacuum-induced evacuation of air bubbles. When the air bubbles were completely removed from the PDMS, the negative mold was plasma activated: First, Stainless steel injection needles were applied to the mold to create channels within the later PDMS casted part. Then, the mold was plasma-treated using a plasma cleaner device Pico P100 (Diener electronic GmbH & Co. KG, GER). Therefore, the chamber was flooded with oxygen gas, evacuated to 0.3 mbar, and plasma induced by 500 W for 2 min. The atmosphere in the chamber was replaced with air and the mold removed from the plasma device. Next, PDMS was filled into the mold and crosslinked at 70 °C for 3 h. After that, the solidified PDMS part (Fig. 7 D) was removed from the mold and finally cured at 130 °C for 30 min. Alternatively, autoclaving, as described in section 3.6, could be performed on the parts once for final crosslinking. At the end, the parts were soaked in ultra pure water to remove uncrosslinked monomeres and autoclaved before using for experiments.

3.9.3 Dynamic Culture

For dynamic tissue culture, a specialized incubator, selfmade by the chair of Tissue Engineering and Regenerative Medicine (TERM, University Clinics Würzburg, GER) (Fig. 8), was used. The integrated temperature and and atmospheric control was set to 37 °C and 5 % CO_2. Humidity control was not implemented in this system. After the bioreactor was assembled and filled with medium, it was placed into the incubator and installed to a built-in peristaltic pump.

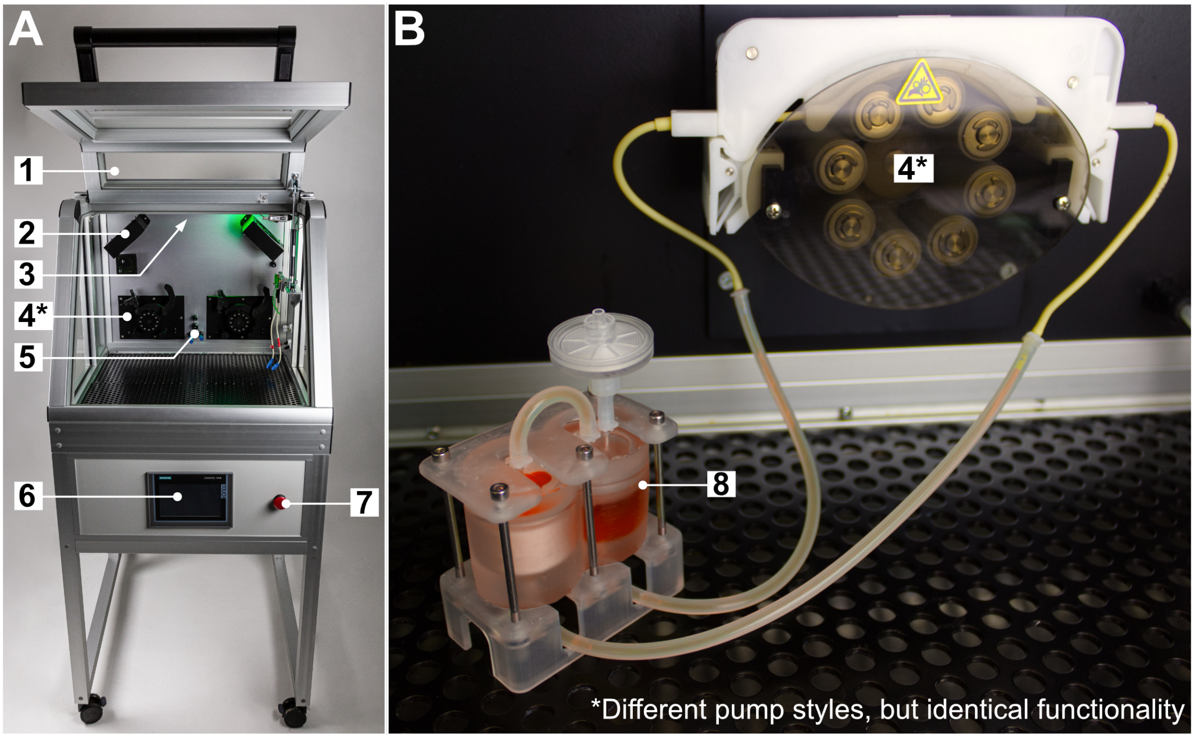

Figure 8: Dynamic perfusion culture setup. (A) Self-made Incubator system made by TERM with lid (1), ventilators for air circulation (2), heating plate (3), integrated peristaltic pumps (4) (* indicates different pump styles with identical functionality), sensors for temperature and CO_2 (5), touch screen control unit (6) and emergency stop switch (7). **(B)** Incubator interior with bioreactor (8) installed to the integrated pump (4).

Pump speed was then set to 5 rpm, equally to 1.5 ml/min. Media exchange was performed weekly by removing the full medium from the reservior compartment. The medium within the tube system and the tissue chamber remained in the bioreactor. New medium was then filled into the reservior. After culture, the bioreactor parts were separated and soaked in fully demineralized water (FD water) for 24 h. 3D-printed tissue container was discarded as it is stated to be single-use only. The next day, the bioreactors parts were cleaned using an ultra sonic bath at 60 °C for 1 h.

3.10 Media Analysis

To quantify the concentration of glucose, lactate and lactate dehydrogenase (LDH) of the medium, 500 µl of the medium were transferred from the cell culture to a 1.5 ml reaction vessel and analyzed in the Cedex Bio Analyzer (F. Hoffmann-La Roche AG, CH)). Glucose Bio (6343732001), Lactate Bio (6343759001) and LDH Bio Kit (6343767001) were used for this analysis and fresh medium was used as a control.

3.11 Vitality Assessment

3.11.1 Life/Dead Staining

For fluorescent Life/Dead characterization of the bioprinted constructs LIVE/DEAD^{TM} Kit (Life Technologies Corp., USA) was used. First, the constructs were washed with PBS^{-} and transferred to a glass bottom petri dish. According to the manufacturer protocol, 1.5 µl calcein and 6 µl ethidium homodimer were diluted in 3 ml of PBS- and applied to the constructs. Following, the constructs were incubated in a dark environment at RT for 45 min and then washed again with PBS-. They were then visualized using an IF-microscope equipped with a 470 nm-filter for calcein (viable cells) and a 545 nm-filter for ethidium homodimer (dead cells).

3.11.2 Qualitative Viability Assay

Qualitative viability assay was done by 3-(4,5-dimethylthiazol-2-yl)-2,5-diphenyltetrazolium bromide (MTT) (Sigma-Aldrich, GER) assay. Therefore the constructs were transferred to a wellplate and submerged in MTT solution (1 mg/ml in cell culture medium). After 3 h of incubation at 37 °C, the MTT solution was discarded and the constructs were washed with PBS^+ twice. Finally, pictures of the constructs were taken for qualitative characterization.

3.12 Histological Analysis

3.12.1 Fixing and Embedding

Prior to histological staining, the constructs were fixed with Roti-Histofix® 4 % (PFA) (Carl Roth, GER) and embedded in paraffin. To do so, the constructs were removed from the bioreactor and transferred to a 50 ml centrifugation tube filled with PFA + 0.3 M $CaCl_2$. $CaCl_2$ was added to prevent dissolving of the construct during fixation.

This way they were incubated on a rocking shaker at RT for 3 h (1 h per mm of thickness). After that, the fixed constructs were placed in an embedding cassette with a filter paper and submerged in tap water. Then they were transferred into an automated embedding center (Leica Camera AG, GER) for dehydrating and paraffin embedding. The protocol of the embedding center is depicted in table 9. After paraffin embedding, the constructs were transferred from the embedding cassettes to stainless steal molds and casted into a paraffin block.

Table 9: Protocol for embedding center

Step	Solution	Time	Temp.
#1	Tap water	2 h	RT
#2	50 % Ethanol	2 h	RT
#3	70 % Ethanol	2 h	RT
#4	90 % Ethanol	2 h	RT
#5	96 % Ethanol	2 h	RT
#6	Isopropyl alcohol	2 h	RT

#7	Isopropyl alcohol	2 h	RT
#8	Isopropyl alcohol / Xylene (1:2)	2 h	RT
#9	Xylene	2 h	RT
#10	Xylene	2 h	RT
#11	Paraffin	2 h	60 °C
#12	Paraffin	2 h	60 °C

3.12.2 Hematoxylin and Eosin Staining

For histological staining, slices of 5 µm thickness were cut from the paraffin-embedded construct using a microtome and transferred to polylysine-coated glass slides. This slides were then stored at 37 °C over night. The next day, the slides were transferred to 60 °C for 1 h to liquefy the paraffin. After that, the slides were rehydrated and stained with hematoxyline and eosin (both Morphisto GmbH, GER) by submerging in the corresponding baths as depicted in table 10. Afterwards the slides were again dehydrated in baths with increasing alcoholic concentration, and finally covered by a coverslide using Entelan® (Merck, GER) as a mounting medium.

Table 10: HE staining protocol

Step	Solution	Time	Description
#1	Xylene	10 min	Deparaffining
#2	Xylene	10 min	Deparaffining
#3	96 % Ethanol	1 min	Rehydration
#4	96 % Ethanol	1 min	Rehydration
#5	70 % Ethanol	1 min	Rehydration
#6	50 % Ethanol	1 min	Rehydration

#7	Hematoxylin	7 min	Apply staining to nuclei
#8	FD water	Dip	Washing
#9	Tap water (rinsing)	7 min	Coloring nuclei
#10	Eosin	7 min	Staining cytoplasm and matrix
#11	FD water	Wash	Washing
#12	70 % Ethanol	2 min	Dehydration
#13	Isopropyl alcohol	5 min	Dehydration
#14	Isopropyl alcohol	5 min	Dehydration
#15	Xylene	5 min	Dehydration
#16	Xylene	5 min	Dehydration

3.13 Statistical Analysis

Calculations and statistical analysis were conducted using GraphPad Prism 6 and 9 (GraphPad Software, USA) and Microsoft Excel 365 (Microsoft, GER). The data and values are visualized as mean ± standard deviation. Unpaired t-test was used to calculate significances and are indicated by * for $p \leq 0.05$.

4 Results

4.1 Determination of 3D Printer Capabilities and Limitations

A majority of the figures and results in this section have already been published earlier by Gensler and Leikeim *et al.* [67] and are repeated here for your convenience.

4.1.1 Test Body Design

A broad study was performed in a first step to characterize the three most commonly used printing techniques like FDM/FFF, SLA, and SLS for their capabilities and limitations considering the simultaneous printing of bioreactor and biofabricate. To do so, a set of test bodies was designed by CAD as explained in section 3.3, for investigating a variety of geometrical parameters (Fig. 9).
One test body was designed for the assessment of the resolution on the basic X- and Y-axis. It was designed by a group of small bars with different widths on a block. It was then duplicated and rotated by 90° so that one of them was printed in X-direction and the other one in Y-direction. A second test body, similar to the first one, was designed with all bars showing the same width, but different heights. This test body was used to investigate the resolution of the Z-axis of the printer, which is closely correlating to the amount of layers the geometry is printed of. Since channels are an important geometry for perfusion bioreactors, a next test body was designed as a block, holding an arrangement of channels of different diameters. It was again duplicated and tilted accordingly, so that the channels were printed horizontally with one of the test bodies and vertically with the other one. Since printing and removing support structures in 3D printing sometimes shows a crucial challenge, an other test body was designed to investigate the printing of floating structures without support. Overhanging angles were printed on a bar to investigate the limiting angle. An other important parameter for printing bioreactors is the tightness and leakage-proof of such a system. A set of squared cups was printed with different wall thicknesses and an constant inner volume of 1.2 ml. [67]
By using the built-in volume measurement tool in SolidWorks® 2017 it could be shown, that transferring the original file-data into STL-file format did not changed the volume of the test bodies and therefore no loss of accuracy could determined in this step.

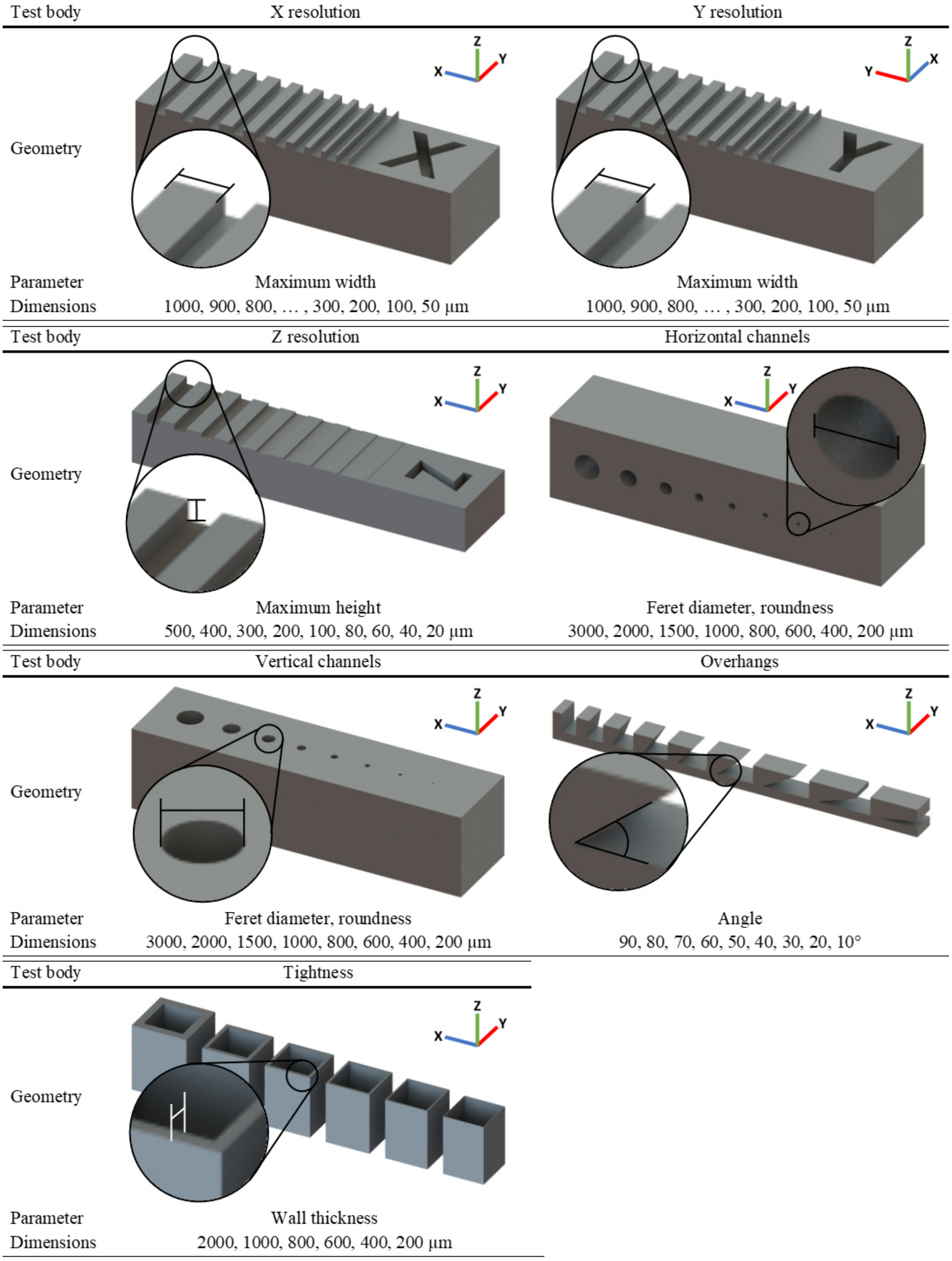

Test body	X resolution	Y resolution
Geometry		
Parameter	Maximum width	Maximum width
Dimensions	1000, 900, 800, … , 300, 200, 100, 50 µm	1000, 900, 800, … , 300, 200, 100, 50 µm

Test body	Z resolution	Horizontal channels
Geometry		
Parameter	Maximum height	Feret diameter, roundness
Dimensions	500, 400, 300, 200, 100, 80, 60, 40, 20 µm	3000, 2000, 1500, 1000, 800, 600, 400, 200 µm

Test body	Vertical channels	Overhangs
Geometry		
Parameter	Feret diameter, roundness	Angle
Dimensions	3000, 2000, 1500, 1000, 800, 600, 400, 200 µm	90, 80, 70, 60, 50, 40, 30, 20, 10°

Test body	Tightness
Geometry	
Parameter	Wall thickness
Dimensions	2000, 1000, 800, 600, 400, 200 µm

Figure 9: Testbodies for quantifying printer capabilities. CAD geometries and parameters are shown here for the individual test bodies used for analyzing printer tolerances and limitations. Individual test bodies were designed for X- and Y-resolution, Z-resolution, horizontal and vertical channels, as well as floating angles and wall thickness for leakage investigation. Figure taken from Gensler and Leikeim *et al.* [67].

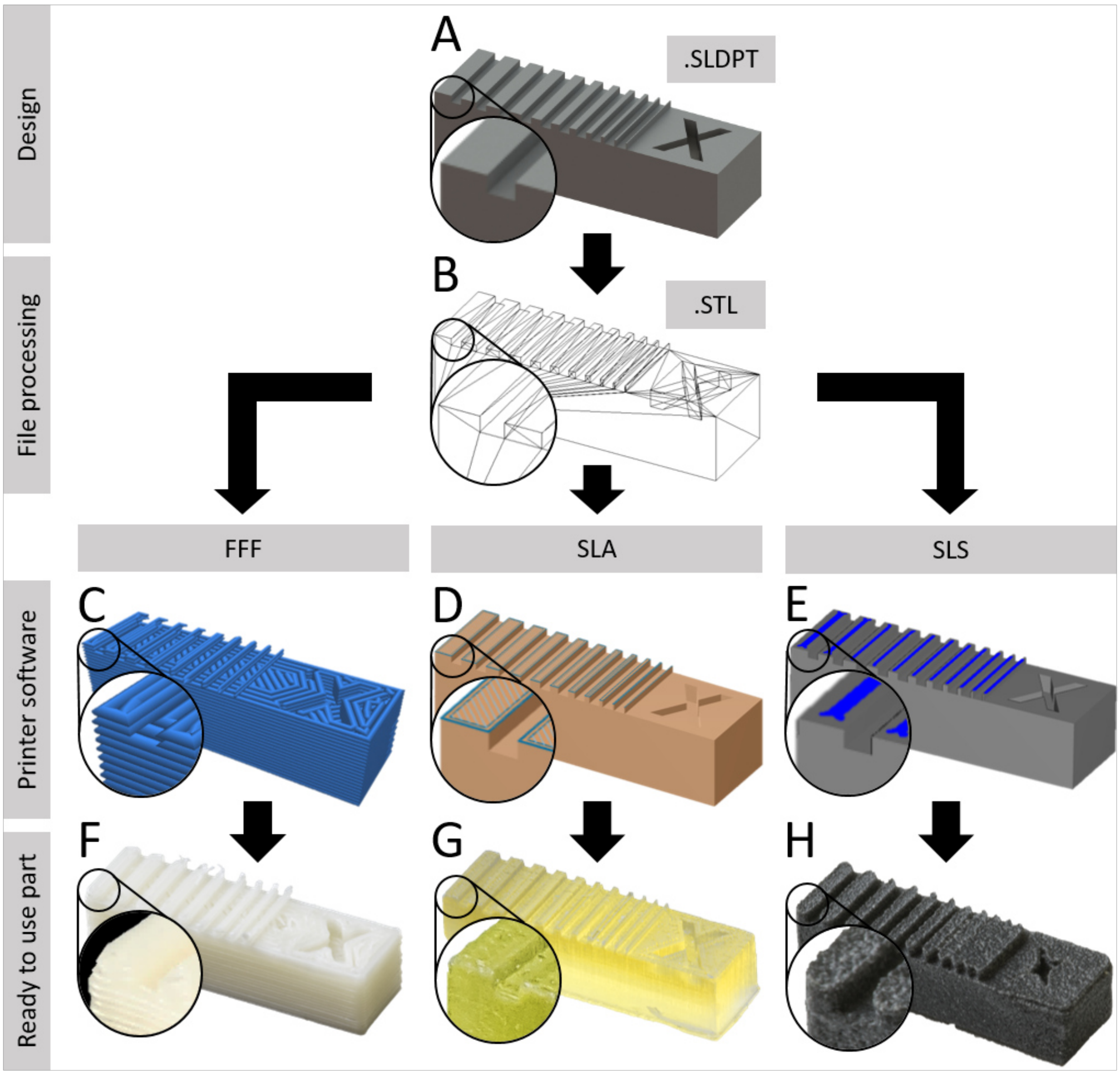

Figure 10: Processing of CAD-files to printed parts (example X-resolution test body). All test bodies were designed in Solidworks® 2017 software **(A)** and converted into STL-file format **(B)**. The STL-file was then processed into the device-specific Gcodes using the respective company owned software for the FFF printers **(C)**, SLA printer **(D)** and the SLS printer **(E)**. The resulting printed part after post-processing (ready to use) shows significant differences in surface quality and accuracy **(F-H)**. The nozzle or laser path is shown in blue. Figure taken from Gensler and Leikeim *et al.* [67].

In a next step, the test bodies were processed with the respective software of the different 3D printers, as explained in section 3.4. The results are shown in figure 10 for the X-resolution test body as an example. After slicing the test body with the FDM/FFF printer software, the movement of the printer nozzle was visualized, showing that there is loss of information due to the software ignoring geometries less than 200 µm. [67]

Table 11: Printer settings and parameters used for test body printing.

Printer	**Raise3D Pro 2**	**Ultimaker 3**	**Ultimaker S5**	**Form 2**	**Lisa Pro**
Method	FFF	FFF	FFF	SLA	SLS
Software (file format)	ideamaker 3.4.2 (.gcode)	Ultimaker Cura 4.2.1 (.gcode)	Ultimaker Cura 4.3 (.gcode)	Preform 3.0.1 (.form)	Sinterit Studio 2019 1.4.5.0 (.scode)
Company (printer)	RAISE3D Technologies, USA	Ultimaker B.V., Netherlands	Ultimaker B.V., Netherlands	Formlabs Inc., USA	Sinterit sp. z o.o., Poland
Printed material	Green-TEC Pro Filament, Natur, 1.75 mm	Green-TEC Pro Filament, Natur, 2.85 mm	Green-TEC Pro Filament, Natur, 2.85 mm	Dental SG Resin	PA12 Smooth
	(Lignin based*)	(Lignin based*)	(Lignin based*)	(Bisphenol A ethoxylate based*)	(Nylon 12)
Company (material)	Extrudr | FD3D GmbH, Austria	Extrudr | FD3D GmbH, Austria	Extrudr | FD3D GmbH, Austria	Formlabs Inc., USA	Sinterit sp. z o.o., Poland
Basic printing parameter	Nozzle diameter: 0.4 mm	Nozzle diameter: 0.4 mm	Nozzle diameter: 0.4 mm	Laser diameter: 140 µm	
	Layer height: 200 µm	Layer height: 100 µm	Layer height: 100 µm	Layer height: 50 µm	Layer height: 125 µm
	Printing temp: 220°C	Printing temp: 220°C	Printing temp: 220°C	Printing temp: 30.5°C	Chamber temp: 178°C
	Printbed temp: 60°C	Printbed temp: 60°C	Printbed temp: 60°C	Laser power: 0.25 W	Laser power: 1.67 W
	Standard speed: 50 mm/s	Standard speed: 70 mm/s	Standard speed: 70 mm/s		
	Outer shells: 4	Outer shells: 8	Outer shells: 4		
	Infill ratio: 33%	Infill ratio: 20%	Infill ratio: 15%		
	Infill type: Honeycomb	Infill type: Honeycomb	Infill type: Triangle		

Fused filament fabrication (FFF), stereolithography (SLA), selective laser sintering (SLS), temperature (temp).

*Since materials for printing are complex composites, we only show the main component here.

Table taken from Gensler and Leikeim *et al.* [67].

This is of cause depending on the actual printing settings used (Tab. 11) and can be adjusted if necessary. Since this apporach also included reduction of printing time, the printing settings were adjusted to a compromise of different aspects which are explained in detail later in this section. Since SLA and SLS are laser-based printing techniques the software showed the laser movement rather than the nozzle movement as in FDM/FFF. In SLA, it can be seen, that the software did not ignored any geometries independent of their dimension and the laser settings. SLS printer software instead shows a significant offset from the actual geometry to the visualized laser path, indicating a relative large laser diameter. This is also shown in the final printed part (Fig. 10 H) by rounded edges of the bars and fusing of multiple smaller bars into each other. SLA shows a final part that is closely related to the digital geometry with a high surface quality, while FDM/FFF clearly shows a layered surface. [67]

4.1.2 Analysis of Individual Printing Techniques

Due to the simple shape of the test bodies, they could be visualized and imaged using a standard light microscope. The images of the test bodies were then processed via two self-written macros within ImageJ, as explained in section 3.5. The functionality of the macros (Code 1, p. 120 and Code 2, p. 120) is explained in Gensler and Leikeim *et al.* [67] and shown in figure 11:

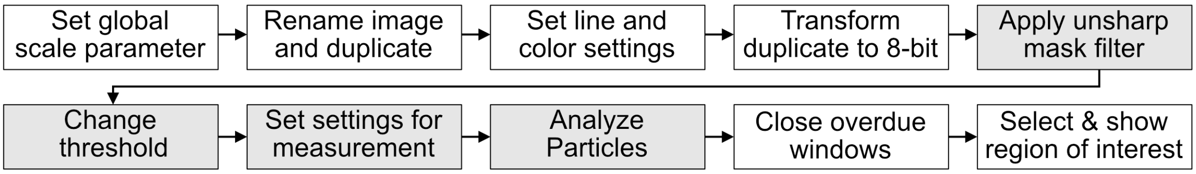

Figure 11: Flowchart of the functionality of the ImageJ macros.

First, the area of interest was cropped and set to 8-bit grayscale. Subsequently, an unsharp mask filter was applied to increase contrast, followed by a grey level threshold (RenyiEntropy) to reduce noise. At the end, the particle analyser tool identified the shape of the area of interest. SLA-printed parts in fact showed increased artifacts due to irregular light conditions caused by transparency of the material. Therefore, the RenyiEntropy filter had to be adjusted individually [67].

The visual feedback of the macros is shown in figure 12. For the X- and Y-test body the maximal width was measured by the macro, as well as the maximal height of the Z-test body.

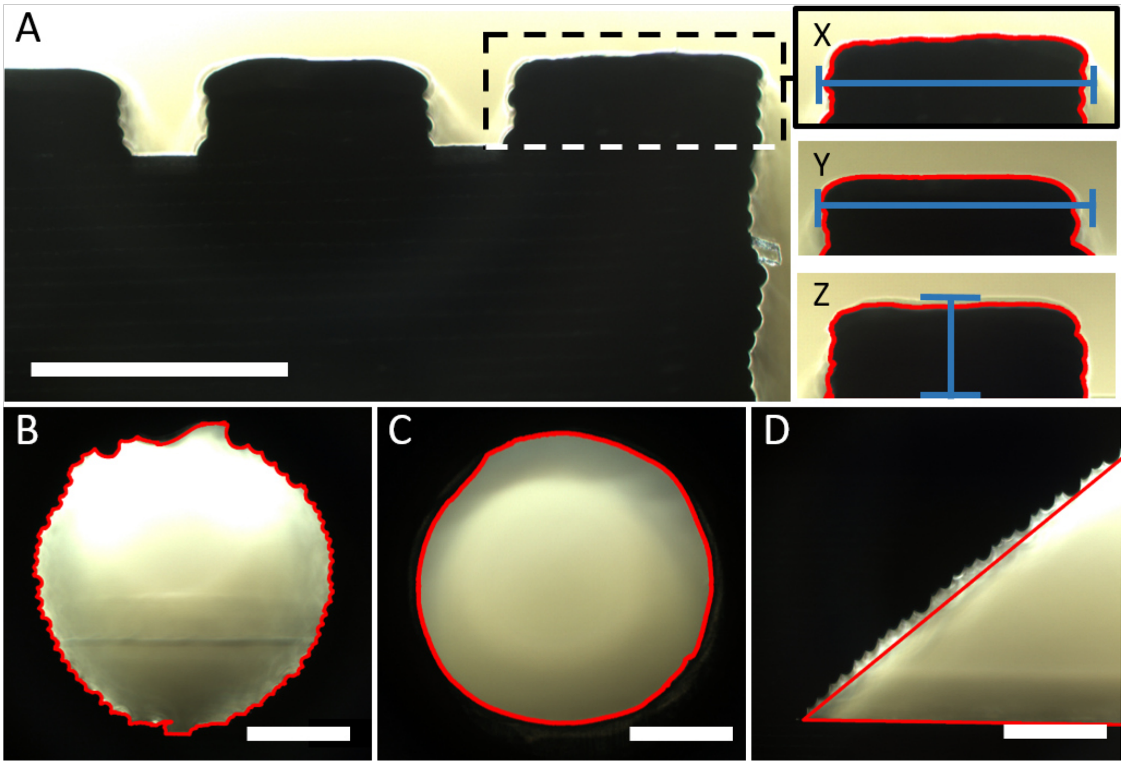

Figure 12: Evaluation of printed test bodies using ImageJ macros. Microscopic images of the test bodies were taken and the area of interest was cropped (dotted line). The shape was identified and analyzed using self-written Fiji macros (red line). **(A)** For X- and Y-resolution test bodies **(X and Y)** the maximum width, and for the Z-resolution test body **(Z)** the maximum height was measured (blue line). For the horizontal-printed channels **(B)**, as well as the vertical-printed channels **(C)**, the feret diameter and the roundness was calculated. **(D)** The angle of the according test body was measured manually using the angle measuring tool from ImageJ (red line). Scale bar equals 1000 µm. Figure taken from Gensler and Leikeim *et al.* [67].

The channels were quantified for their feret diameter (largest diameter) and the roundness factor. Floating overhangs were measured manually using the built-in angle measurement tool of ImageJ. Leakage-proof was investigated by calculating the remaining weight of the printed cups, after they were filled with fully demineralized water as explained in section 3.5. After processing and quantification of the test body parameters, the printing techniques were compared to their relative accuracy (Fig. 13) to the original designed value. A positive value means, that the resulting shape was thicker, higher or broader than the original one and vise versa. This also means, that a relative deviation closer to 0 % indicates a higher correlation from resulting part to the designed shape. The individual results are already stated in Gensler and Leikeim *et al.* [67] and repeated here for your convenience:

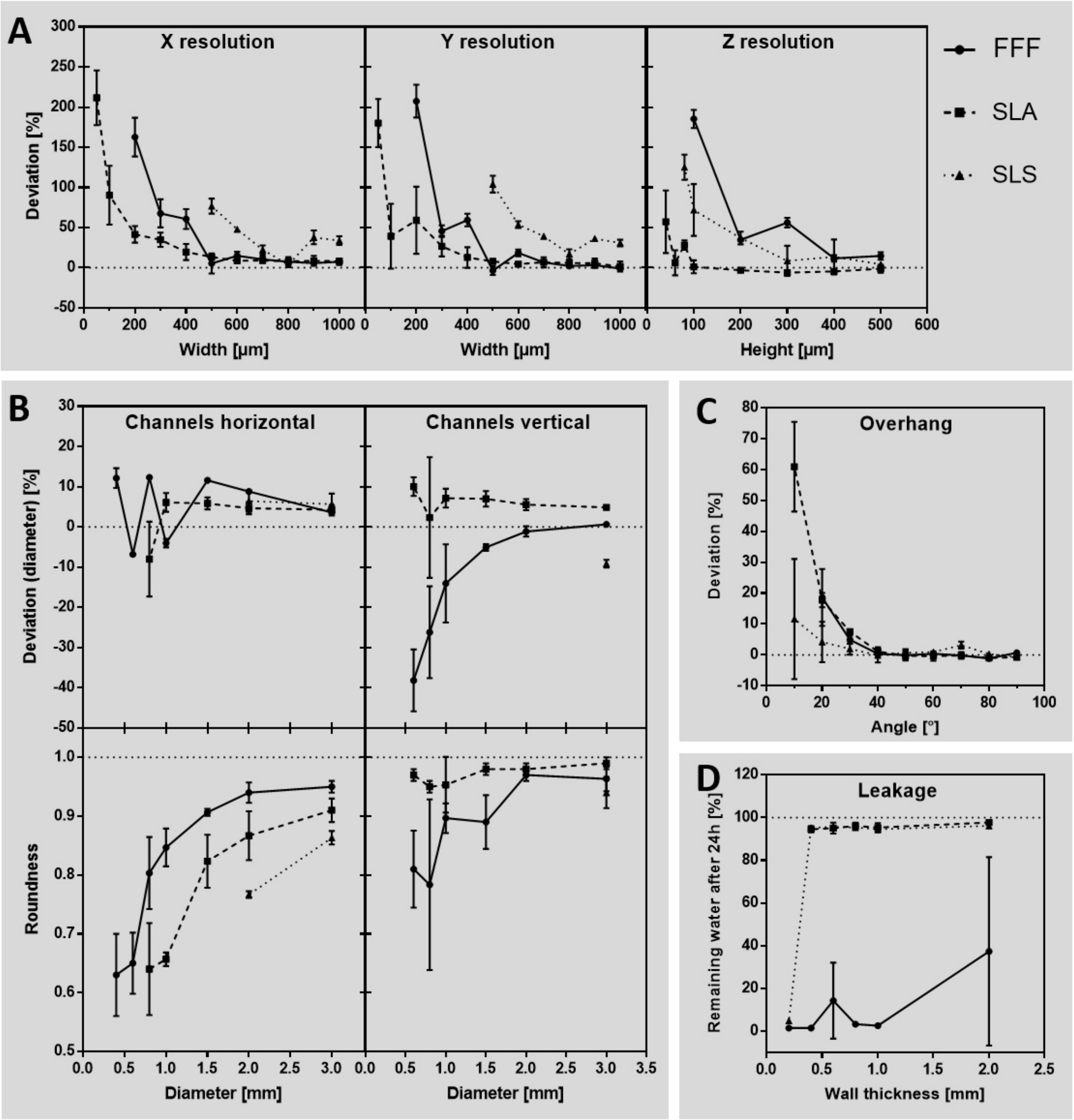

Figure 13: Accuracy of different 3D printing methods compared to each other. Test bodies printed with FFF (Raise3D Pro 2 printer), SLA (Form 2 printer) and SLS (Lisa Pro printer) technique were analyzed to their deviation of the respective geometry that was designed by CAD before. **(A)** Accuracy of the base axes X, Y and Z. **(B)** Diameter and roundness of horizontally and vertically printed channels. **(C)** Angled overhangs, printed without support structures. **(D)** Leakage investigated for different wall thicknesses. n = 3. Figure taken from Gensler and Leikeim *et al.* [67].

"Comparing X and Y resolution, all three techniques showed exponential increase of accuracy deviation by decreasing parameter dimensions of the test bodies. Thereby, SLA achieved the lowest deviation compared to FFF and SLS, especially in dimensions smaller than 500 µm. While FFF did not print dimensions below 200 µm at all, SLA and SLS printed every structure of the test body, resulting in very high deviations for small dimensions. Especially in SLS, the resulting geometries were printed so thick that they fused into each other, which made it impossible to analyse them below 500 µm. By analysing the Z resolution, SLA also had the lowest deviation compared to FFF and SLS. Inaccuracy increased exponentially in heights below 100 µm, resulting in an oscillating deviation of 28.3 ± 4.8 % at 80 µm, 6.1 ± 12.7 % at 60 µm and 57.3 ± 31.8 % at 40 µm height. Heights below 40 µm were not printed by SLA. FFF did not print below 100 µm and SLS stopped printing at 80 µm. As SLS showed the lowest accuracy in the base axes, horizontal channels were only printable down to 2000 µm diameter. SLA achieved channels down to 800 µm diameter and FFF down to 400 µm. SLA-printed channels had a stable average deviation of 5.2 ± 0.8 % from 3000 to 1000 µm diameter and then falling to −8.0 ± 7.6 % at 800 µm. FFF instead showed a linear increase of deviation from 3.6 ± 0.7 % at 3000 µm, down to 11.6 ± 0.5 % at 1500 µm diameter. Then it had oscillating deviations of −4.0 ± 0.9 % (1000 µm), 12.3 ± 0.1 % (800 µm), −6.8 ± 0.4 % (600 µm) and 12.2 ± 2.0 % (400 µm). Roundness of horizontally printed channels revealed an exponential decrease in FFF and SLA (SLS only 2 dimensions measurable). Starting at 0.95 ± 0.01 for FFF and 0.91 ± 0.02 for SLA at 3000 µm diameter values decreased to 0.63 ± 0.06 at 400 µm (FFF) and 0.64 ± 0.06 at 800 µm (SLA). Similar to horizontal channels, SLS was only able to generate channels of 3000 µm diameter in vertical direction, with a deviation of −9.1 ± 0.8 %. SLA was able to print channels down to 600 µm diameter, showing again a stable average deviation of 6.1 ± 1.0 % from 3000 µm down to 1000 µm diameter. Then accuracy decreased to 2.3 ± 12.3 % (800 µm) and 10.0 ± 1.9 % (600 µm). According to that FFF, also generated channels down to 600 µm diameter, but showed an exponentially increasing deviation of 0.6 ± 0.4 % at 3000 µm to −38.2 ± 6.3 % at 600 µm diameter. In contrast to horizontal channels, the roundness of vertical channels in SLA achieved much lower and stable average deviation of 0.97 ± 0.01 compared to FFF, that roughly showed an exponential tendency of decreasing roundness from 0.96 ± 0.02 (3000 µm) to 0.81 ± 0.05 (600 µm). Printing overhangs without any support structure had very low deviations of 0.0 ± 0.6 % (FFF), −0.5 ± 0.6 % (SLA) and 0.7 ± 1.2 % (SLS) from 90° down to 40° in all three printing methods. Angles below 40° showed exponential increasing deviation, while FFF was not able to print 10° overhangs at all. Therefore, 20° overhangs resulted in 18.6 ± 6.6 % deviation in FFF. In SLA, 10° were produced with 61.0 ± 11.9 % deviation and in SLS 10° deviated by 11.6 ± 15.9 %.

Testing the leakage of 3D printed parts showed low loss of water or none at all by 95.6 ± 0.9 % remaining water after 24 h incubation in cups with 2000 µm down to 400 µm wall thickness in SLA and SLS. 200 µm wall thickness was not printable in SLA, and showed leakage in SLS (4.9 ± 0.6 % remaining water). Although FFF did generate all wall thicknesses from 2000 µm down to 200 µm, only 1 out of 3 samples of 2000 µm and 600 µm wall thickness had no leakage". [67]

The tolerances given by the values above were used to derive a table with the recommended CAD limitations for the FDM/FFF and SLA printing technique (Tab. 12). The results of the SLS printing technique showed insufficient quality for bioreactor printing and have therefore excluded in this table. For FDM/FFF we recommend to design geometries ≥ 500 µm in X- and Y-direction, as well as ≥ 200 µm in height. Same applies for SLA printing, except of a minimal height of 50 µm. Horizontal channels should be designed with a diameter of 1.5 mm smallest, and 1 mm for vertical channels for both printing techniques, as well as overhangs to a minimum of 40°. We also recommend to print vessels with a wall thickness of more than 2 mm with FDM/FFF and more then 500 µm for SLA.

Table 12: Recommended design limitations for 3D-printed geometries

Geometry	**FDM/FFF**	**SLA**
X/Y	≥ 500 µm	≥ 500 µm
Z	≥ 200 µm	≥ 50 µm
Channels horizontal	≥ 1.5 mm	≥ 1.5 mm
Channels vertical	≥ 1 mm	≥ 1 mm
Overhangs	≥ 40°	≥ 40°
Wall thickness	> 2 mm	≥ 500 µm

4.1.3 Testing of 3D-Printed Material Properties after Treatment

After analyzing and determining the printer design limitations, the effect of the sterilization process to the used materials was investigated. To do so, autoclaving was used as it represents the gold standard in biomedical applications. This technique however is also stated to be a rather harsh treatment to the materials. Therefore, vaporized hydrogen peroxide plasma sterilization (VH_2O_2) was used as explained in section 3.6 (p. 41).

According to DIN EN ISO 527 [125] and 178 [126], standardized test bodies were printed for tension tests and four-point-bending tests. These parts were then treated up to three times for each of the sterilization methods and then tested accordingly to their tensile and flexural strength using a spezialized material testing machine Z010 (Zwick Roell AG, GER) (Section 3.7, p. 42). Again, the individual results (Fig. 14) are already published by Gensler and Leikeim *et al.* [67] and repeated here for your convenience:

"FFF-printed parts made from lignin-based Green-TEC Pro filament [...] showed an untreated tensile strength of $44.4 \pm 9.2\,\mathrm{N/mm^2}$ and a flexural strength of $42.7 \pm 3.3\,\mathrm{N/mm^2}$. After performing 3 times plasma sterilisation, no significant difference was detected in both tensile and flexural strength. In contrast, autoclaving significantly reduced tensile ($14.8 \pm 3.6\,\mathrm{N/mm^2}$) and flexural strength ($6.2 \pm 1.1\,\mathrm{N/mm^2}$) after 3 treatments. Flexural strength was already decreased significantly after the first autoclaving treatment. Untreated parts, printed from bisphenol A ethoxylate-based Dental SG Resin (Formlabs Inc., USA) by SLA technique showed a tensile strength of $30.7 \pm 7.9\,\mathrm{N/mm^2}$ and a flexural strength of $27.0 \pm 6.3\,\mathrm{N/mm^2}$. Autoclaving and plasma sterilisation resulted in no significant impact on the material after 3 treatments. Autoclaving however tends to reduce tensile ($14.0 \pm 4.3\,\mathrm{N/mm^2}$ and flexural strengths ($20.4 \pm 2.2\,\mathrm{N/mm^2}$. Untreated SLS printed parts made from Nylon 12 (Sinterit sp. z o.o., Poland) had a tensile strength of $26.5 \pm 0.7\,\mathrm{N/mm^2}$ and a flexural strength of $26.8 \pm 6.2\,\mathrm{N/mm^2}$. After the first treatment of autoclaving and plasma sterilisation, an increase in tensile strength was measured. However, after the second and third treatments in both sterilisation processes no significant differences were measured in the value of the tensile strength in comparison to the untreated control". [67]

In addition to the mechanical properties after sterilization, biocompatibility of the treated materials was investigated as well, aligned to DIN EN ISO 10993-5. According to the results above, 3D-printed parts were defined as single-use whenever they were used for biological experiments. Therefore, the materials for biocompatibility tests were sterilized only once before the cell culture medium was treated with them.

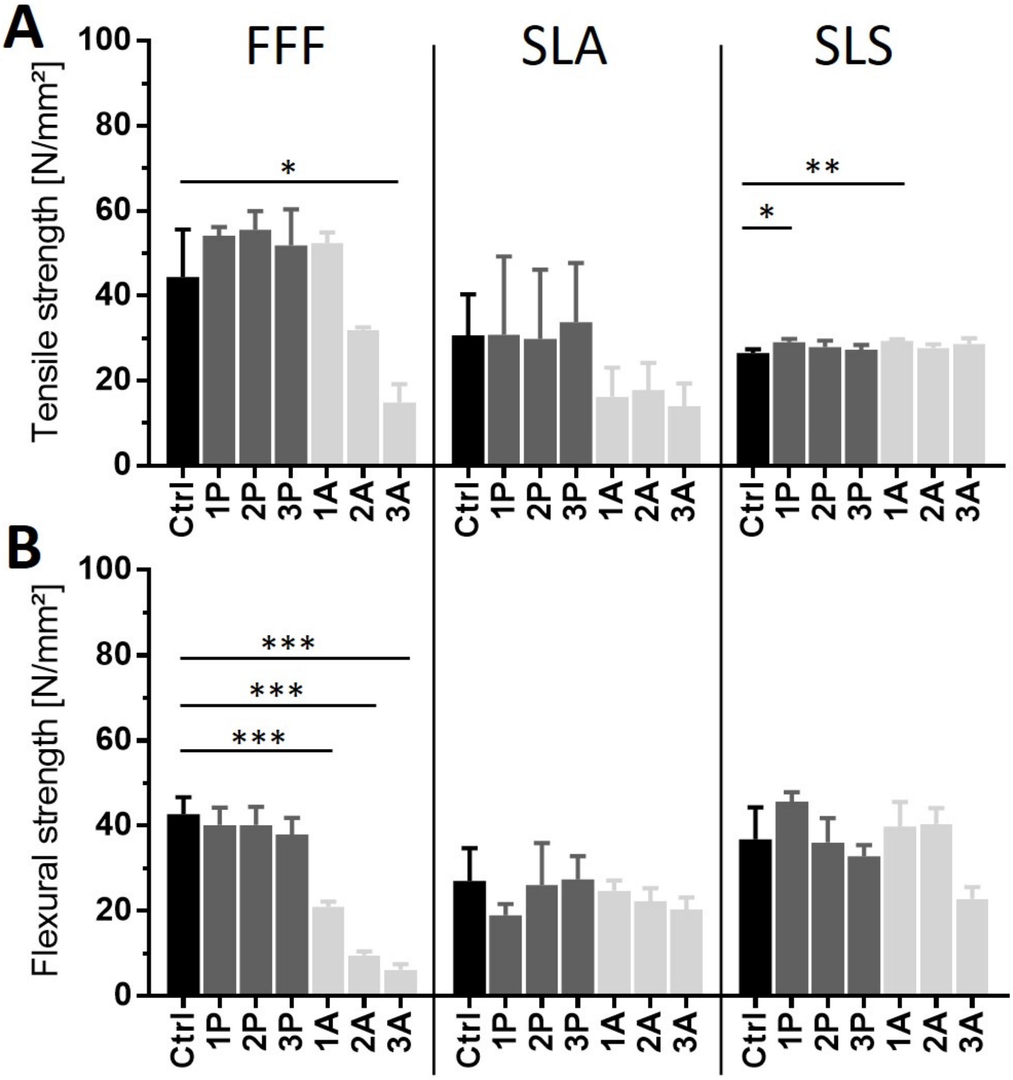

Figure 14: Effect of autoclaving and plasma sterilization to printed materials. Tension **(A)** and bending **(B)** tests were performed according to DIN EN ISO 527 and 178. FFF printed material showed no change in material properties when treated by plasma sterilization up to three times, but autoclaving significantly reduced tensile and flexural strength of the material. In SLA-printed material, no significant loss of tensile and flexural strength could be measured, but autoclaving tends to be more corruptive to the material over time. Materials printed by SLS show a significant increase of the tensile strength when sterilized for the first time, but no further impact when sterilized up to three times. In flexural strength, however, both methods tend to downgrade the material properties but do not show significances. All significances are referring to the control and are indicated by *. n = 3. Figure taken from Gensler and Leikeim *et al.* [67].

As shown in figure 15, materials of the later bioreactor (Lignin and PDMS) were analyzed, as well as materials included in the manufacturing process without direct cell contact to ensure a full biocompatible manufacturing process. As depicted in section 3.8 (p. 42), C2C12 cells were used to perform a passive biocompatibility test according to DIN EN ISO 10993-5 [127]. As stated in this norm, materials are defined as biocompatible if the viability shows $\geq 70\,\%$ compared to the positive control, which is defined to 100 %. Materials used for the actual bioreactor were incubated at 37 °C to simulate the cell culture atmosphere.

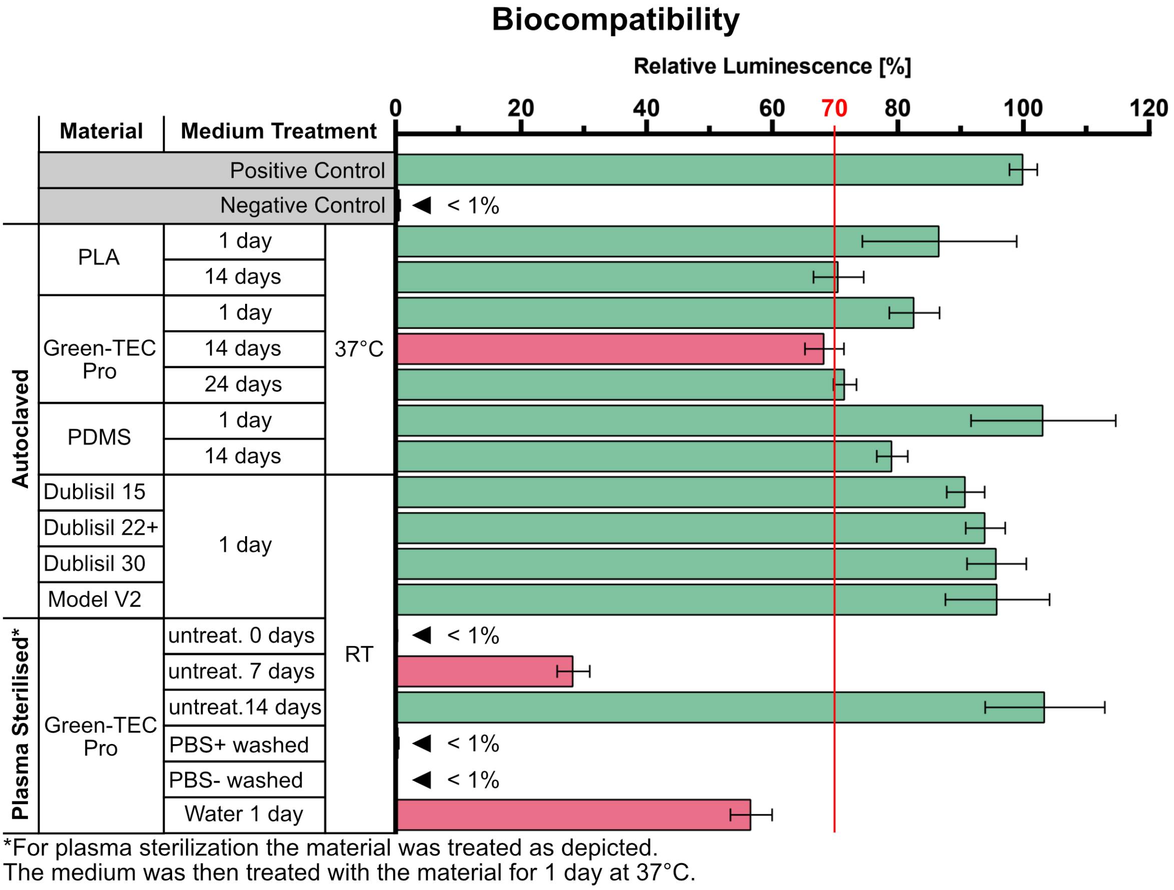

Figure 15: Biocompatibility of tested materials. CellTiter Glow assay of material-treated cell culture medium was quantified by luminescence measurement. Untreated medium (positive control) was defined to 100 %. According to DIN EN ISO 10993-5, 70 % marks the transition from biocompatible to non-biocompatible material. Therefore, materials with a mean $\geq 70\,\%$ are depicted in green and materials $< 70\,\%$ are shown in red.

Polylactic acid (PLA) was tested also due to its gold standard in conventional 3D printing. PLA showed a positive biocompatibility after 1 day of medium incubation by $86.7 \pm 12.3\,\%$. After 14 days of incubation biocompatibility was reduced closely the the 70 %-threshold to $70.6 \pm 4.0\,\%$. Likewise, lignin showed a positive biocompatibility at day 1 ($82.6 \pm 4.0\,\%$) and a reduced one at day 14 just under 70 % (68.3 ± 3.1 %). Lignin was then also tested for 24 days to investigate long time behavior. Here, biocompatibility increased slightly over 70 % to 71.6 ± 1.9 %. PDMS was biocompatible positive at first day (103.2 ± 11.5 %), as well as day 14 (79.1 ± 2.5 %), even though the biocompatibility also decreased here as well at day 14. Next, the materials used for PDMS casting and the manufacturing process were tested. To do so, different kinds of Dublisil® silicons (15, 22+, 30), as well as resin Model V2 were incubated with the medium for one day. All of them showed positive biocompatibility by 90.8 ± 3.0 % for Dublisil® 15, 93.9 ± 3.2 % for Dublisil® 22+, 95.8 ± 4.8 % for Dublisil® 30 and 95.9 ± 8.3 % for the resin Model V2. All tested materials so far were sterilized by autoclaving before treated to the medium. Since some parts of the bioprinting process (like some connectors) could not been sterilized, vaporized hydrogen peroxide plasma sterilization was used. For this tests, lignin was used as testing material. The sterilized parts were treated as described in figure 15 before the incubation with medium for one day. It was shown, that plasma sterilized parts were not biocompatible at all if applied to the medium before 14 days after sterilization (103.4 ± 9.6 %). If the parts were incubated with the medium directly after sterilization the biocompatibility was at 0.30 ± 0.04 % and at 28.3 ± 2.6 % when incubated 7 days after sterilization. Washing the parts after sterilization with PBS^+ or PBS^- prior to medium incubation did not had an effect to the biocompatibility (0.50 ± 0.05 % and 0.20 ± 0.02 %). Incubating the parts in ultra pure water (Millipore) for 1 day before incubation with the medium showed a biocompatibility of 56.7 ± 3.3 %.

4.1.4 Guideline for 3D Printing in Tissue Engineering

With the results gathered about the 3D printers, as well as the material properties and the biocompatibility, a guideline was formed for standardized accessing of 3D printing for tissue engineering (Fig. 16). This guideline is also already published by Gensler and Leikeim *et al.* [67]. The description of the guideline is repeated here for your convenience:
"[...] the individual printer-software is used to transfer the STL-file into G-code. Within this step, it is crucial to set the printer settings suitable to the desired needs and material. Afterwards the parts are printed. The test bodies are designed in a way that the region of interest can easily be imaged using a microscope. Images are then loaded into Fiji and the area of interest is cropped manually. After that, the Fiji macros [...] are executed to quantify the accuracy of the printed parameters. Additionally, the bodies for mechanical tests can be sterilised before investigating properties of different materials and the effect of individual sterilisation methods.

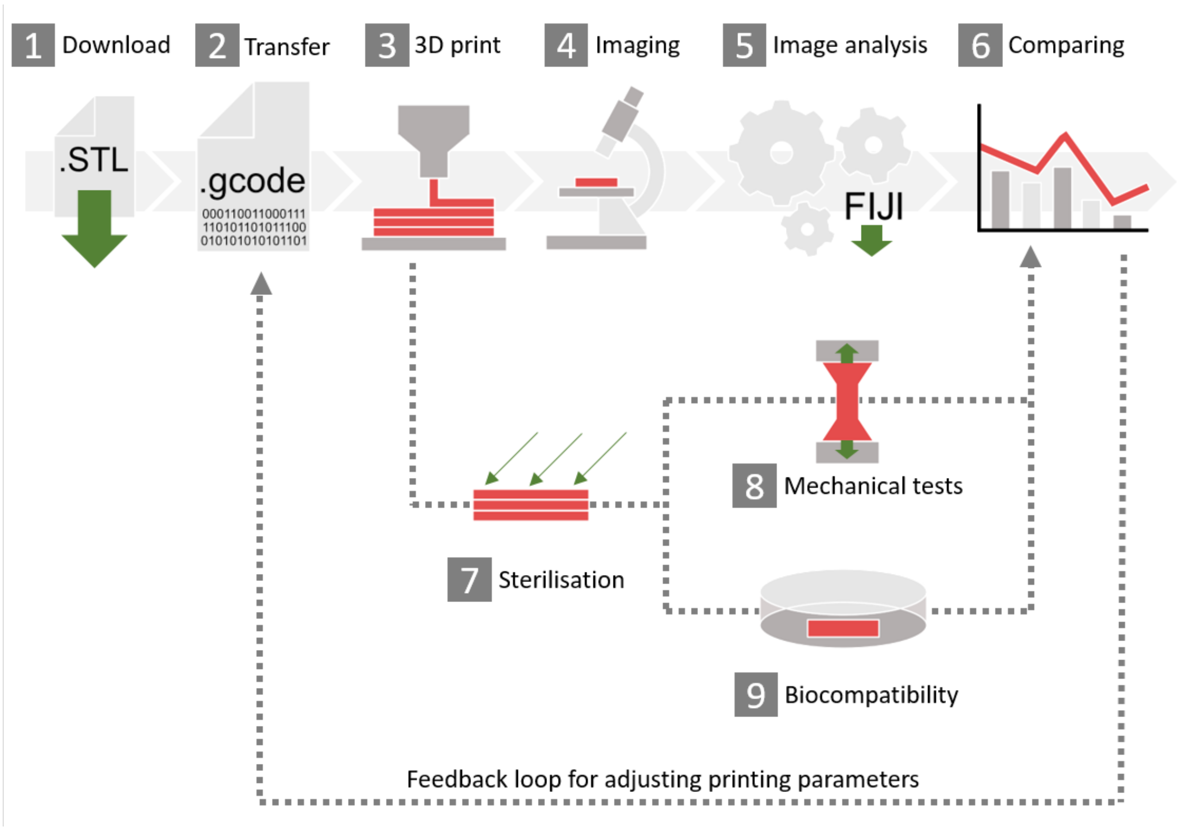

Figure 16: Overview of the 3D printing guideline. (1) Download of the STL-files of the test bodies (attached to the publication [67]). **(2)** Transfer of the STL-files into Gcode or similar, using the individual software and printer settings. **(3)** 3D printing of the test bodies. **(4)** Imaging of the printed parts. **(5)** Download the ImageJ macros (attached to the publication [67]) and analyze the images after cropping the area of interest. **(6)** Compare the results to each other or to different printers whether they match the desired quality or not. After printing, the sterilization test **(7)**, mechanical test (DIN EN ISO 527 and 178) **(8)** or biocompatibility tests (DIN EN ISO 10993–5) **(9)** can be performed. Figure taken from Gensler and Leikeim *et al.* [67].

For TE approaches the biocompatibility of the bioreactor test body after sterilisation has to be investigated. At last, different printers, materials, printing techniques and printing parameters can be compared and the obtained results can be used to adjust printing parameters for better printing results". [67]

4.1.5 Analysis of Independent FDM/FFF Printers

The guidance was then sent out to different labs, so they could use it on their FDM/FFF printer and investigate the optimal printing parameters. The 3D printers used for this interlaboratory test were Ultimaker 3 and Ultimaker S5 (both Ultimaker B.V., NL) and the printing settings used are stated in figure 11. The individual results (Fig. 17) are already stated in Gensler and Leikeim *et al.* [67] and repeated here for your convenience:
"In this case, Raise3D Pro 2 (RP2) (RAISE3D Technologies, USA), Ultimaker 3 (UM3) and Ultimaker 5S (UM5) (Ultimaker B.V., Netherlands) were compared. Data of the RP2 printer was already used as a FFF reference before [...]. RP2 achieved a stable deviation of 6.5 ± 7.4 % down to 500 µm when analysing X and Y resolution followed by an exponential increase of inaccuracy of 185.1 ± 28.9 % at 200 µm lowest possible dimension. UM3 and UM5 did not print dimensions smaller than 400 µm and showed exponentially increasing inaccuracy from 28.4 ± 7.3 % at 1000 µm to 100.5 ± 16.5 % at 400 µm. In contrast, accuracy deviation in height was low in UM3 and UM5 down to 200 µm (16.7 ± 5.5 %), followed by deviating 635.7 ± 14.0 % from 20 µm height in UM3. UM5 did stop printing heights below 60 µm (147.8 ± 21.5 %) and RP2 below 100 µm (185.3 ± 9.3 %). As shown before, RP2 had oscillating deviation in horizontal printed channels. UM3 and UM5 both result in a smaller diameter than designed initially. The printing limit of all printers was 400 µm diameter channels. Roundness was decreasing more in RP2 (0.63 ± 0.06) and UM5 (0.63 ± 0.08) compared to UM3 (0.85 ± 0.09) at 400 µm. Loss of quality also showed an exponential tendency here. In printing vertical channels, the ultimaker printers achieved significantly different capabilities than RP2. Deviation was already at −22.8 ± 2.8 % at 3000 µm diameter and it further decreased to −69.0 ± 7.5 % at 1500 µm diameter which was also the lowest diameter printable. According to that, roundness also decreased rapidly from 0.90 ± 0.06 (3000 µm) to 0.58 ± 0.11 (1500 µm). By printing overhangs, all printers showed a 0.4 ± 1.0 % deviation down to 40°, following by exponential increase to 43.0 ± 3.4 % (UM5) and 46.4 ± 2.8 % (UM3) at 10° and 18.6 ± 7.5 % (RP2) at 20°. In contrast to RP2, UM3 and UM5 did not show any leakage in all wall thicknesses with an average amount of remaining water of 97.2 ± 0.8 % for both printers. The wall thickness of 200 µm was only printable with the RP2 printer. These results show a successful application of our established guidance in the described interlaboratory tests and thereby confirmed its robustness and reproducibility." [67]
The bioprinting technique used here is derived from, and therefore closely related to, the FDM/FFF technique. Due to this, we decided to go for FDM/FFF printing techniques for the further bioreactor development.

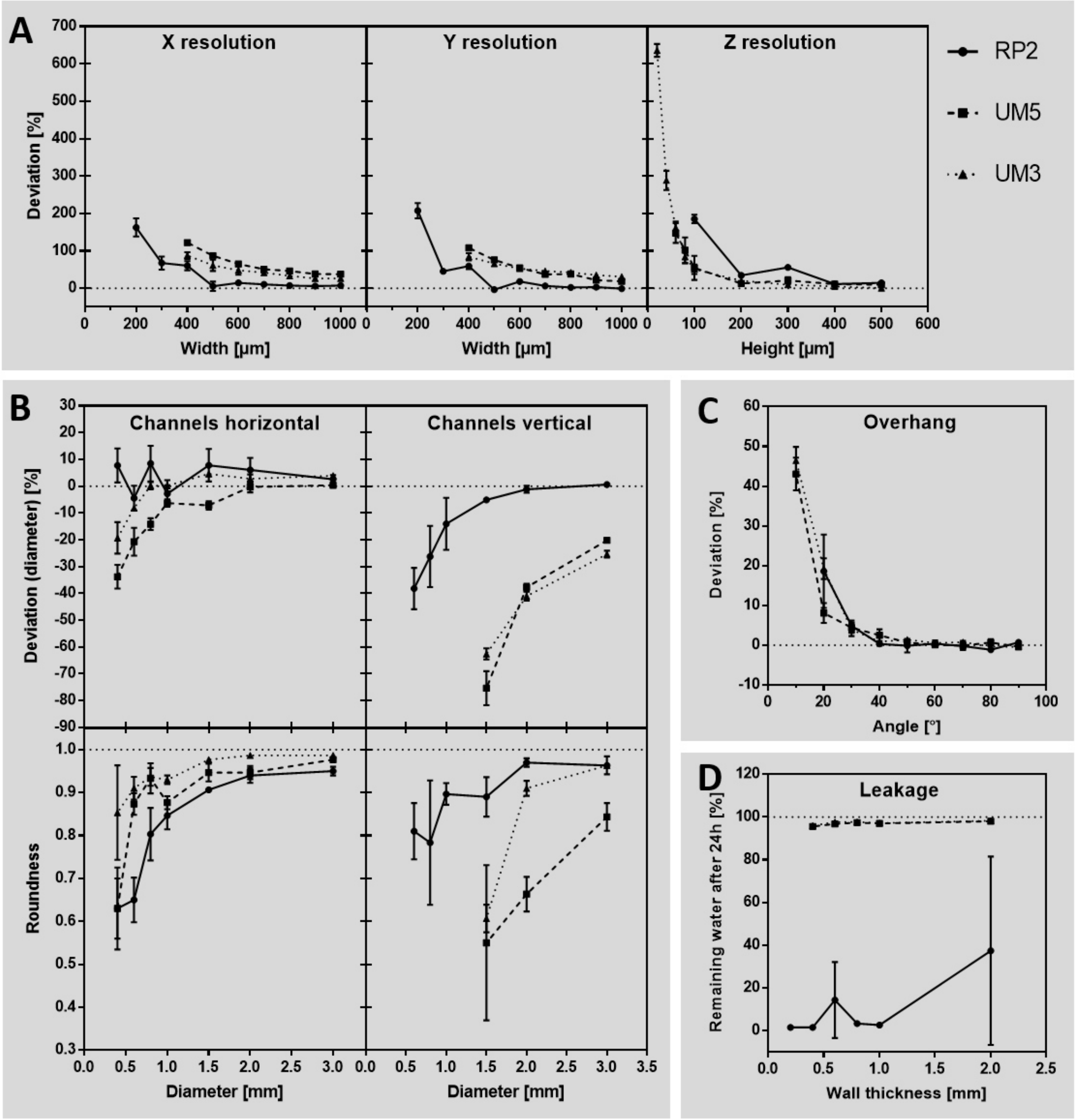

Figure 17: Accuracy of different FFF printers compared to each other. Test bodies, which were FFF-printed with Raise3D Pro 2 (RP2), Ultimaker 3 (UM3) and Ultimaker S5 printer (UM5) were analyzed regarding their deviation of the respective geometry that was designed by CAD before. Data from Raise3D Pro 2 are equal to figure 13 (FFF). **(A)** Accuracy of the base axes X, Y and Z. **(B)** Diameter and roundness of horizontal and vertical printed channels. **(C)** Angled overhangs, printed without support structures. **(D)** Leakage investigated for different wall thicknesses. n = 3. Figure taken from Gensler and Leikeim *et al.* [67].

4.2 Development of the Bioreactor Platform

4.2.1 Developmental Aspects

After accessing general design criteria and printing strategies for a FDM-printed bioreactor, the actual design of a bioprinting-suited bioreactor platform was focused. Therefore, the strategy of a step-by-step elimination of design short-comings and issues was used for the distinct generations and iterations. With the first iterations G.01 to G.03 (Fig. 18), a simplified geometry was designed for perfusing a tissue construct.

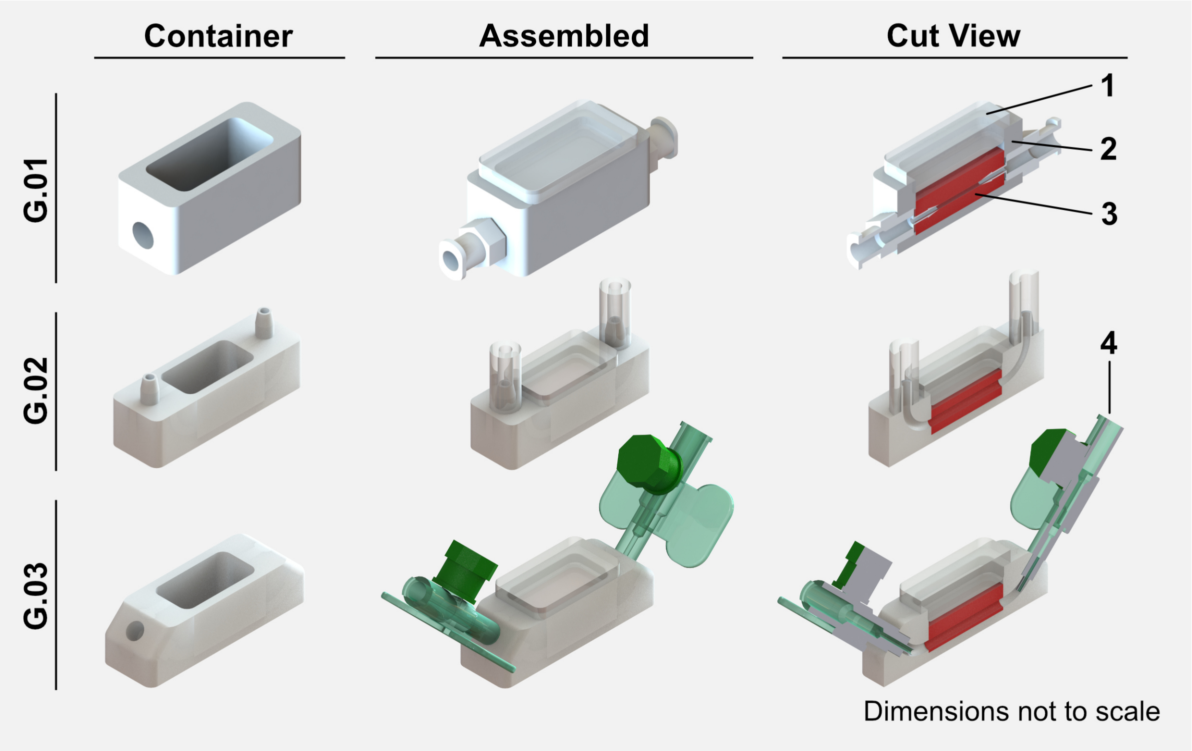

Figure 18: Iterations G.01 to G.03 of the bioreactor development. This first iterations focused on a simple 3D-printable design to investigate basic requirements for a 3D-printable bioreactor. Sealed by a lid made from PDMS (1), the 3D-printed tissue container (2) holds the tissue construct (3). Medium flow is applied via indwelling cannulas (4). The tissue construct was not bioprinted, but casted at this stages of development.

A PDMS-casted lid (1) was used to seal a simple 3D-printed container made from lignin (2), holding a perfusable construct (3). All three generations showed leakage during 14 days of dynamic culture and an unstable channel, but also showed a suitable demand of time and material.

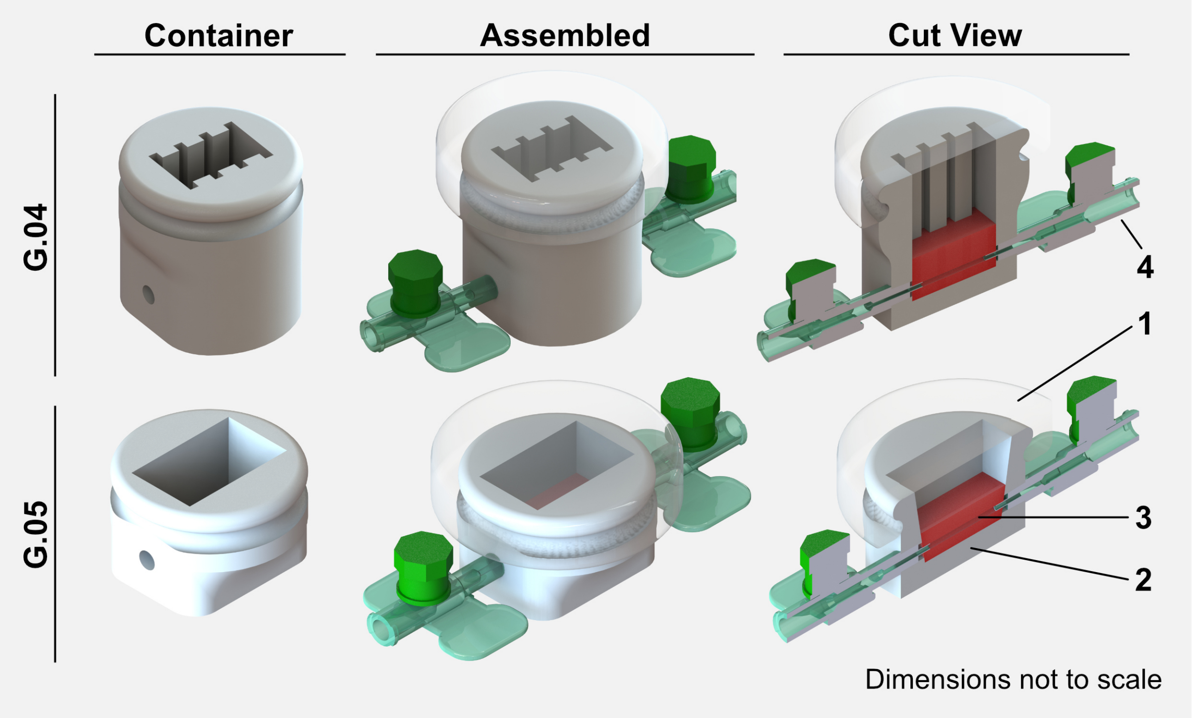

Figure 19: Iterations G.04 and G.05 of the bioreactor development. With this iterations leakage issues were addressed as well as bioprinter accessibility. The 3D-printed container (2) was increased in complexity and the lid made from PDMS (1) was reshaped for better sealing. The tissue construct (3) is perfused using indwelling cannulas (4).

Even though, a construct could be bioprinted into them, perfusion experiments were done by casting the bioink into the containers. G.01 and G.03 needed a higher amount of parts compared to G.02 but therefore the 3D printed part was not printable with sufficient quality here. The problem with detaching constructs during perfusion was solved first with G.03 by using indwelling cannulas as connectors (4).

With generation G.04 (Fig. 19) the leakage-issue was solved for the first time by increasing the overall container height and improving the PDMS-lid. Unfortunately this way the geometry of the container needed a much greater amount of material and printing time. Additionally, the container was to high to print a construct inside. This, on the other hand, was solved with G.05 by reducing the height of the container, as well as implementing angled interior walls for bioprinting with conical nozzles. The reduction of height however led again to leakage during perfusion.

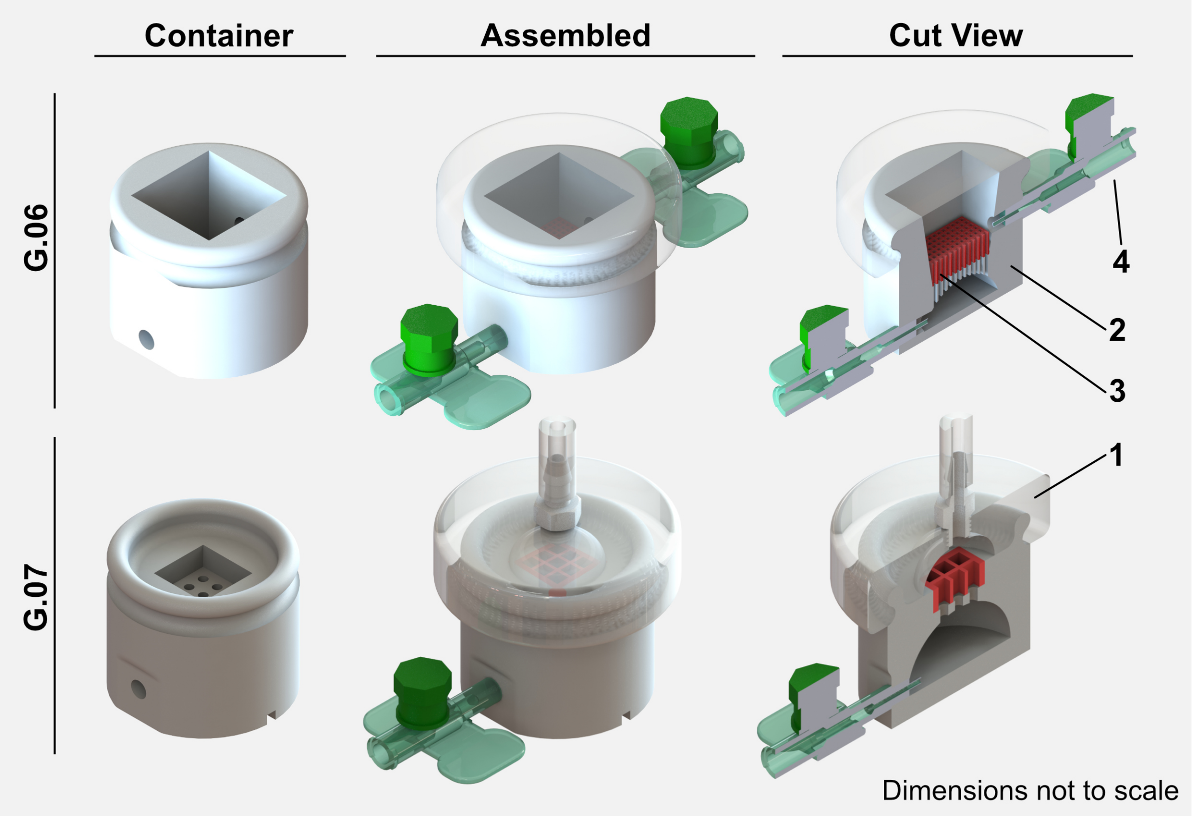

Figure 20: Iterations G.06 and G.07 of the bioreactor development. With this iterations the concept of perfusing the tissue was switched. The 3D-printed tissue container (2) was redesigned for a lower and a upper compartment in order to perfuse the tissue construct (3) vertically. The lid made from PDMS (1) was redesigned as a medium outlet. With this, one of the indwelling cannulas (4) could be removed, leading to enhanced leakage-proof.

Within iteration step G.06 and G.07 (Fig. 20) there was an important major switch in the bioreactor concept in order to improve channel stability and overall bioreactor performance: The perfusion of the construct was switched from horizontal to vertical perfusion, which led to a two-compartment-container with vertical pores connecting these compartments. This counteracted the instability of the channels, as they could no longer collapse. In addition, the density of parallel channels was significantly increased. Medium inflow was applied via the lower, half-spherical, compartment. Compared to G.06, in G.07 the size of the pores and the lower compartment were increased, leading to a better printing quality. Also the upper indwelling cannula was removed and a LUER-connector was installed to the lid to reduce leakage. Even though G.07 showed less leakage, both iterations did not overcome this issue completely.

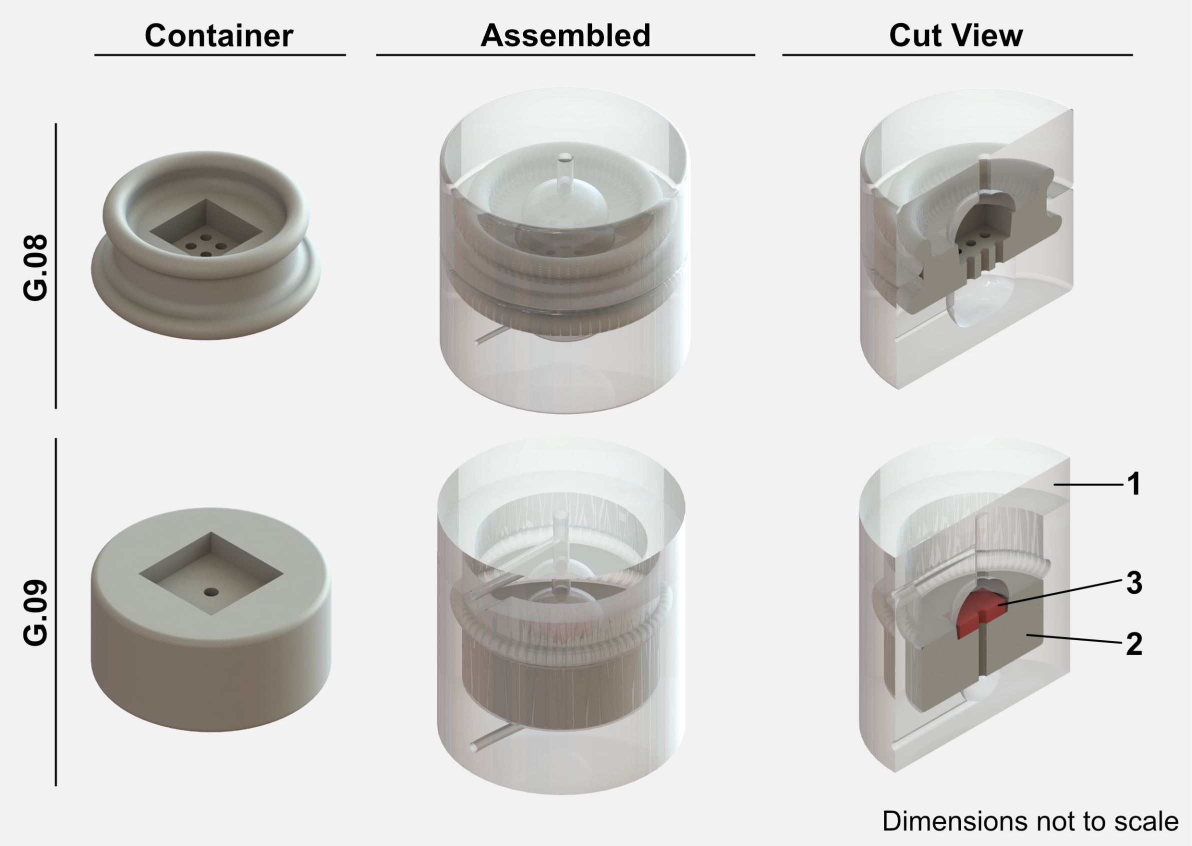

Figure 21: Iterations G.08 and G.09 of the bioreactor development. With this iterations the leakage issue could be solved finally by full encapsulation of the 3D-printed container (2) with a housing and a lid made from PDMS (1). The container, holding the tissue construct (3), could also be reduced in size and complexity leading to an improved printing time.

Using the insights from G.07, the sealing performance was increased by full encapsulation of the 3D-printed container with parts made from PDMS (Fig. 21). Additionally, the container-part could be reduced in complexity dramatically, resulting in lower printing time and demand on material compared to the previous generations. Different from G.08, in G.09 the PDMS-parts are intersectioning each other. This way the leakage was overcome by sealing a PDMS-PDMS-interface, rather then sealing a PDMS-Lignin-interface.

An overview of the major short-comings are summarized in table 13. As an indicator for the chances for contamination and leakage, the amount of needed parts, between inflow and outflow connectors, was listed (Parts). Also included are whether the construct is perfusable in the bioreactor generation or not (Perfusability). Next, the FDM-printed quality of the parts was rated to be sufficient or not (Printable).

Table 13: Eliminated short-comings and issues of bioreactor generations

	G.01	G.02	G.03	G.04	G.05	G.06	G.07	G.08	G.09
Parts	5	2	6	6	6	6	5	5	5
Perfusability	X	X	X	X	X	X	X	X	X
Printable	X		X	X	X	X	X	X	X
Accessibility	X	X	X		X	X	X	X	X
Connection			X	X	X	X	X	X	X
Time/Material	X	X	X					X	X
Stability						X	X	X	X
Leakage-proof				X					X

Also, the possibility to bioprint a construct inside the container (Accessibility) was noted, as well as the disconnection of the construct from the inflow and outflow connectors inside the bioreactor during perfusion (Connection), closely related to the stability of the channel inside the construct (Stability). Finally, the subjective rated demand of needed time and material for printing and whether this was an acceptable amount or not (Time/Material) is listed, together with the overall leakage of the whole bioreactor system during 14 days of perfusion (Leakage-proof).

4.2.2 Final Bioreactor Platform

Derived from the G.09 concept, the final bioreactor platform G.10 was designed and optimized (Fig. 22 + 23). As shown in figure 22, the simplified tissue container (1), holding the bioprinted construct (2) is inserted into the bioreactor housing made from PDMS (3). This housing shows two compartments next to each other: The tissue compartment holding the tissue container, and the medium reservoir holding the medium of the setup. The housing is then closed with an optimized lid geometry, sealing the bioreactor similar to G.09.

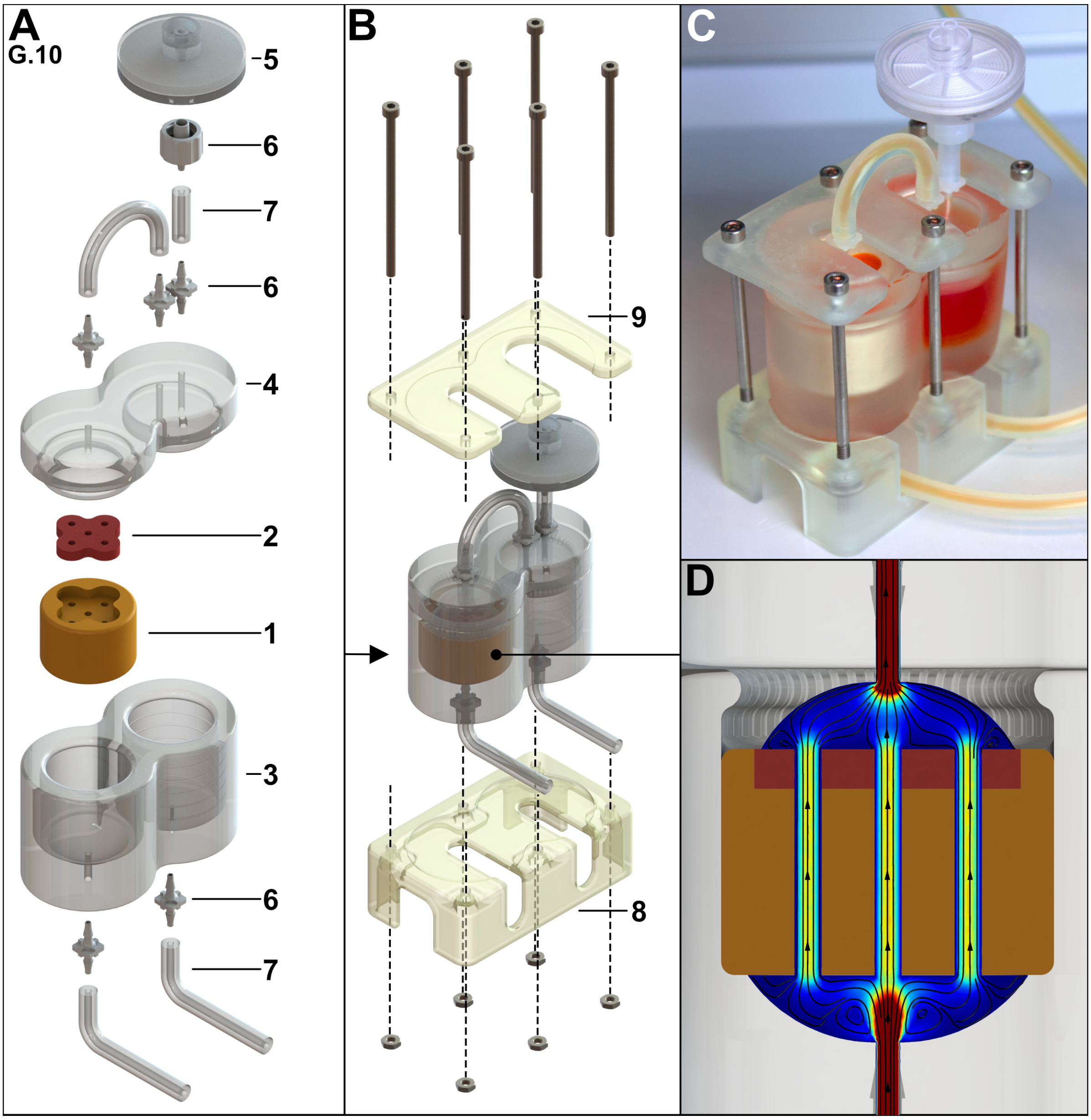

Figure 22: 3D-printed bioreactor setup. (A) Exploded view of the bioreactor parts: A preprinted tissue container (1) holding the bioprinted tissue (2) is inserted into the bioreactor housing (3) made from PDMS. The housing mainly forms two compartments like the tissue chamber and the medium reservoir. A lid (4) made from PDMS closes the bioreactor tightly. Silicon hoses (7), as well as a sterile air-filter (5), are connected to the bioreactor via LUER-connectors (6). **(B)** Fixation parts (8 + 9) enable a stable stand of the bioreactor. **(C)** Photo of the assembled bioreactor. **(D)** *In silico* analysis visualizes the applied medium flow within the tissue chamber from high velocity (red) to low velocity (blue). Streamlines and arrows indicate the flow direction.

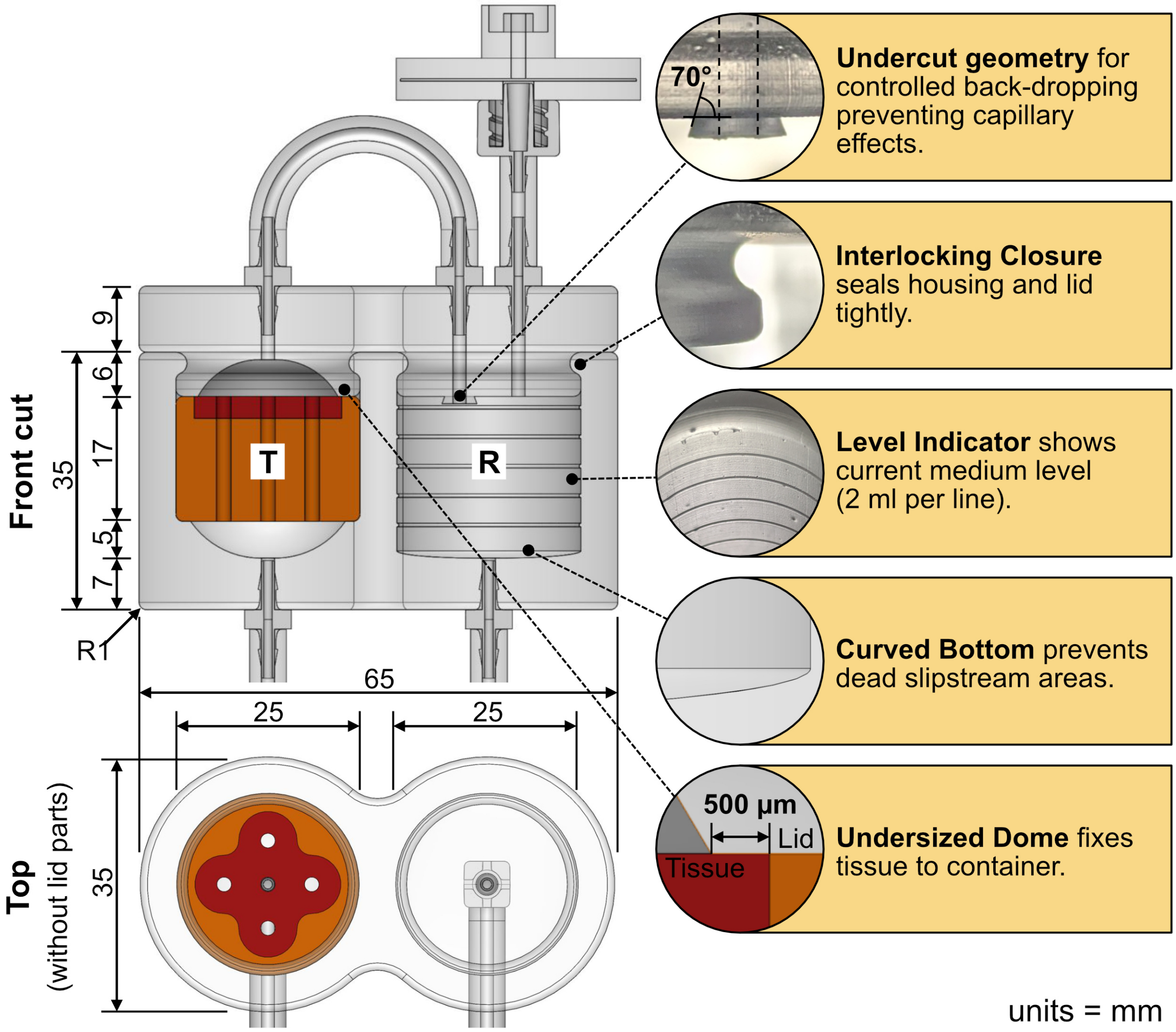

Figure 23: Sectional views of the bioreactor interior. Sectional view showing the tissue chamber (T) and the medium reservoir (R). Designed details of the bioreactor setup include an undercut geometry for controlled back-dropping of the medium, an interlocking geometry of the lid and the housing, level indicators inside the medium reservoir, a curved bottom of the medium reservoir for preventing dead slipstream areas and an undersized dome shape to fix the tissue construct in the container.

On top of the lid a sterile air filter (5) is connected via LUER-connectors (6) and silicone hoses (7). Also, the tissue compartment is connected to the medium reservoir on top of the lid. Both compartments are connected at their bottom to the pumpcycle. To further reduce the likelihood for leakage, the lid and the housing are tightly compressed between a SLA-printed bioreactor stand (8) and a likewise printed plate on top of the bioreactor (9) as depicted in figure 22 B. The concept of the medium flow direction is shown (Fig. 22 D) with the medium being pumped into the tissue compartment from below and through the pores of the container, as well as the aligned pores of the tissue. After exiting the tissue, the medium is flowing back to the medium compartment via a silicone hose on top of the bioreactor. As shown in the technical schematic of the bioreactor (Fig. 23), some minor improvements were done to the system that are crucial for proper function and handling of the platform. First, an undercut geometry was added to the backflow of the medium into the medium reservoir. This undercut counteracts the capillary effect of the medium and prevents it from interflowing the Lid-Housing-interface. With this geometry a controlled dropping of the medium is ensured. Next, the interlocking geometry of the lid and the housing from G.09 was further improved and applied to the system. Additionally, level indicators were designed for the medium reservoir to get a visual feedback of the filled medium. The bottom of the medium reservoir is curved and forms a funnel-like structure to prevent dead slipstream areas and enables the complete draining of the reservoir. An important aspect is the undersized dome geometry of the lid, which fixes the tissue in place during perfusion.

4.3 Bioprinting Process

4.3.1 Analysis of different Shapes for Tissue Construct

After defining the final geometry of the tissue container, the degree of freedom of the 3D printing technique was used to test different construct shapes. Limited by the outer shape of the tissue container, different shapes were designed and analyzed for their bioprinting potential. The designed tissues are depicted in Figure 24 and include a squared shape with the edge length of 11.6 mm and one central channel (Square1), as well as one with four channels (Square4). Complimentary to that, a flower shape was designed with a diameter of 13.4 mm and one central channel (Flower1), as well as five channels (Flower5). Additional to that, an iconic heart-like shape (Heart), as well as a smiley was designed (Smiley). All of those shapes had a height of 3 mm and were printed out of 5 layers. Last, a column structure was designed with a diameter of 8 mm and a height of 12 mm (Column). The pores were designed having a 2 mm diameter, while the column shape had a diameter of 2.8 mm. For all of those shapes a tissue container was adapted accordingly and a Gcode was written, as described in section 3.2.1 (p. 3.2.1), to test the printability of the shapes.

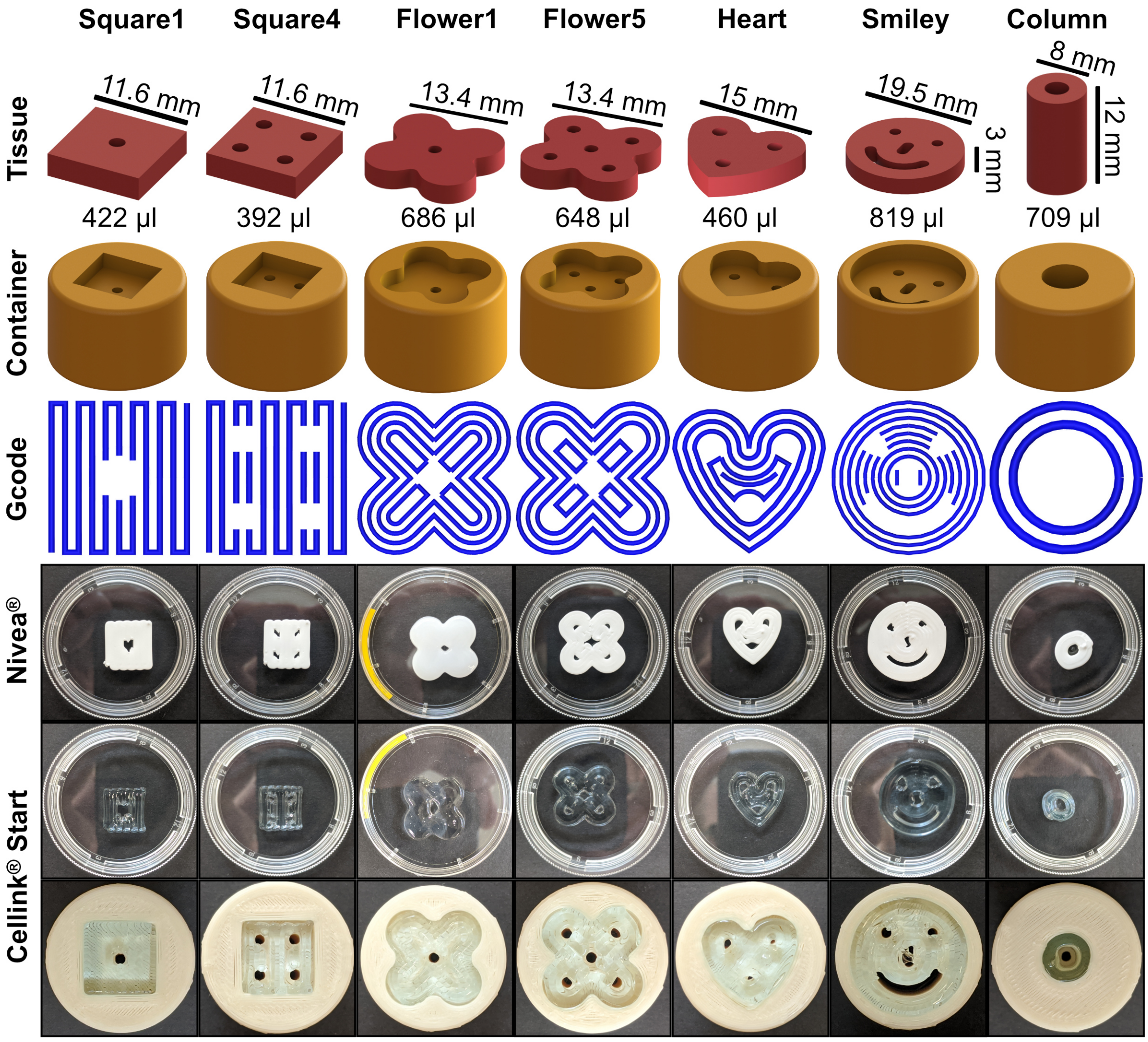

Figure 24: Proof of concept by testing different geometries from tissue design to final printing assessment. First row shows the CAD of different tissue geometries including different pore arrangements and the overall tissue volume. Second row shows the CAD of the derived tissue container. One layer of the tissue Gcode is graphically depicted in the third row. Within the forth row first printing tests with NIVEA® lotion are depicted. The lower two rows show the bioprinting assessment using the Cellink® Start hydrogel for printing the constructs in a petri dish, as well as into the preprinted tissue container.

In a first attempt, NIVEA® lotion (Beiersdorf AG, GER) was used to roughly test the Gcode and printer setting by printing the shapes into a petri dish. After that, Cellink® Start (Cellink AB, SWE) was used for fine-tuning the Gcode and the printer settings. After final adjustments, bioprinting into the preprinted tissue containers was tested using the Cellink® Start hydrogel. All of the shapes could be printed with the same Gcode parameters and printer settings. An one-layer-example of the Flower5 Gcode is depicted in Code 3 (p. 120). The Gcodes were designed with a strand distance of 1 mm. The height of the first layer was set to 0.4 mm and the distance between the layers to 0.6 mm. Printing speed was set to 600 mm/min. A blunt nozzle with 0.41 mm inner diameter and a length of 6.35 mm was used to print all shapes except of the column one. To print the column shape, a nozzle with a length of 12.7 mm was used. The column shape was printed at a pressure of 230 - 250 kPa and 104 - 120 kPa were used to print the other shapes.

Before starting perfusion experiments with cells and bioink, the individual shapes were examined for their performance in dynamic culture conditions. To do so, *in-silico*-simulation was performed using COMSOL multiphysics software as described in section 3.9.1 (p. 43). As shown in figure 25, the velocity of the medium flow was simulated to investigate whether the pores are distributed equally with medium or not. As initial value, a mass volume of the pump of 1.5 ml/min was used causing a maximum flow velocity inside the tissue pores of 5.2 mm/s. If applied to a shape with multiple pores, the velocity drops accordingly in the individual pores. As it is shown, the medium velocity is equally distributed throughout the individual pores of each shape, with exception of the smiley-shaped geometry. Here the pores show an unequal medium distribution. Derived from the medium velocity, the shear stress was also calculated and depicted in figure 25. Since the shear stress is calculated by the flow velocity, the depicted results correlate to the medium flow velocity. In shapes with one single pore, the sheer stress did reach to a maximum of 30 MPa and showed correlating lower stress in shapes with multiple channels. Also the shear stress was equally distributed in the individual channels except of the Smiley.

Most important, the glucose concentration during dynamic culture was simulated as well. The initial values, as well as glucose consumption and diffusion coefficient were calculated and derived from literature and are listed in detail in section 3.9.1 (p. 43). The concentration of the glucose in the steady state analysis were between 12 mol/m^3 and 25 mol/m^3 (initial value of the medium). It can bee seen, that the squared and flower shapes with more then one channel have a higher glucose concentration in the overall tissue compared to the other shapes. Also, in these shapes the concentration is equally distributed, while the Square1, Flower1, Heart, Smiley and Column show areas with lower glucose concentration.

According to the results gained by *in-silico*-simulation, Flower1, Flower5 and Column were used for test-printing with bioink. As described in section 3.2.2 (p. 37) and section 3.2.3 (p. 38), Alginate-POx bioink and Cellink® Bioink were printed into the according tissue containers. For this experiments no cells were mixed into the bioinks.

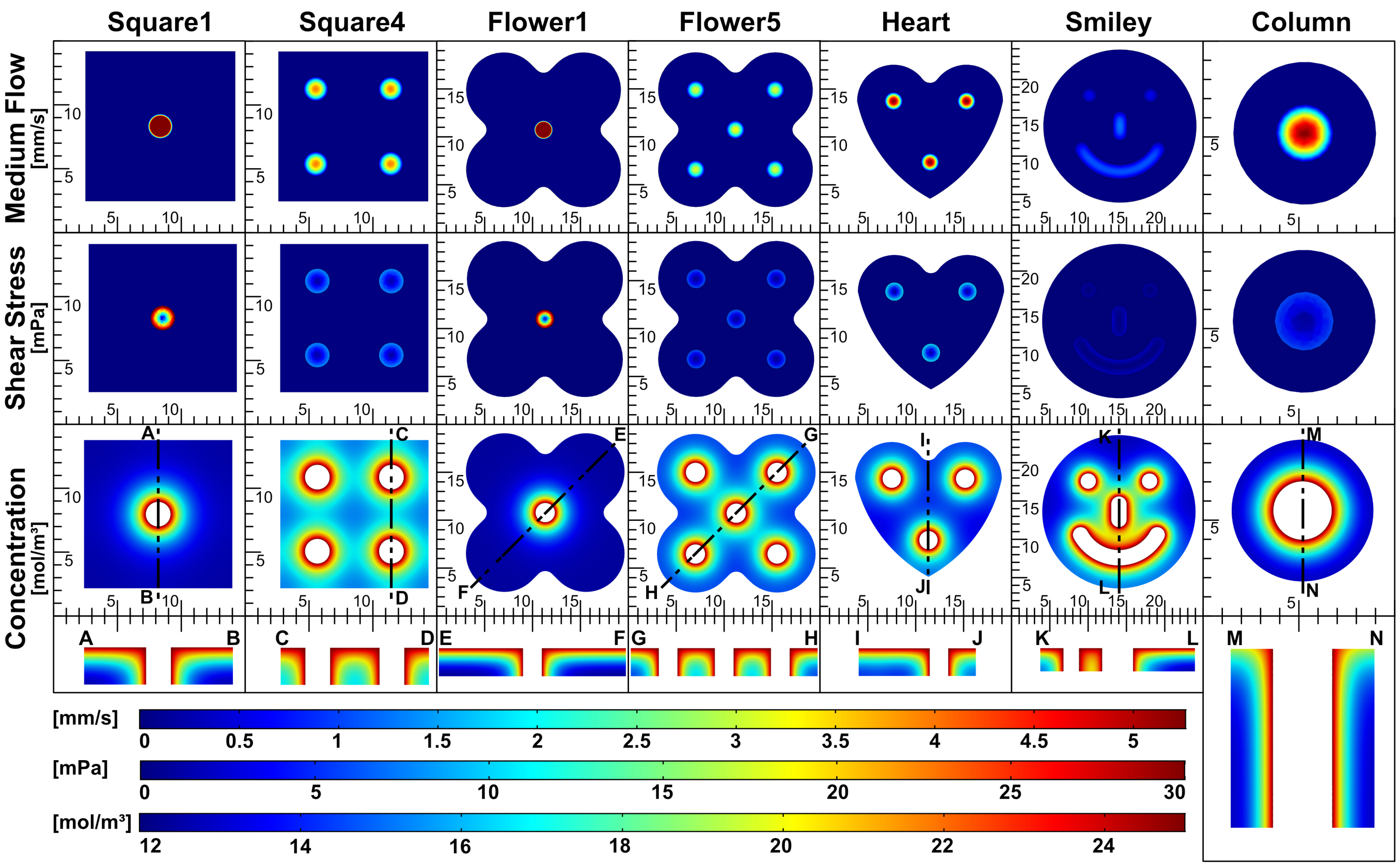

Figure 25: Steady state conditioned *in-silico*-simulation of relevant parameters. Each of the tissue geometries are assessed for the medium flow distribution of the pores (upper row), the shear stress within the pores (middle row) and the concentration of glucose in the tissues (lower two rows). 1.5 ml/min was used as initial medium flow and the calculation of the shear stress. Start concentration of the tissue is 0 mol/m^3 and 25 mol/m^3 for the medium. The diffusion coefficient was set to 6×10^{-10} m^2/s [130] and the elimination rate was calculated to -1.157×10^{-4} mol/m^3 s (glucose consumption of 3 mio cells/ml) [131]. Glucose concentration is also shown as cut view indicated by A-B, C-D, and so on.

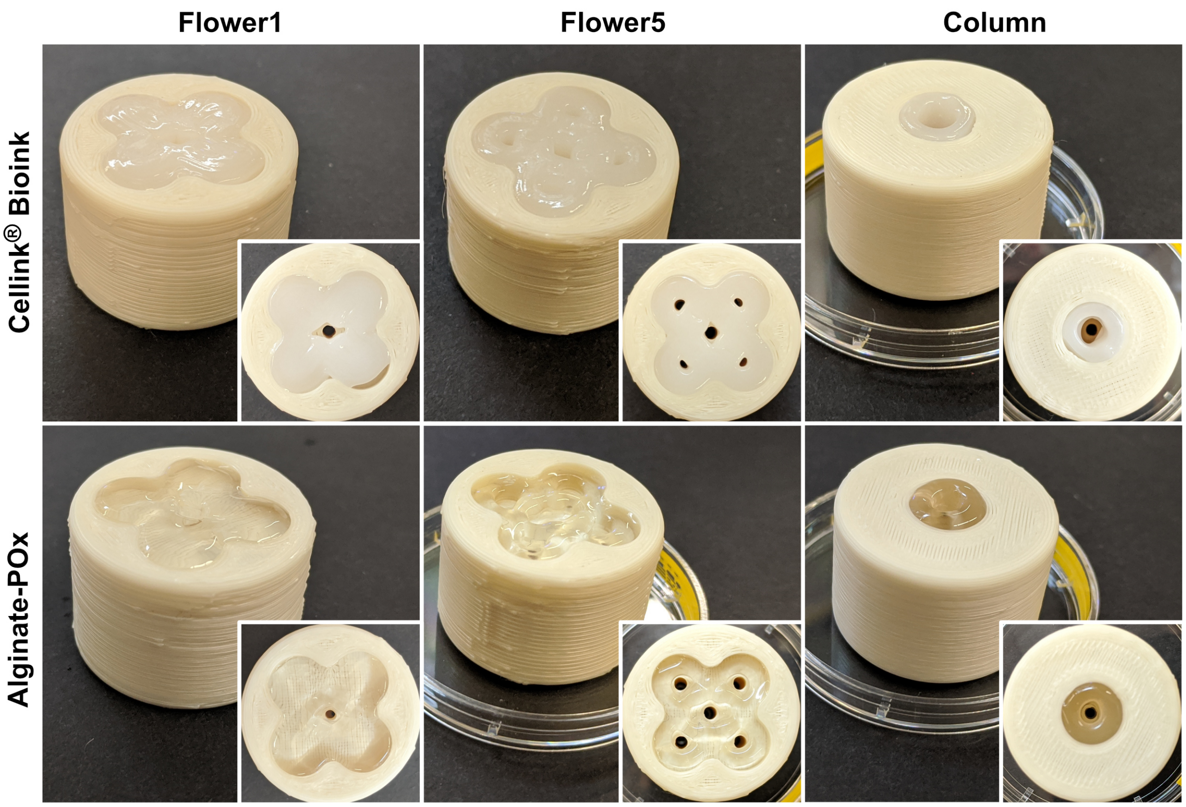

Figure 26: Printed constructs by bioink without cells. Cellink® Bioink and Alginate-POx bioink constructs with Flower1, Flower5 and Column shape.

As shown in figure 26, all three shapes could be printed into the tissue containers with high quality. The pores of the constructs are aligning with the pores of the tissue container the same way as the printed constructs made from Cellink® Start (Fig. 24). Crosslinking was achieved by applying calcium chloride containing crosslinking solution (Cellink AB, SWE) on top of the printed constructs for 30 min (Fig. 27).

4.3.2 Dynamic Perfusion cultured Constructs

After proper investigation and test-printing of bioink constructs into the tissue container, cell-containing perfusion experiments were conducted. Therefore, Alginate-POx bioink and Cellink® Bioink were mixed with 10 mio C2C12 cells/ml, as described in section 3.2.2 (p. 37), and printed using the Flower5-shape into the respective tissue container (Section 3.2.3, p. 38). C2C12 cellline was used at this stage since it shows a fast growing and inexpensive cell source. After printing and crosslinking of the tissue constructs, they were dynamically

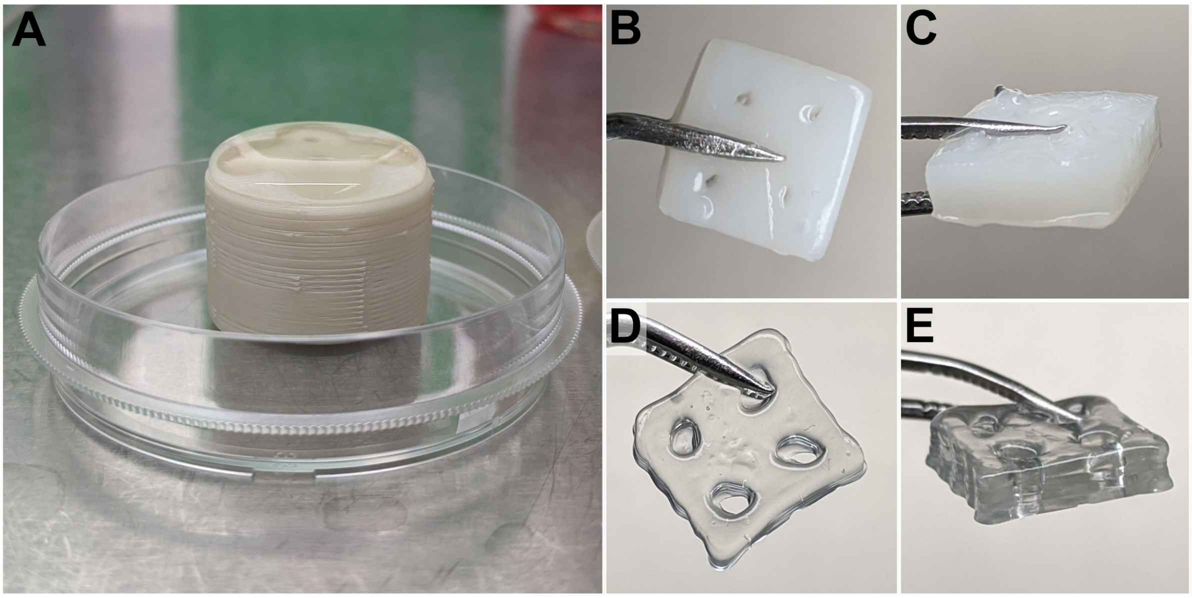

Figure 27: Crosslinking of bioprinted constructs. (A) Cellink® crosslinking agent applied for 30 min to a bioprinted construct printed into tissue container. **(B+C)** Crosslinked construct made from Cellink® Bioink. **(D+E)** Crosslinked construct made from Alginate-POx bioink.

cultured for 14 days, as explained in section 3.9.3 (p. 45). Because bioprinted constructs were consistently ruptured or disintegrated at medium velocities of 3 ml/min or higher in preliminary tests, the pump speed was set to 1.5 ml/min.

During culture, the medium was exchanged twice per week and analyzed for the glucose and lactate concentration, as well as the content of lactate dehydrogenase (LDH) (section 3.10, p. 46). As shown in figure 28, with progressing cell culture time, a reducing concentration of glucose, as well as an increasing concentration of lactate was measured within both bioinks. In both bioinks the LDH value is highest at the first point of measurement (day 5) and is then settling in at 118 - 209 U/l.

After 14 days of dynamic culture, each of the constructs were used for different analysis like Life/Dead staining (section 3.11.1, p. 46) and MTT assay (section 3.11.2, p. 46). For histological analysis, one of the constructs was fixed and embedded in paraffin, as described in section 3.12.1 (p. 47), and hematoxylin and eosin staining (HE) was performed as explained in section 3.12.2 (p. 48). The results of the Alginate-POx constructs are shown in figure 29. No significant shrinkage of the constructs was identifiable objectively, and the pores of the construct and the tissue container are aligned to each other. Qualitative MTT assay showed a homogeneous staining of viable cells throughout the whole construct. Life/Dead and HE staining show a more detailed overview of the construct.

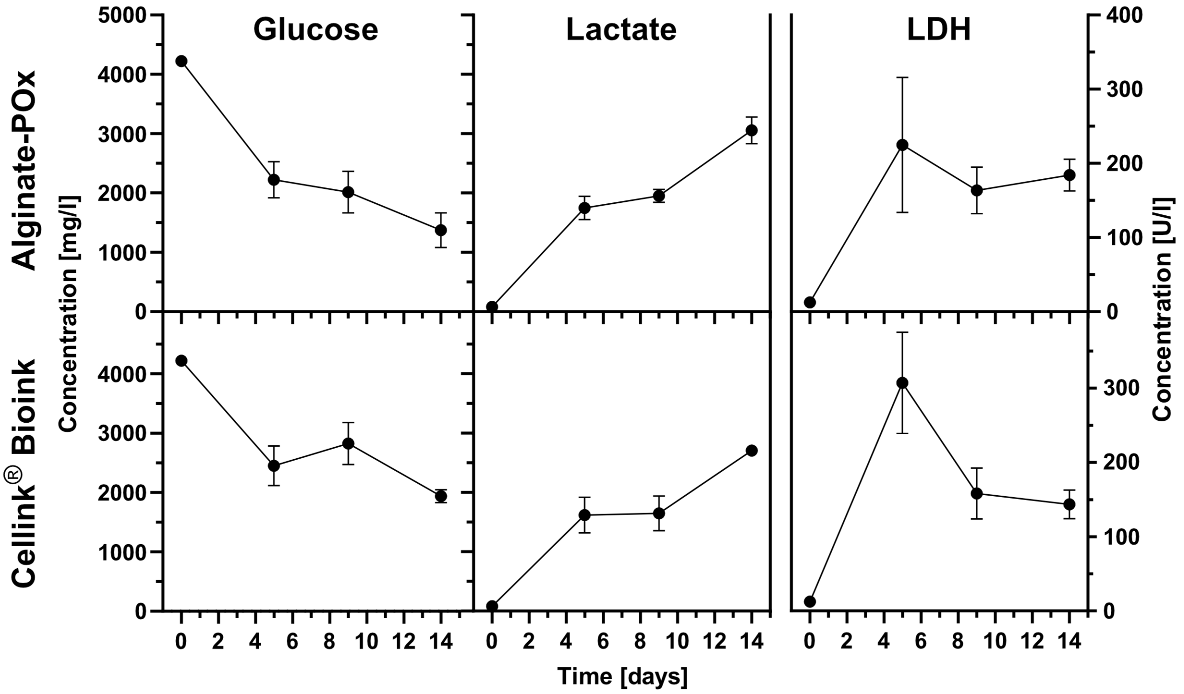

Figure 28: Medium analysis during dynamic tissue culture. Concentration of glucose, lactate and lactate dehydrogenase (LDH) of the medium during perfused tissue culture in the bioreactor system. Medium was analyzed on day 5 and 9, just before a medium exchange was performed, and on day 14. Fresh medium was used for day 0. n = 3.

In Life/Dead staining a homogeneous distribution of viable and dead cells can be observed for the individual areas like peripheral pore, tissue area and central pore. In HE staining, an accumulation of cells are visible in the areas of the peripheral and central channel. In the tissue area, an inhomogeneous distribution of cells is shown forming strand-like shapes according to the nozzle movement during bioprinting.

The results of the Cellink® Bioink constructs are shown in figure 30. Similar to the Alginate-POx constructs, no shrinkage of the constructs was identifiable objectively, showing that the pores of the construct and the tissue container are aligned to each other after dynamic culture. Qualitative MTT assay shows homogeneous staining of viable cells in the construct, even though the printing paths and strands are clearly visible. In contrast to the Alginate-POx constructs, HE staining shows a homogeneous distribution of cells throughout the whole construct, while Life/Dead staining indicated cell accumulations in the area of peripheral and central pore. In the tissue area strand-like shapes according to the nozzle movement during bioprinting are indicated.

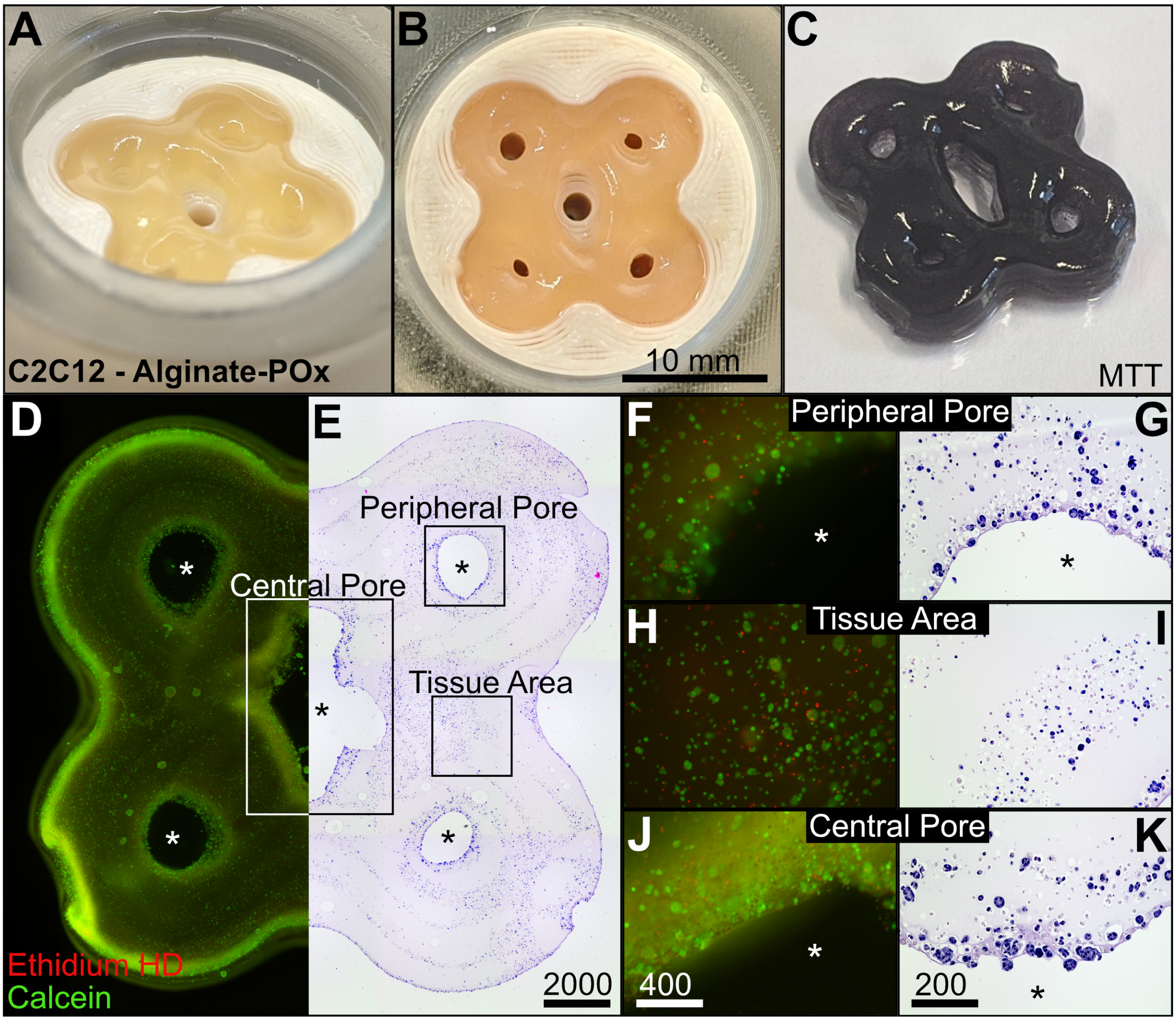

Figure 29: Analysis of Alginate-POx bioink constructs containing C2C12 cells. **(A, B)** Tissue construct after 14 days of dynamic culture. **(C)** Qualitative MTT assay. **(D)** Life/Dead staining of the whole construct and **(E)** HE staining of fixed tissue slices. **(F, G)** Representative sections of areas at the peripheral pore, **(H, I)** the tissue area, and **(J, K)** the central pore. Scale in D-K in µm. Pores are indicated by *.

After successful performance of the bioreactor experiments comparing the both bioinks using C2C12 cells, adipose differentiation of hMSCs was tested as well. Unlike the C2C12 cellline, hMSCs are a primary cell source with higher demands on the environment and higher correlation to a patient-specific tissue. 2 mio cells/ml were mixed with Cellink® Bioink and printed as described above. Medium was changed from expansion medium to adipose differentiation medium as described in section 3.1.2 (p. 37). After 21 days of dynamic culture, the constructs were analyzed the same way as the experiments described above. The results are shown in figure 31: According to the Cellink® Bioink construct containing C2C12 cells,

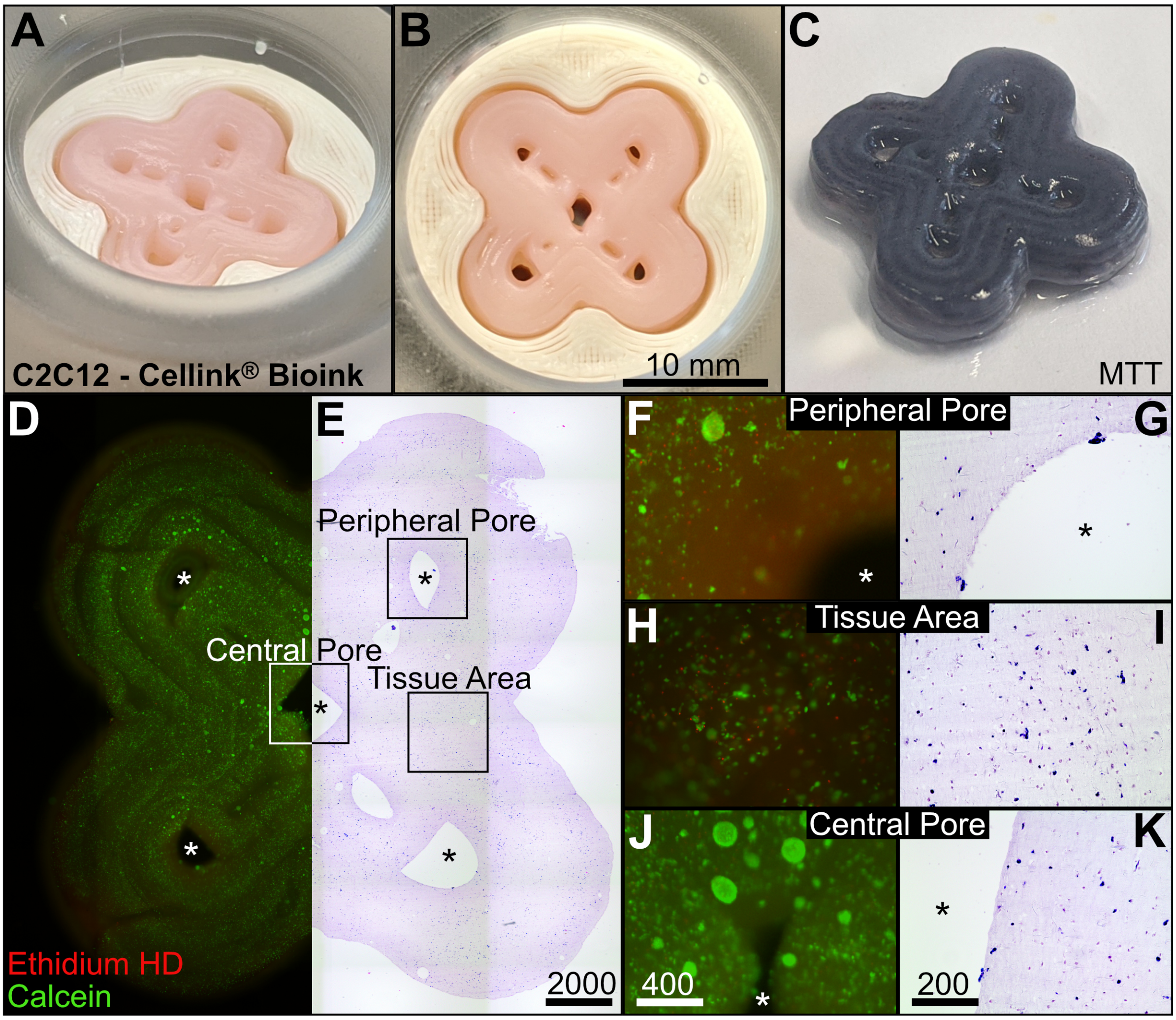

Figure 30: Analysis of Cellink® Bioink printed constructs containing C2C12 cells. **(A, B)** Tissue construct containing C2C12 cells after 14 days of dynamic culture. **(C)** Qualitative MTT assay. **(D)** Life/Dead staining of the whole construct and **(E)** HE staining of fixed tissue slices. **(F, G)** Representative sections of areas at the peripheral pore, **(H, I)** the tissue area, and **(J, K)** the central pore. Scale in D-K in µm. Pores are indicated by *.

no shrinkage of the constructs with the hMSCs are identifiable objectively. The pores of the construct and the tissue container are aligned to each other after 21 days of dynamic culture. Qualitative MTT assay shows homogeneous staining of viable cells in the construct with the printing paths visible. Life/Dead, as well as HE staining, show homogeneous distribution of cells throughout the whole tissue construct, even though printing paths are visible in both stainings. No accumulation of cells is shown in the construct. Detailed HE staining of the cells show differentiated hMSCs with a high amount of lipid vacuoles.

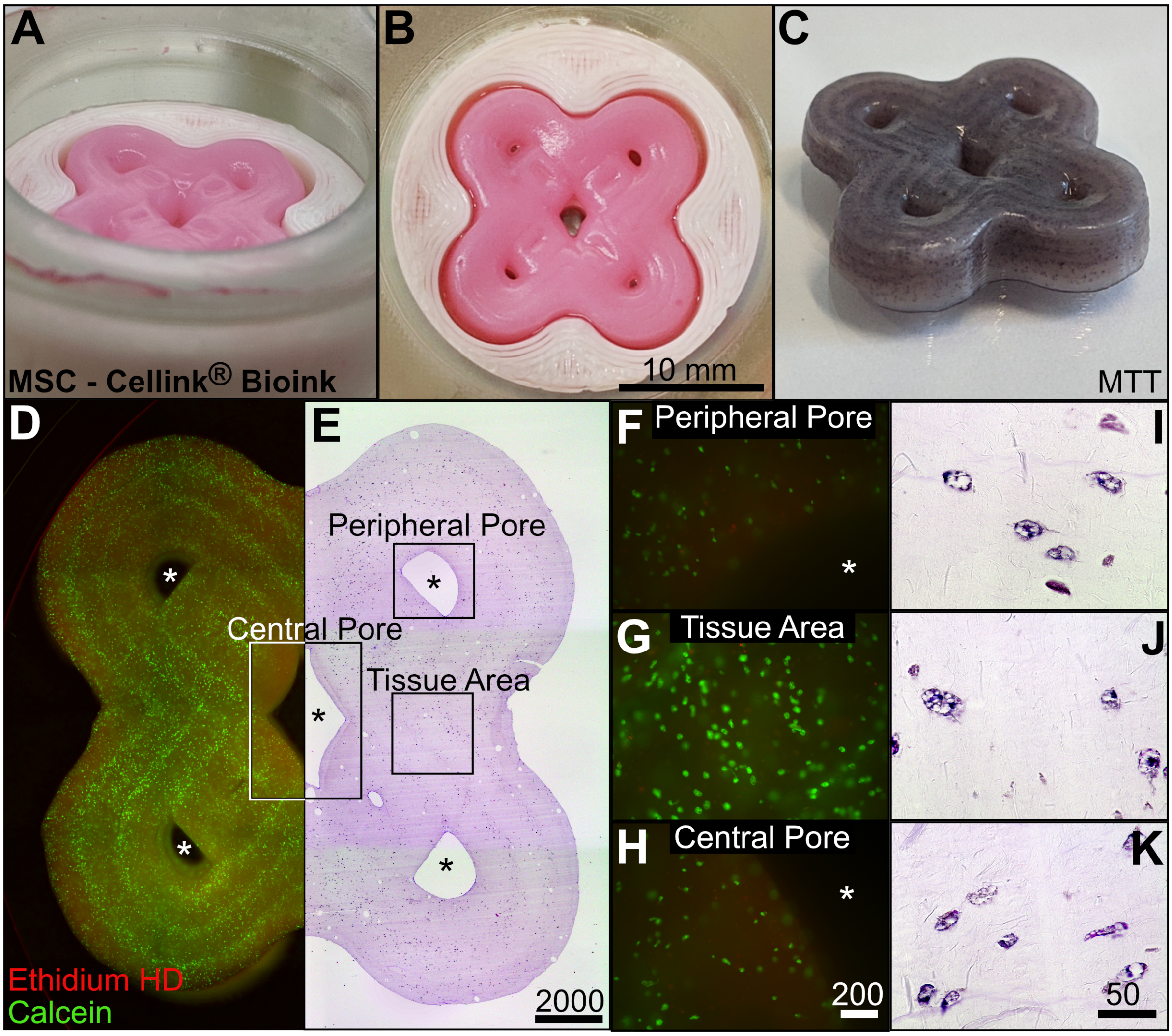

Figure 31: Analysis of hMSCs-containing Cellink® Bioink constructs. (A, B) Tissue construct containing hMSCs cells after 21 days of dynamic culture. **(C)** Qualitative MTT assay. **(D)** Life/Dead staining of the whole construct and **(E)** HE staining of fixed tissue slices. **(F)** Representative sections of areas at the peripheral pore, **(G)** the tissue area, and **(H)** the central pore. **(I-K)** Adipose induced hMSCs. Scale in D-K in µm. Pores are indicated by *.

4.3.3 Transition to combined Printing

After performing cell-containing experiments and proofing the functionality of the developed bioreactor system, efforts were taken to transfer the sequential printing method to a combined one. As shown in figure 32, printing the Flower5 tissue container required 7.4 ml of material, as well as a printing time of 41 min. Taken into account, that the bioink has to be installed before starting the printing of the tissue container in a combined printing approach, the printing time was considered to be to long, leading to sedimentation of cells in the bioink. Additionally the cartridges used within the printer has a theoretical maximum volume of 3 ml, which thereby is not applicable with a geometry of bigger volume. This is why the tissue container was splitted into a spacer that can be preprinted, and a reduced geometry of the tissue container. This reduced version can be printed by 1.2 ml with a reduced printing time of 10 min.

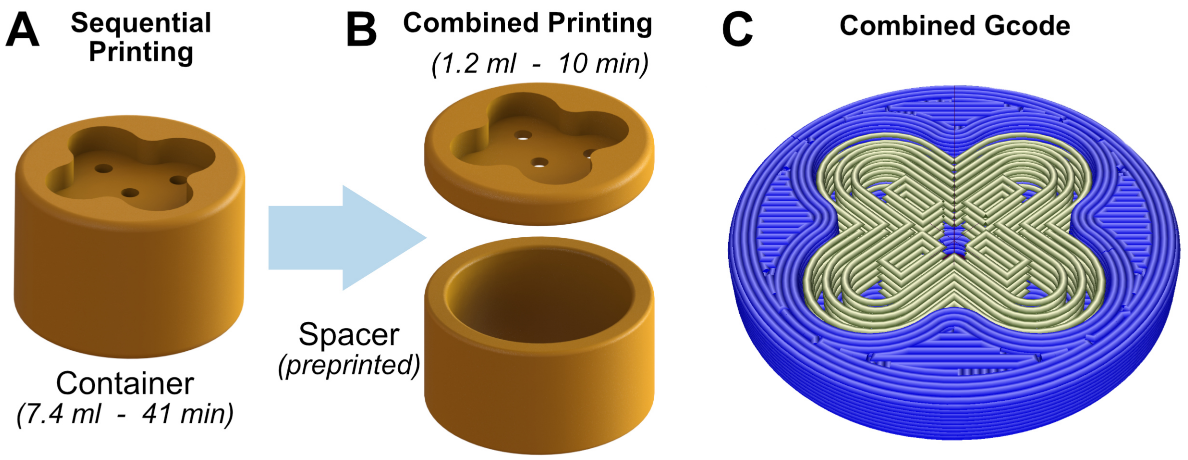

Figure 32: Preparation for combined printing. The tissue container used for sequential printing is splitted into a spacer-part, and a reduced version of the tissue container. Gcodes for the tissue container and the tissue construct are combined and adapted to the individual printer.

For combined printing, both Gcodes of the construct, as well as the tissue container, were combined within RepetierHost software that way, that one printhead was used for printing the tissue container, and a second one for printing the tissue construct. Since combined printing was not possible with Cellink® Inkredible+™ due to the lack of a thermoplastic printheads, the Gcode was adapted to the Cellink® BioX printer instead. The actual operation of the combined printing process was performed by Susanne Heid at the University of Erlangen (FAU). It turned out that the cartridges of the printer do have a significantly lower extrusion volume in reality than the theoretically stated 3 ml. So, the Flower5 construct could not be combined printed due to device-specific technical limitations. As a proof of concept for the combination of the two printing techniques, the combined printing was realized for an early-state version of Square1 (Fig. 33).

Figure 33: Combined printing of an early-state Square1 shape. Printing of the combined printed construct was performed, and the photo acquired, by Susanne Heid.

With successful proof of concept for the combined printing, a second guidance was developed for approaching combined printing of individual wound defects (Fig. 34): Within step 0, a patients wound geometry could be aquired at the clinics, using for example 3D scanners or similar technologies. In step 1 and 2 the geometry of the to-be-printed tissue construct is designed and transferred to Gcode using the raw geometry data from the clinics, as well as individual bioink properties gained by bioink development. After that the tissue container is designed and transferred to Gcode in step 3 and 4, according to the designed tissue construct. In this steps, material- and printer-specific parameters and properties are taken into account gained by analysis of the printer limitations as described before. In step 5, both Gcodes are combined for the individual printer used and after that, the combined printing is performed in step 6. After printing, bioreactor assembly and dynamic culture is performed related to the bioreactor development as described above (step 7 + 8). In a last step, the generated tissue could be implanted to the patient.

4.4 Automated Docking Station for Bioreactor System

After the development of the combined printing method, the degree of automation should further be improved by designing a device, capable of taking over repeating tasks, like media exchange, and enhancing general handling within the lab. Therefore, a full list of requirements was set up and evaluated as shown in table 14.

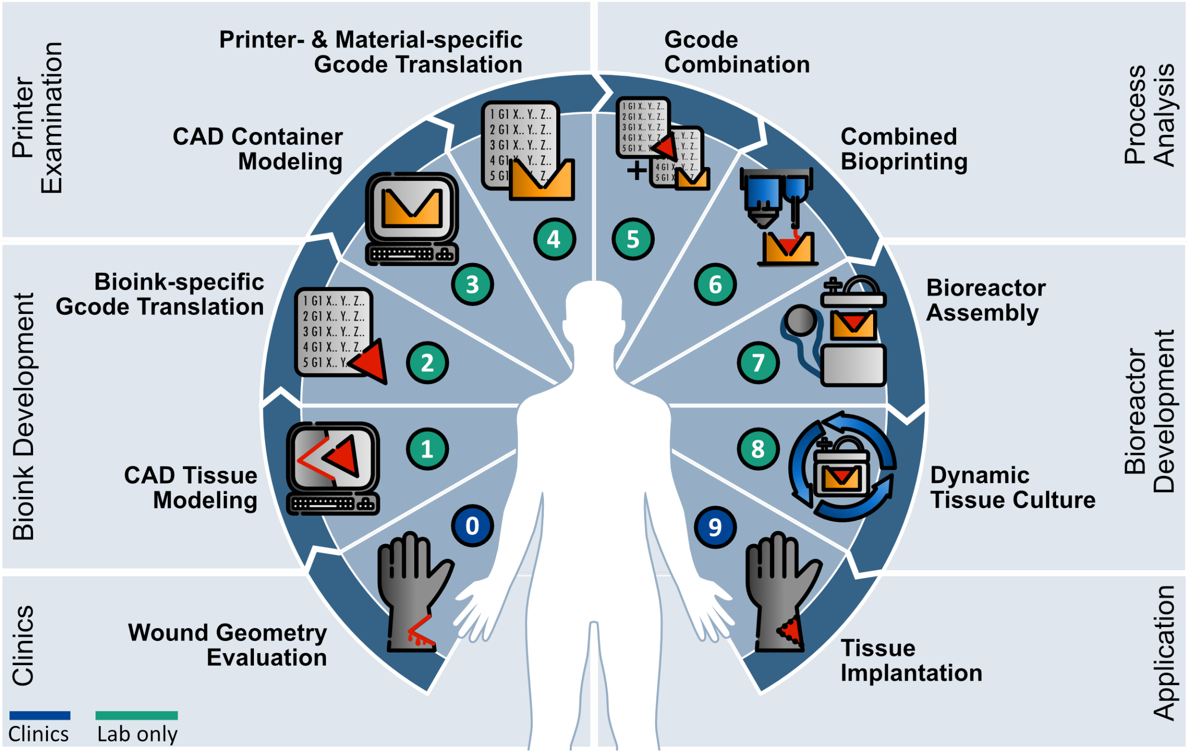

Figure 34: Refined guidance for patient-tailored bioprinting. Starting with geometry assessment of wound defect by e.g. 3D scanning methods **(0)**. According to wound data the effected piece is modeled by CAD **(1)** followed by translation into tissue- and printer-specific Gcode **(2)**. Next, the derived tissue container is designed **(3)** and translated into material- and printer-specific Gcode **(4)**. Gcodes are combined to a working-file for individual printers **(5)**. Tissue container and construct are printed by combined printing approach **(6)** and installed to the bioreactor system **(7)**. Dynamic perfusion culture is applied for proper tissue maturation **(8)** until translation into the patient **(9)**.

According to this list, a tubing system was conceptualized including the two chambers of the bioreactor, the tissue chamber and the medium reservoir, as well as two external compartments for new medium and waste. To switch the flow destination between the chambers, valves were conceptualized accordingly. Figure 35 showing the concept of automated medium exchange depicted as fluidic diagram: both compartments of the bioreactor are connected to each other forming a circuit that is installed to both valves and the pump. Additionally, the waste is connected to the tubing system and installed to pinch valve 1. Likewise, the new medium compartment is connected to the tubing system and valve 2. In untriggered state, the connection to the waste and the new medium are closed by the valves.

Table 14: List of requirements for an automated bioreactor dockingstation

Priority	Requirement	Minimum acceptable	Target	Ideal
M	Medium exchange	>1 button after manual medium preparation	1 button after manual medium preparation	Integrated medium reservoir with scheduled medium exchange (full automation)
M	Pump Speed	1.5 ml/min (fixed)	0 - 10 ml/min (manually adjustable)	0 - 10 ml/min manually and automated pressure controlled
M	Case sealing	Simple enclosure for save handling and protection of electronics	Dustproof	Waterproof
M	Battery capacity	0.5 h	0.5 - 2 h	> 2 h
M	Size	Fits into standard size incubator	Transferable into cleanbench with glas front fully open	Transferable into cleanbench with glas front in working position
M	Human machine interface	No screen, physical buttons	Status-screen, physical buttons	Graphical touchscreen with integrated buttons and graphs
M	Error free runtime	2 weeks	3 weeks	4 weeks
M	Material costs	< 500 €	< 300 €	< 150 €

M	Availability of components	Custom-manufactured	Regular available	Regular available or selfmade (e.g. 3D printed)
W	Interrupted perfusion during medium exchange	< 15 min	< 5 min	0 min
W	Weight	< 10 kg	< 5 kg	< 1 kg
W	Medium temperature control	35 - 38 °C	35.7 - 37.7 °C	36.3 - 37.4 °C
W	Tissue stimulation	Electrical	Electrical, mechanical	Electrical, mechanical, biochemical
W	Monitoring	Temperature, pH	Temperature, pH, filling level, glucose	Temperature, pH, filling level, glucose, lactate, LDH, pressure, oxygen, live-imaging
W	Remote access	Room-wide	Department-wide (intranet)	Global (internet)

M = Must-have, W = Wish/Nice-to-have, grey filling = achieved

That way the medium is being pumped from the medium reservoir of the bioreactor through the pump into the tissue chamber holding the tissue, and back into the reservoir as described before. When valve 1 is triggered, the connection to the waste is opened and the connection to the tissue chamber is closed. The medium is pumped into the waste and the medium reservoir gets depleted. When valve 2 is triggered in contrast, the connection to the medium reservoir is closed and the new medium compartment is connected to the tubing system. The new medium is pumped into the system and the medium reservoir is refilled again.

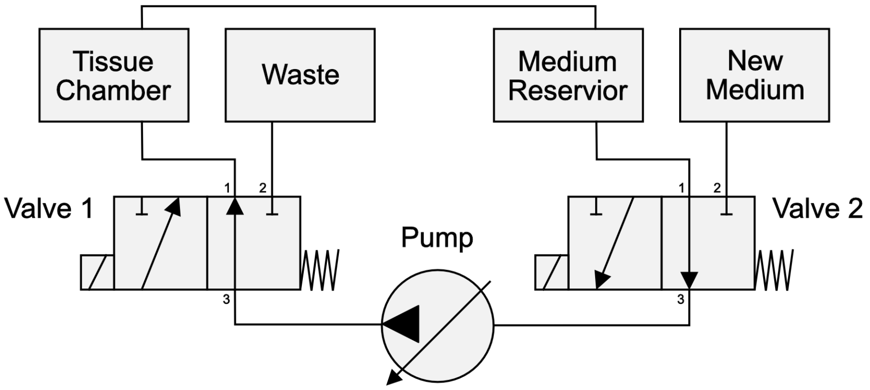

Figure 35: Fluidic diagram of the automated tubing system.

In a next step, the electrical hardware setup was derived from the list of requirements and the fluidic diagram. First, an Arduino UNO R3 microcontroller was used as the computing unit of the system. Due to high availability of logical components and low costs, combined with an open-source architecture and modular design principle, this microcontroller is particularly well suited for such tasks. Next, standard 14 V 3/2-way pinch valves with a normal-open and a normal-closed port were used as valves for the tubing system. To enable mobile operation, a PWM solar charging controller was used to automatically switch between the wall adapter power supply and a lithium iron phosphate battery (11-14.6 V, 3 A h). It controls charging of the battery when the device is connected to a power supply. If the power supply is removed, but the device is not turned off, the PWM solar charging controller automatically switches to power supply by battery. This enables a mobile operation of the device. A so-called NEMA 17 stepper motor with a peristaltic pumping unit attached served as a pump.

With having selected the most important components of the system, the electrical circuit diagram was developed (Fig. 38). To buffer electrical peaks in the moment of turning on or off the system, a capacitor (16 V, 1000 µF) was installed. For the same reason, the valves are connected to a schottkydiode each (1N5820) to deal with electrical peaks generated by induction when the valves are released. The valves are operated by a 2-relay-module triggered by the Arduino UNO R3 microcontroller. A stepper motor driver module (DRV8825) was used to control the pumping motor. periphery of the device contains a stainless-steel button to trigger the automated medium exchange, a battery charge indicator, as well as a LCD screen to displaying most relevant status information. A rotary button was also implemented to manually changing the pump speed.

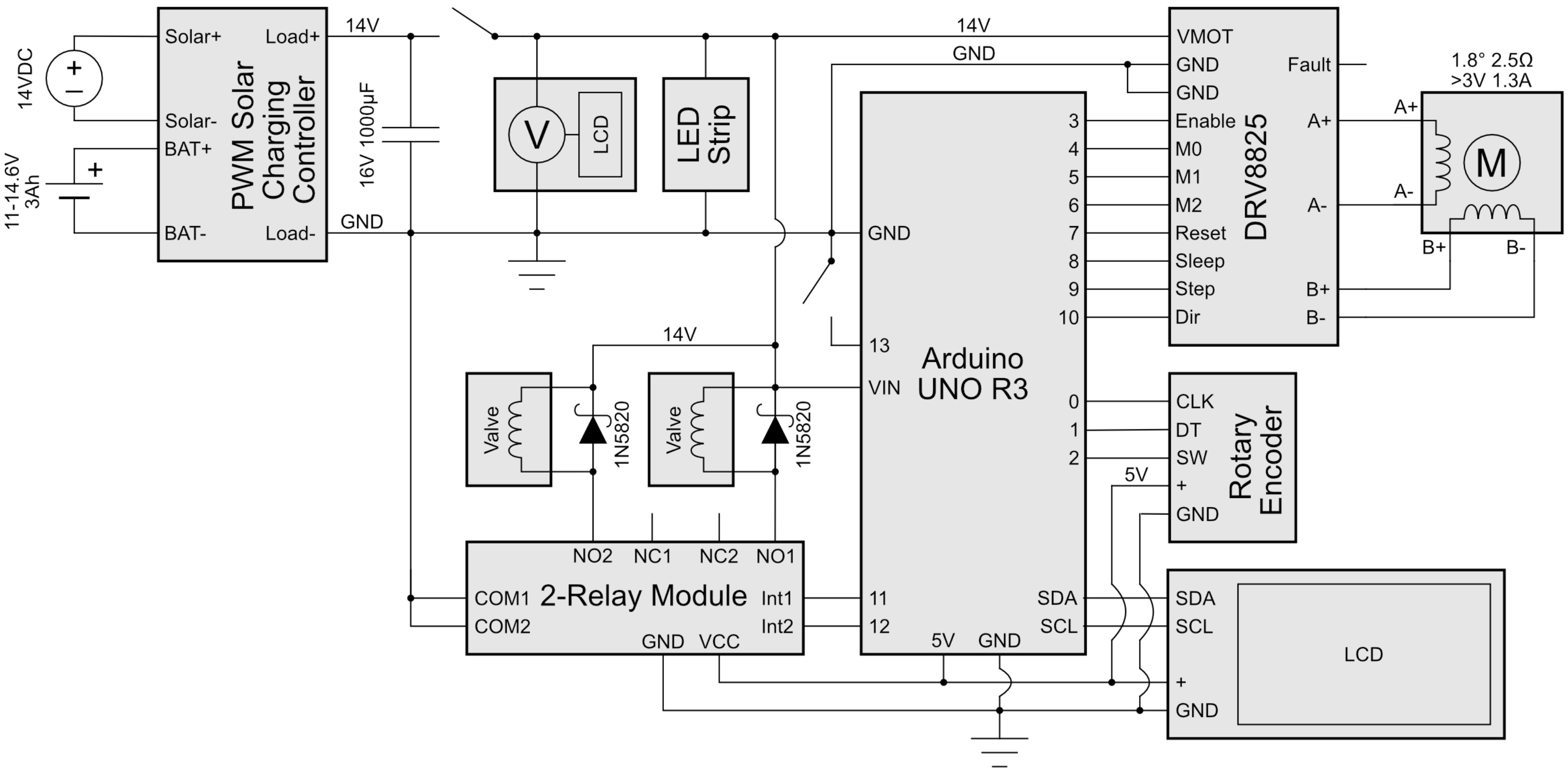

Figure 36: Electrical circuit diagram of the automated system.

A special printed circuit board (PCB), called Arduino UNO Protoshield, was used to realize the electrical circuit diagram. The Protoshield board is designed to fit to the Arduino microcontroller and connects the logical pins of the board to the according pins of the microcontroller. The layout of the board and assignment of the pins is shown in figure 37.

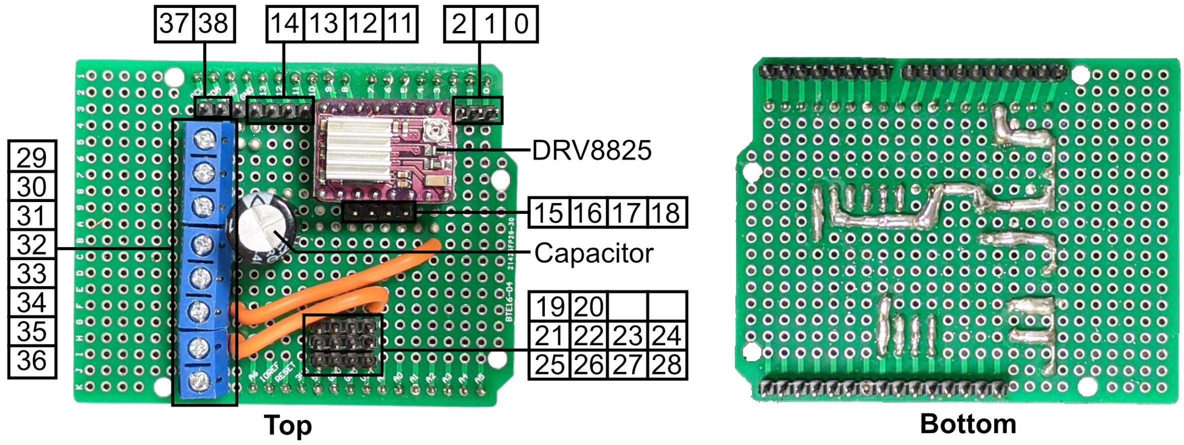

Pin	Assignment	
0	CLK	Rotary encoder
1	DT	
2	SW	
11	Int 1	Relay module
12	Int 2	
13	Button	
14	Button	
15	A-	Motor
16	A+	
17	B+	
18	B-	
19	+	Rotary encoder
20	GND	
21	+	LCD screen
22	GND	

Pin	Assignment	
23	GND	Battery charge indicator
24	+	
25	+	Relay module
26	GND	
27	GND	LED strip
28	+	
29	COM1	Relay module
30	COM2	
31	Load-	PWM solar charge controller
32	Load+	
33	ON/OFF switch	
34	ON/OFF switch	
35	Valve 1	
36	Valve 2	
37	SCL	LCD screen
38	SDA	

Figure 37: Layout of the Protoshield board and pin assignment.

After assembling the hardware parts of the docking station, the firmware was programmed for the Arduino. The full firmware code is shown in Code 4 (p. 122) and depicted in figure 38 as flow chart. After the prevoid settings, the pins, variables, and initial states are defined in the void setup() function. Afterwards the device enters the void loop() function which runs the motor and is repeated infinitely until either the button or the rotary encoder is triggered.
If the rotary encoder is actuated, the software enters the void ChangeSpeed() function. In this function, the rotation direction of the encoder is detected and the encoder level gets

updated. Next, the screen is updated for the new pump speed value and the according steps per time are calculated for the stepper motor driver module. At the end, the sleep-mode-PIN is toggled true or false whether the pump speed equals 0 or not. This mode is saving energy and increases the lifetime of the electrical parts. The software then enters back to the void loop() function.

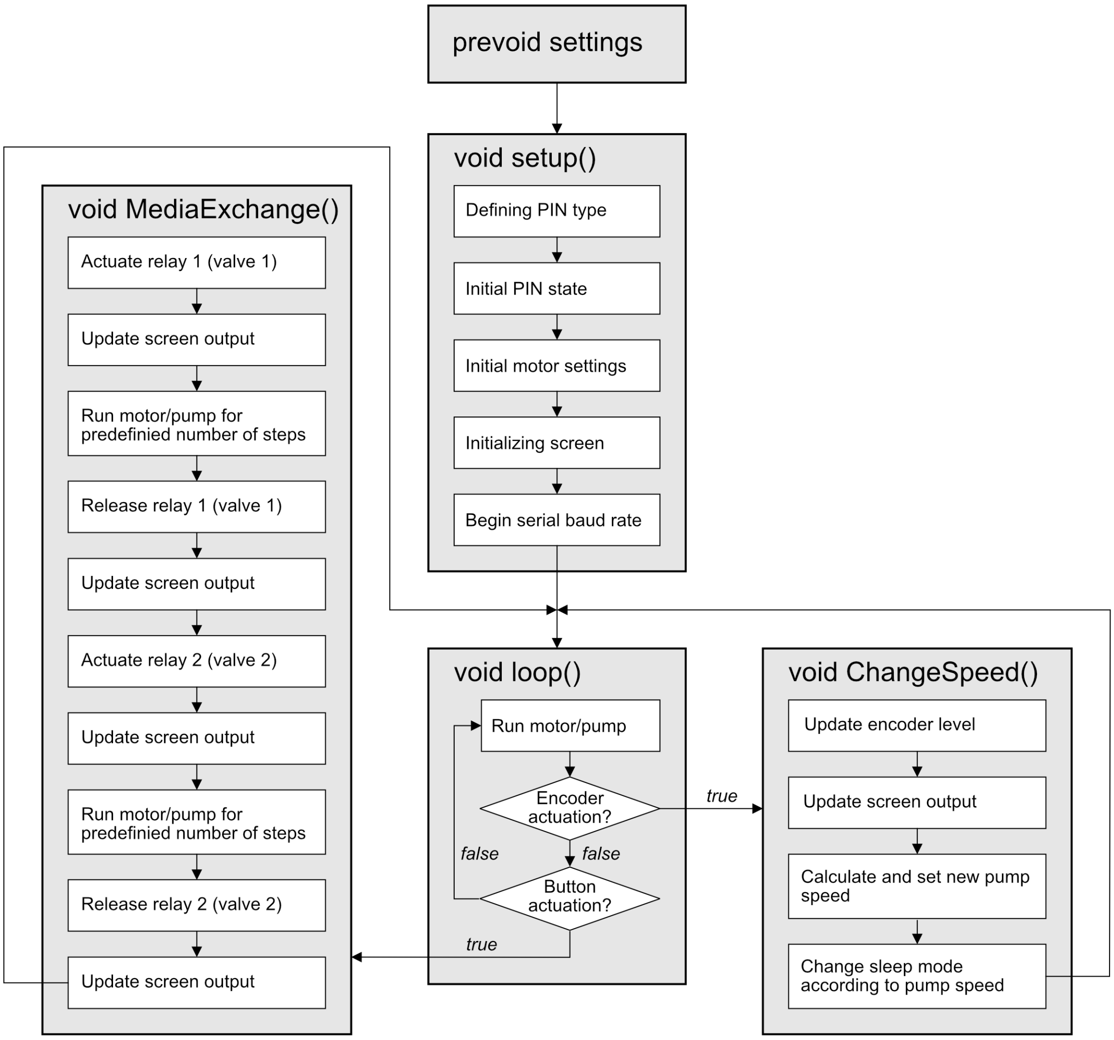

Figure 38: Software flowchart of the automated bioreactor docking station.

If the button for the medium exchange is actuated, the void MediaExchange() function is entered. First, relay 1 is triggered, which activates valve 1. During that, the LCD screen is updated showing the current step of the medium exchange. Additionally, the motor (=pump) is running for a predefined number of steps. The number of steps needed for the medium reservoir to get emptied or filled was investigated empirically before and is hard-coded into the software. After the stepper motor driver has run the motor/pump for that precalculated number of steps, relay 1 (valve 1) is released and relay 2 (valve 2) is triggered. The same steps as described above for valve 1 are repeated. That way the bioreactor is refilled with new medium. At the end, relay 2 (valve 2) is released, the screen is updated to the standard screen and the void loop() function is entered back again.

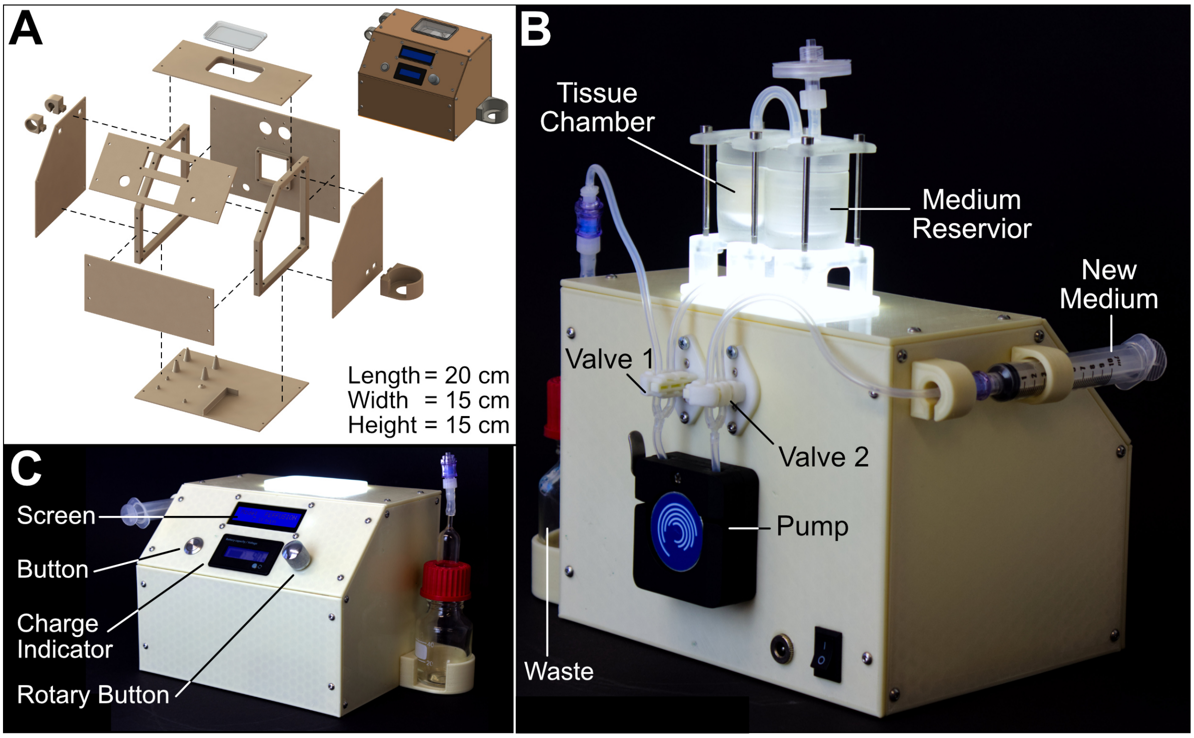

Figure 39: Automated docking station for the bioreactor system. (A) Exploded view of the 3D-printed housing of the device made from Green-TEC Pro - Nature filament. **(B)** Back view of the automated docking station with installed bioreactor and tubing system. **(C)** Front view of the automated docking station.

In the end, a housing was designed to encapsulate the electrical components and protect them from dust. The housing was designed to fit under the cleanbench and having the screens and buttons being presented at the front for easy accessibility. The enclosure components (Fig. 39 A) were 3D-printed by Green-TEC Pro filament to reduce cost and weight. Next to the device, a syringe holder was added. The syringe is used as the new-medium-compartment containing the preheated new medium. A glass bottle, serving as waste for the old and used medium, was attached to the other side of the device. Both compartments can be connected to the tubing system using sterile, valve-like, one-way LUER-connectors. The bioreactor can

be docked on top of the device. The pump and pinch valves are installed at the back of the device. The summarized costs of the docking station were about 260 €.
The final docking station with installed bioreactor and tubing system is shown in figure 39. With this automated docking station device all must-have requirements were fulfilled with 22.2 % minimal required, 44.4 % target and 33.3 % ideal quality. 33.3 % of the nice-to-have requirements were fulfilled by target quality and 66.6 % were not fulfilled. The individual achievements are indicated in the list of requirements (Fig. 14, grey filling).

5 Discussion

5.1 Standardized Guideline for 3D Printer Analysis

Even though 3D printing techniques are increasingly used in life sciences, the handling, development, and standardized printing of research-grade geometries is still not a straight forward approach. Especially combination of material sciences and printing techniques, as well as bioreactor development, require specialized know-how to operate 3D printers. To address these limitations, we focused on a standardized way to approach bioreactor development in Tissue Engineering:

In a first step, a set of test bodies was designed. This test bodies show a simple geometry and are therefore easily manageable by commercial 3D printers. Due to the distinct design of one parameter per test body, the printed results can be visualized using common light microscopes. This way prevents low-quality-areas of one parameter interferings with other regions of the test body, as it is the case for test bodies, that have a variety of holes, bars and overhangs fused together in one piece. The parameters used for the test bodies were chosen to be the most important for developing bioreactors without needing support structures during the printing process.

Due to the limitless amount of printer and slicing settings, that show different impact to the final printed result, depending on material, geometry, and individual device, settings were chosen, that show an acceptable compromise of printing time and surface quality. It could be shown, that a loss of accuracy is not only due to material properties and device hardware limitations, but also caused by the slicing algorithm and the software used for it. All of them are thereby high potential targets for quality improvement.

Clearly, the different printing techniques FDM/FFF, SLA, and SLS have their unique advantages and disadvantages, which gives them their own niche of application and makes it hard to compare them here one-to-one. FDM shows easy handling, less waste, relative cheap materials, and fast printing times, but has a rather low quality compared to other techniques. The best benefits of the FDM technique can be met by rapid prototyping applications. SLA-technique showed the best surface quality and printing accuracy, but also required longer printing times than FDM printing, as well as more costly materials. SLS printing in contrast is able to print without any support structures. Unfortunately, post-processing efforts could not be reduced on the parts and the materials used, due to a high number of particles that sticked to the pores of the printed parts. Even major efforts for cleaning did not overcome this issue. Also, the quality and accuracy of the specific SLS printer device was not appropriate for cell culture applications, which is why design criteria for this technique couldn't be stated. The novell standardized guidance, which was used for comparing the printing techniques, enables to derive recommended design limitations for FDM and SLA from the results. According to the design criteria of the test bodies, design limitations could be stated for X-, Y- and Z-resolution, as well as channels printed horizontally and vertically, unsupported overhangs and leakage-proof wall structures.

Interestingly, both techniques show identical values in most of the recommended limitations: Even though the specific overall tolerances of the techniques and devices are varying, structures should not be printed smaller than 500 µm in X- and Y-direction, as well as lower than 200 µm and 50 µm in height for FDM and SLA respectively. The limiting height is strongly depending on the layer height setting of the printer and can be varied easily, but also has a great impact on the resulting printing time. Horizontal channels in both techniques should not be printed smaller than 1.5 mm in diameter, respectively 1 mm for vertical channels. In terms of unsupported overhangs, both techniques show a recommended limit of 40°.

Wall thicknesses for printing bioreactors is recommended to be 2 mm or thicker. For SLA even smaller thicknesses showed leakage-proof, but since the overall stability and integrity of the printed parts is related on the wall thicknesses, it is recommend not to use them thinner than 2 mm. In this case, not all FDM printers used were able to print leakage-proof walls even with 2 mm thickness. This shows clearly how different the impact of printer settings can be, when comparing devices of the same technique, printing with the same materials. Printing approaches therefore should always made after the device was analyzed and quantified by using the deveoped guideline.

Since there is an increasing pallet of usable materials for 3D printing, desicion was made to go for one representative material per printing technique as proof of concept in this work: The resin Dental SG (secret composition) was used due to its application in dentistry and stated biocompatibility by the manufacturer. For SLS, nylon-based material was used due its inert properties. For FDM-printing, Green-TEC Pro filament was used. This material based on lignin is made from natural polymers and is approved by the FDA for biocompatibility. It is certified degradable by DIN EN ISO 14855 [132] and therefore shows low impact to the environment. This material was used due to these properties and the rather low costs.

As proof of concept for the guidance, it was successfully given to independent labs for standardized analysis of their specific printer devices. The task was the same as described above: Finding a suited compromise of printing time and quality. Additionally, the FDM printers could be compared to each other by their specific advantages and disadvantages. In the result both Ultimaker printers (3 and S5) showed less accuracy in the printed parts compared to the Raise3D Pro II, but were instead able to print leakage-proof walls with a thickness of less than 0.5 mm.

5.2 Impact of Sterilization Methods to Material Properties

As an additional part of the standardized guidance, the change of material properties after sterilization was investigated. Again, as proof of concept only two sterilization techniques, autoclaving and vaporized plasma sterilization, were tested as representatives in this work. Autoclaving was chosen due to its gold standard status in Life Sciences, and vaporized plasma sterilization since it is stated to be a gentle method with low impact to the material [133, 134]. As expected, it was shown that tensile and flexural strength is significantly reduced in lignin when autoclaved up to three times. Compared to plasma treatment, no significant change was identified.

In SLA and SLS, no significant strength reduction was observable, but tendency for decreasing strengths can be seen in higher autoclaving stages. Again, no significant loss of properties was shown in plasma treatment. Due to this, autoclaving of 3D-printed parts is recommended only when handled as single-use in cell culture. To increase lifetime of parts that are used multiple times, plasma sterilization is recommended instead. Of cause, other sterilization methods like UV-light, gamma-radiation, or ethanol can be tested by the same methods of the guidance and classified for their best use.

As stated at the beginning of this work and shown in the guidance, biocompatibility is a major crucial parameter for bioreactor development. Due to the limitation to the FDM technique for the development of the bioreactor (see explanation in the next section), all those materials that were involved in the production of the final bioreactor parts were analyzed.

According to DIN EN ISO 10993-5 [127], that states 70 % to be the transition from biocompatible to non-biocompatible, lignin showed a biocompatibility of roughly 80 % when autoclaved once after one day of incubation with the medium. However, biocompatibility decreased slightly below 70 % after 14 days, and increased slightly above 70 % after 24 days of incubation. To clarify the question for biocompatibility in this situation, PLA was tested also as the gold standard material used for 3D printing. PLA is also used for long term cell culture and stated to have inert properties for these approaches. This tests also showed a decreased biocompatibility slightly above the 70 %-mark. Due to this, Green-TEC Pro material also claimed to be positive biocompatible. A possible reason for this rather negative results could be, that the medium was not exchanged for those 14, respectively 24 days, while incubation, and thereby most of the proteins and growth factors could have been already degraded due to their half-life. Which means, that the medium used for the biocompatibility experiments didn't showed the same composition as it is in fresh medium.

PDMS, as the material of the main parts, as well as the Dublisil® silicones, which were used for production of the PDMS parts, showed positive for biocompatibility. This ensured at full biocompatible manufacturing of the bioreactor parts and drastically reduces the chance for bioincompatible residues on the parts.

As stated above, some parts had to be plasma sterilized, so biocompatibility was also tested after this sterilization method. Although the plasma sterilization process showed no significant impact to the different printed materials in terms of mechanical properties, it was not biocompatible at all directly after sterilization ($< 1\,\%$). Neither washing with PBS$^-$, PBS$^+$, incubation with ultra-pure water for one day, nor leaving it untreated for 7 days led to a positive biocompatibility. Only if the parts were left untreated after sterilization for 14 days, biocompatibility was positive. I can be assumed, that the functional groups, generated by activating the surface during the sterilization process as shown in literature [135–137], somehow interact with the medium ingredients, causing major damage to the proteins and growth factors. This surface activation is only reduced by time. However, this is only an assumption and needs to be investigated in detail in future. As a conclusion for this work, decision was made to use plasma sterilized parts after 14 days of sterilization treatment earliest.

5.3 Development of a 3D-Printed Bioreactor Platform for Sequential Printing

This work was aiming for combined printing, so a technical solution for combining a 3D printing technique and a bioprinting technique had to be found. In this case, FDM printing and extrusion-based bioprinting was chosen for three reasons: First, even though FDM printing does not show the best surface quality, it is the easiest to handle, cheap, and most common technique so far. Second, FDM is the most adaptable technique, since nearly any setting and parameter can be changed manually. The third reason was interlaboratory-exchange, the share of common knowledge, and research synergies within the transregional research consortium TRR225. Therefore, devices (Cellink® Inkredible+™ and Cellink® BioX) were chosen, that could be easily distributed to a high number of labs.

Both devices are based on material extrusion techniques, which limited the development of the 3D-printable bioreactor platform to these techniques. The development of a geometry, that included all aspects for this aim, like low printing time, high shape fidelity, perfusable, leakage-proof, no support structure since no post-processing could be done, and the ability to automatically print a tissue inside, showed the trickiest aspect of this whole work. To approach this challenge step by step, a prototyping trial-and-error method was used: Bioreactor parts were designed, printed, and tested on a rather high frequency. The most important iterations shown in this work include a simple cup-like shape which was taken as a starting point of development. Iteration by iteration short-comings and limitations were solved, ending with a rather complex bioreactor-shape in between. Since leakage was the most persistent issue, a full encapsulation with parts made from PDMS was realized. Because the negative molds for the PDMS parts are custom-made using 3D printing technique (as explained in section 3.9.2 43), the shape-fildelity could be maintained. It must be noted that static and dynamic systems behave completely different in terms of leakage-proof. During the development, it became clear that interfaces with FDM-printed parts, even though they were Lignin-PDMS-interfaces, are not able to form tight assemblies in a dynamic setting. This could be due to the layered surface of the FDM-printed parts which benefits capillary effects.

Another issue was the detachment of the bioprinted construct from the perfusion connections. This problem was overcome by perfusing the tissue vertically instead of horizontally. Since FDM printers can print vertical channels with much higher accuracy and better quality, as tested before, this was a secondary benefit of this approach. With this solution, it was possible to reduce the printed part even further to a simple container-like shape encapsulated in a housing and a lid made from PDMS.

After optimizing the design, the housing was designed to hold the 3D-printed container and included a medium reservoir. By adding a medium reservoir to the casted PDMS-part, the total amount of parts needed for the setup could be drastically reduced. This reduces the overall number of interfaces in the system and decreases the chance for contamination and leakage. The simple shaped cylinder-like tissue container could be reshaped for a variety of tissue geometries by adapting the pore arrangement and the inner structure but keeping the outer size persistent.

Further minor improvements to the bioreactor concept included an undercut geometry at the backflow from the tissue chamber to the medium reservoir. Since the medium was meant to drop from the lid back into the medium reservoir, this undercut geometry supports the controlled formation of droplets and prevents hydrostatic and capillary effects. Level indicators were implemented to the medium reservoir for a convenient handling and optical control of the bioreactor. By designing a curved bottom of the medium reservoir, a funnel-like function is indicated. This prevents the formation of dead slipstream areas and enables the full depletion of the reservoir. Lastly, the lid-area at the tissue was shaped that way, that it is holding the tissue at pace and prevents it from detaching when perfused with medium. This way the developed bioreactor system was used for dynamic tissue culture.

5.4 Construct Shape Analysis and Bioprinting Process

The degree of freedom of the bioreactor design was showed by designing a set of different tissue shapes, including a unique setup of pores. The according tissue container was easily derived from the various tissue shapes. The Gcode was written manually for each individual shape by using NIVEA® lotion as bioink replacement. This way, the specific coordinates and parameters of the Gcode could be derived. In this approach, a strand distance of 1 mm, a first layer height of 0.4 mm, and 0.6 mm for the following layers showed the best printing quality. The diameter of the pores was set to 2 mm (2.8 mm in Column-shape), and printing was performed using 0.41 mm nozzles. This showed the best compromise of printing time and quality.

Thinner nozzles could have been used, resulting in higher pressures and printing time, but also in higher quality, while broader nozzles would have significantly reduced the printing time, as well as the shape fidelity. All in all, bioprinting shows a complex interaction between the parameters of nozzle diameter, printing speed, bioink viscosity and pressure. These parameters must be adjusted individually for every approach, bioink, and shape, and can hardly be standardized. For the NIVEA® lotion testing, printing speed was set to 600 mm/min. Fine-tuning was performed by using the hydrogel Cellink® Start.

In order to print inside the containers, first a special designed adapter plate was 3D-printed to fit into the bioprinter and holding the preprinted sterilized tissue containers. Using blunt steel nozzles, the tissues could be printed into the container using the Cellink® Start hydrogel. Using NIVEA® lotion, followed by Cellink® Start, makes a convenient way to approach bioprinting settings and Gcode design, that is cheap, resource-conserving, and environmentally friendly.

Using CFD software, medium flow, shear stress, and nutrient concentration within the individual shapes could be predicted. This way it could be shown, that unequal shaped pores, like in the smiley-shape, do not support an equal nutrient supply in the tissue. Additionally, it was shown, that a single pore in tissues like Square1 and Flower1, leads to reduced glucose concentrations in the outer tissue regions. Due to its specific geometry, the column-shape was fine with a single channel. Square4, Flower5, and the iconic heart-like-shape were designed with equally distributed pores over the whole construct and accordingly showed higher concentrations on glucose within the tissues. Even though the simulation represents an idealized simplification of the complexity of the tissues, the simulated concentration gradients of the shapes are to be considered realistic. This is due to the symmetrical structure of the individual tissues and the decreasing concentrations from the pores and the upper surface into the tissue.

An important finding is, that by *in-silico*-simulation it was shown, that the pores within a multi-pore-shape are equally perfused by medium (equal medium velocity). This is an important indicator for the medium supply of the tissue. The initial medium flow of these simulations, as well as in the final biological experiments was set to 1.5 ml/min. The medium velocity of cause directly impacts the shear stress applied to the cells in the pore area. If cells would be used in this setup that require certain shear stress for proper differentiation, like endothelial cells, it should be adapted accordingly. However, during preliminary tests, tissues got destroyed, ripped apart, or simply dissolved in settings with medium velocities of 3 ml/min or higher. Since this work did not focus on shear stress application to the cells, a rather low medium velocity of 1.5 ml/min was chosen. It is recommended testing a bioink carefully for their integrity prior to usage in dynamic settings.

After this analysis, Flower1, Flower 5, and Column could be successfully test-printed using Cellink® Bioink and Alginate-POx bionk as proof of concept. A perfect alignment of the printed tissue and the pores with the pores of the container was shown here also. According to these results, the Flower5 shape was used for further biological experiments. This shape shows the most complex properties in terms of shape within the set of tissues and has multiple pores to ensure a sufficient glucose concentration inside the tissue of at least 12 mol/m^3. Therefore, this shape was chosen for bioprinting with cells.

5.5 Dynamic Perfused Tissue Culture

Constructs were generated using Alginate-POx bioink and Cellink® Bioink, containing C2C12 cells by a ratio of 10 mio cells/ml. Monitoring of the medium during cell culture, which was obtained by non-invasive analysis, was performed for two reasons: First, glucose and lactate levels gave rough insight of the cell growth and expansion in the tissue and helped to estimate the time for next medium exchange. If the lactate levels would not correlate negatively with the glucose levels, a contamination could have been identified. Second, LDH levels show a rough hint for cell death and cell-contentment.

In this case, glucose and lactate levels developed as expected during the tissue culture. Considered, that the medium exchange was performed irregularly every 4th or 5th day, glucose consumption raised, as did the lactate levels. At first medium exchange, a relative high amount of LDH was detected in all constructs. This finding correlates with results from preliminary experiments. It can be assumed, that this is caused by cell death during bioink mixing and bioprinting processes. Additionally, there is a certain delay from starting perfusion until the medium reaches the inner parts of the construct. It can be assumed, that those reasons lead to a relatively high cell death and LDH level at the beginning.

14 days of dynamic culture did not show any impact to the tissue stability, regardless of which ink was used. It is assumed, that the relative low flow rate and the crosslinking prevented the constructs from significant shrinkage. The pores of the constructs showed unchanged alignment with the pores of the tissue container, as it did after printing.

Also, constructs made from both inks showed cells spread throughout the entire tissue. This is an important result since it proofs a sufficient nutrition of all areas inside the construct. Differences could be identified between the inner tissue parts and areas near to the pores: In both inks, cells formed aggregates close to the pores and the area around them. This is an expected result, as the pores are the source of the nutrients. Dead cells were also visualized in the tissue, indicating a competition for nutrients. Further implementation of capillaries or similar could solve this, and lead to a deportation of waste. In the inner parts of the constructs the distribution of cells is more heterogeneous and indicates the nozzle path during printing. Reasons for this could be stiffness gradients generated during crosslinking due to the layered structure of the construct [138–140], or different shear forces inside the nozzle of the printer during the printing process [141, 142]. Both reasons need further investigations for clarification. By visual comparation of both constructs, both inks show a successful dynamic culture of cell-containing bioprinted constructs.

As previously described in the aim of the work, tissue maturation has a crucial impact on successful tissue production. To demonstrate that the reactor can support this and maintain its functionality during cell differentation into a functional tissue, adipose differentiation of hMSCs was performed as a representative example. To do so, constructs were printed by using Cellink® Bioink mixed with 2 mio primary hMSCs per ml. Directly after printing the medium was switched from expansion medium to adipose differentiation medium. After 21 days of dynamic culture with weekly medium exchange, the construct showed the same stability as it did within the C2C12-experiments: The pores of the tissue aligned perfectly with the pores of the tissue container and no shrinkage could been identified macroscopically. Also, visualization showed cells spread throughout the entire construct, as it did before. In contrast to the C2C12 construct, no aggregation of cells could be found at the pores. Instead, the cells are distributed equally, although the printing pathway is also identifiable here by cell distribution. Magnification of the anatomical staining showed successful initiated differentiation of the hMSCs by formation of vacuolic structures, that can be referred to as fat vacuoles. Even though the number of cells is rather low, this results proof the possibility for differentiation within the developed bioreactor system.

5.6 Adaption to Combined Printing

Due to technical limitations, the process in this work was mainly based on sequential printing, with having the container and tissue printed separately. After proof of concept of the functionality of the bioreactor, the tissue container was adapted for combined printing. During this process the results showed, that the most crucial limitations are the technological capabilities of the available printers: Most importantly this includes the possibility for having a thermoplastic printing unit installed to the bioprinter or vice versa. There are several devices at the market that allow such an inclusion, but also are extremely pricy. Unfortunately, there was none of those printers available for this work, except of one that only allowed for very small amounts of thermoplastic material to be printed.

Despite the technological hardware issue, the printing time and volume had to be drastically reduced anyway for a combined printing approach. Extended printing times would result in the cells to sink down within the bioink while waiting for the container to be printed, ending up with inhomogeneous distribution of cells when printing the tissue part. As a result, the shape of the tissue container was reduced as far as possible in height, ending up with a volume change from 7.4 ml to 1.2 ml, and a respective printing time reduction from 41 min to 10 min for the tissue container. The missing height of the container was compensated by a so-called spacer part, which can be preprinted and stored until usage. The poof of concept for combined printing was shown by Susanne Heid using a smaller squared tissue shape rather than the Flower5 shape due to the technical limitations. All in all, we could proof the functionality of the combined printing process. For printing the Flower5 shape and tissue container, the minimal hardware requirements are a hydrogel extrusion printhead with at least 2 ml extrusion volume and a thermoplastic printhead with an extrusion volume of at least 4 ml.

When comparing the two printing processes, sequential and combined, the pros and cons must be weighed carefully for the reasons mentioned above. During the work with the sequential process, it became clear that it can be advantageous to perform the printing steps in an individual, specialized, and optimized device each. Additionally, at current market prices, splitting the process between two devices is much more resource-efficient. It also offers more flexible planning of the process and an interim evaluation of the quality of the printed container. As already described, combined printing in contrast offers a higher degree of automation and thus increases standardization and reduces the hurdles for widespread use in the clinics. A reduction in manual intervention also significantly reduces the risk of contamination, which is particularly relevant in clinical applications. In conclusion, sequential printing is recommended mainly for research purposes, while combined printing brings advantages for clinical use.

5.7 Automation Solution for Bioreactor Platform

For further standardization of the dynamic culture process, which would support bench to bed translation, automation solutions were aimed to reduce manual intervention during tissue maturation. A list of requirements was derived for this purpose, addressing medium exchange, pump speed, mobile usage and handlebility. Medium exchange was focused as it is the most crucial and repeating task in dynamic cell culture. The tubing system was therefore extended by a reservoir for fresh medium and a waste compartment. To keep the required components to standard labware, the new medium reservoir was realized by a standard 10-ml-syringe and a common glass bottle with a tubing socket in the lid as a waste reservoir. Using special LUER-connectors enables the sterile attachment and detachment of them to the tubing system, even when the reactor isn't placed in the sterile cleanbench, which is reducing transferring actions. Since no temperature-control, like sensors and heating units, were implemented, the medium must be preheated manually.

To switch between the different compartments, standard low-voltage pinch valves were used. Together with a NEMA17 stepper motor attached to a peristaltic pump head is used for the dynamic medium flow. For automation of this electrical main parts, an Arduino UNO R3 microcontroller was selected as the best suitable option to this usage. The open-source Arduino platform provides a high set of electrical components, optimized for such kind of automation solutions. Arduino Hardware is standardized and captives with low costs, modular construction, and easy manipulative software development. Restrictions within this microcontroller are a limited number of pins for peripheral parts and devices, low storage memory for the firmware program, and a rather slow processing unit. Further automation of e.g. included electrical stimulation, various sensors and actuators would require a more powerful processing unit, resulting in higher costs and more complex software development.

A second major improvement of the device was enabled by equipping it with a battery pack. This way the device was fully independent operational, leading to a continuous perfusion of the tissue even during transport. An adequate charging controller, which is commonly used for controlling solar panel setups, was used to manage the switch between power supply by a wired unit and a battery, as well as charging the battery in wired-mode. In theory, the integrated battery pack can supply the device up to more then 3 h in mobile-mode. Since the device is not temperature-compensated, variations in temperature also changes the electrical resistances and workload within the device, which impacts the available time for mobile handling. Therefore, a battery charge indicator was implemented to provide visual feedback to the operator.

The housing was designed to protect the operator from the electronics and vice versa. A dust- or water-proof sealing was not realized or evaluated for it. Standards for tightness of electrical devices and protection levels etc. are defined and clearly stated in various DIN norms and can therefore tested for the device individually if required. Since the panels of the housing were 3D-printed, the manufacturing costs were reduced and the weight was lowered to less than 5 kg, making it easy to repair and handling in the lab. The size of the device was adapted to fit to a running clean bench while a bioreactor is attached to it, which enables transfer and operation of the bioreactor in a sterile environment, beneficial for conducting experiments during tissue maturation.

Human machine interface is further complemented by a LCD screen, showing the current status of the medium exchange and the pump speed, providing a minimalistic feedback to the operator. Also, the implementation of a push- and a rotary-button was realized with the microcontroller, reducing the efforts for medium exchange to manually preheating, attaching the new medium and pressing a single button. The overall pump speed can be manually adjusted by the rotary-button to individual needs. With this particular tubing system, medium exchange causes the perfusion of the tissue to stop for only 1 minute, which is of low impact to the nutrient supply within the tissue.

This easy-but-effective functionality of the so-called docking station enables for an economical solution to significantly increase handleability in the lab, but also for non-expert staff in the clinics.

Within this work the efforts of a manufacturing process of perfusable 3D-printed bioreactors holding bioprinted tissues was significantly reduced to some single-button solutions. The developed bioreactor platform enables fast and easy adaption for various shapes, inks, and tissues. A major benefit in this work shows the increase of the handleability of such complex approaches for non-experts in the clinics. The results and findings are a great step towards translation of patient-specific research in Regenerative Medicine to actual clinical use.

6 Conclusion and Outlook

The aim of this work was to synergize conventional 3D printing and bioprinting methods to develop a high shape fidelity and perfusable bioreactor system. The high degrees of freedom offered by these techniques are optimally utilized for the patient-specific production of engineered tissue and enhance bench to bed translation by automation solutions.

To do so, in a first objective a common basis for 3D printing was developed and fitted into a guideline for device- and material-assessment, tailored for bioreactor development in Life Sciences. Quantifiable printer rating and comparison was enabled by the development of test bodies representing most relevant parameters for bioreactor geometries. Broad material analysis was implemented to the guidance, as well as a semi-automated process using ImageJ macros for shape evaluation. Using this guidance, design criteria, like tolerances and geometrical limitations, were figured and a 3D-printed perfusion bioreactor was developed. Most important, the shape fidelity, provided by 3D printing, was kept during the developmental process in order to achieve flexible adaption to patient-specific wound geometry. Meaning, that a standard reactor setup was derived, capable of holding a variety of tissue shapes.

Perfusion was a second major requirement, which was realized by vertical pore structures in the tissue container and the tissues. For Gcode fitting, commercially available bioink alternatives like NIVEA® lotion and Cellink® Start were used to provide a sustainable and low-cost-way for bioprinting research approaches. As shown successfully, those alternatives are well suited to replace costly and resource-demanding bioinks during geometrical trial-and-error studies. Further, resources were reduced by implementing CFD simulations, forecasting shear stress and nutrient concentration according to the pore layout within the tissues in a pre-experimental setting.

Subsequently, the biological functionality of the bioreactor was demonstrated by using easy-to-culture and cheaply available C2C12 cellline to analyze cell survival and basic behavior of the printed tissue during dynamic culture. A sequential printing process was chosen for this, were container and tissue are printed in two distinct steps. Successful cell culture could be performed with two completely different bioinks, self-made alginate-based Alginate-POx bioink and commercially available nanocellulose-based Cellink® Bioink, demonstrating the adaptability and flexibility of the developed system. To demonstrate the possibility of tissue maturation, primary hMSCs were used together with the commercial Cellink® Bioink and printed into the reactor. By using the according medium composition, the cells in the printed tissue were successfully initiated for adipose differentiation during dynamic culture.

In successfully adapting the reactor from a sequential approach to a combined printed process, the advantages and disadvantages of each process became clear. Since simultaneous printing has significantly higher demands on the technological printer hardware, this process is more suitable for clinical applications where less trained personnel and higher sterility standards prevail. Sequential printing, on the other hand, is particularly suitable for research purposes, as the separate manufacturing processes allow an intermediate evaluation of the container.
For a final objective, the standardization of the developed bioreactor system was significantly increased by partially automating the regular media exchange. For this purpose, a mobile device, based on an Arduino-microcontroller, was developed for the bioreactor system. Bench to bed translation of the system was promoted by increased standardization and improved handling.

In a next step, the clinical steps of 3D scanning and wound defect assessment, which have not been considered so far, could be implemented. For this purpose, a 3-dimensional defect geometry must be determined and correctly converted into a CAD-file. The required technical hardware and software for such a process are already available and must be integrated into the overall process accordingly. Furthermore, tissues with higher hierarchical complexity and functionality have to be realized in the reactor system. Since this work has already been carried out with myoblast celllines and adipose differentiation, functional muscle and fat tissue are particularly suitable for the next steps. Also, especially because larger external wounds usually represents defects in fat and muscle tissues. Together with artificial skin constructs which are already available, these three tissues form a solid basis for initiating clinical translation. Additionally, it would be a great step in biofabrication to manufacture internal organs in the same way in the reactor system. A more complex tissue maturation can be achieved step by step by implementing the unmet open points of the docking station requirements list. For example, additional electrical and mechanical stimuli may contribute to the development of muscle tissue. Improved monitoring of reactor internal parameters such as e.g. pH, temperature, and media composition would support higher control and standardizability of the dynamic culture of such tissues.

7 Bibliography

[1] R. Langer and J. P. Vacanti. "Tissue engineering." In: *Science (New York, N.Y.)* 260.5110 (1993), pp. 920–926. ISSN: 0036-8075. DOI: `10.1126/science.8493529`.

[2] Florian Groeber et al. "Skin tissue engineering–in vivo and in vitro applications." In: *Advanced drug delivery reviews* 63.4-5 (2011), pp. 352–366. DOI: `10.1016/j.addr.2011.01.005`.

[3] Robert P. Lanza et al., eds. *Principles of tissue engineering*. 5th edition. London, San Diego, and Cambridge: Elsevier Academic Press, 2020. ISBN: 978-0-12-818422-6. URL: `https://www.sciencedirect.com/science/book/9780128184226`.

[4] Rob B. M. de Vries et al. "Reducing the number of laboratory animals used in tissue engineering research by restricting the variety of animal models. Articular cartilage tissue engineering as a case study." In: *Tissue engineering. Part B, Reviews* 18.6 (2012), pp. 427–435. DOI: `10.1089/ten.TEB.2012.0059`.

[5] Rainer Radtke. *Anzahl der für wissenschaftliche Versuche verwendeten Tiere in Deutschland von 2000 bis 2019*. Ed. by Statista GmbH. 2020. URL: `https://de.statista.com/statistik/daten/studie/205736/umfrage/anzahl-der-fuer-tierversuche-verwendeten-tiere-seit-2000/#professional`.

[6] Patricia Waage et al. *DSO - Jahresbericht Organspende und Transplantation in Deutschland 2020*. 2021. ISBN: ISBN 978-3-943384-24-6. URL: `https://dso.de/SiteCollectionDocuments/DSO-Jahresbericht%202020.pdf`.

[7] Maya Horst et al. "Tissue Engineering in Pediatric Bladder Reconstruction-The Road to Success." In: *Frontiers in pediatrics* 7 (2019), p. 91. ISSN: 2296-2360. DOI: `10.3389/fped.2019.00091`.

[8] Anthony Atala et al. "Tissue-engineered autologous bladders for patients needing cystoplasty." In: *The Lancet* 367.9518 (2006), pp. 1241–1246. ISSN: 01406736. DOI: `10.1016/S0140-6736(06)68438-9`.

[9] Sara Bouhout, Stéphane Chabaud, and Stéphane Bolduc. "Collagen hollow structure for bladder tissue engineering." In: *Materials science & engineering. C, Materials for biological applications* 102 (2019), pp. 228–237. DOI: `10.1016/j.msec.2019.04.052`.

[10] Martin J. Elliott et al. "Stem-cell-based, tissue engineered tracheal replacement in a child: a 2-year follow-up study." In: *The Lancet* 380.9846 (2012), pp. 994–1000. ISSN: 01406736. DOI: `10.1016/S0140-6736(12)60737-5`.

[11] Daisuke Taniguchi et al. "Scaffold-free trachea regeneration by tissue engineering with bio-3D printing." In: *Interactive cardiovascular and thoracic surgery* 26.5 (2018), pp. 745–752. DOI: `10.1093/icvts/ivx444`.

[12] Jeong Hun Park et al. "A rational tissue engineering strategy based on three-dimensional (3D) printing for extensive circumferential tracheal reconstruction." In: *Biomaterials* 185 (2018), pp. 276–283. DOI: `10.1016/j.biomaterials.2018.09.031`.

[13] Antje Kremer et al. "Three-Dimensional Coculture of Meniscal Cells and Mesenchymal Stem Cells in Collagen Type I Hydrogel on a Small Intestinal Matrix-A Pilot Study Toward Equine Meniscus Tissue Engineering." In: *Tissue engineering. Part A* 23.9-10 (2017), pp. 390–402. DOI: `10.1089/ten.TEA.2016.0317`.

[14] Jang Hwan Min et al. "The use of matriderm and autologous skin graft in the treatment of full thickness skin defects." In: *Archives of plastic surgery* 41.4 (2014), pp. 330–336. ISSN: 2234-6163. DOI: `10.5999/aps.2014.41.4.330`.

[15] Charles E. Hart, Andrea Loewen-Rodriguez, and Jan Lessem. "Dermagraft: Use in the Treatment of Chronic Wounds." In: *Advances in wound care* 1.3 (2012), pp. 138–141. ISSN: 2162-1918. DOI: `10.1089/wound.2011.0282`.

[16] T. Shin'oka, Y. Imai, and Y. Ikada. "Transplantation of a tissue-engineered pulmonary artery." In: *The New England journal of medicine* 344.7 (2001), pp. 532–533. ISSN: 0028-4793. DOI: `10.1056/NEJM200102153440717`.

[17] Matthew W. Ellis, Jiesi Luo, and Yibing Qyang. "Modeling elastin-associated vasculopathy with patient induced pluripotent stem cells and tissue engineering." In: *Cellular and molecular life sciences : CMLS* 76.5 (2019), pp. 893–901. DOI: `10.1007/s00018-018-2969-7`.

[18] Sin-Guang Chen et al. "Vascular Tissue Engineering: Advanced Techniques and Gene Editing in Stem Cells for Graft Generation." In: *Tissue engineering. Part B, Reviews* 27.1 (2021), pp. 14–28. DOI: `10.1089/ten.TEB.2019.0264`.

[19] Fergal J. O'Brien. "Biomaterials & scaffolds for tissue engineering." In: *Materials Today* 14.3 (2011), pp. 88–95. ISSN: 13697021. DOI: `10.1016/S1369-7021(11)70058-X`.

[20] B. P. Chan and K. W. Leong. "Scaffolding in tissue engineering: general approaches and tissue-specific considerations." In: *European spine journal : official publication of the European Spine Society, the European Spinal Deformity Society, and the European Section of the Cervical Spine Research Society* 17 Suppl 4 (2008), pp. 467–479. DOI: `10.1007/s00586-008-0745-3`.

[21] Ashkan Shafiee and Anthony Atala. "Tissue Engineering: Toward a New Era of Medicine." In: *Annual review of medicine* 68 (2017), pp. 29–40. DOI: `10.1146/annurev-med-102715-092331`.

[22] Jie Zhang et al. "Dental Follicle Stem Cells: Tissue Engineering and Immunomodulation." In: *Stem cells and development* 28.15 (2019), pp. 986–994. DOI: `10.1089/scd.2019.0012`.

[23] A. Polymeri, W. V. Giannobile, and D. Kaigler. "Bone Marrow Stromal Stem Cells in Tissue Engineering and Regenerative Medicine." In: *Hormone and metabolic research = Hormon- und Stoffwechselforschung = Hormones et metabolisme* 48.11 (2016), pp. 700–713. DOI: `10.1055/s-0042-118458`.

[24] Ronghua Yang et al. "Progress in studies of epidermal stem cells and their application in skin tissue engineering." In: *Stem cell research & therapy* 11.1 (2020), p. 303. DOI: `10.1186/s13287-020-01796-3`.

[25] Julie R. Fuchs, Boris A. Nasseri, and Joseph P. Vacanti. "Tissue engineering: a 21st century solution to surgical reconstruction." In: *The Annals of Thoracic Surgery* 72.2 (2001), pp. 577–591. ISSN: 00034975. DOI: `10.1016/s0003-4975(01)02820-x`.

[26] Francesco Rosso et al. "From cell-ECM interactions to tissue engineering." In: *Journal of Cellular Physiology* 199.2 (2004), pp. 174–180. ISSN: 1097-4652. DOI: `10.1002/jcp.10471`.

[27] Mina J. Bissell, H.Glenn Hall, and Gordon Parry. "How does the extracellular matrix direct gene expression?" In: *Journal of Theoretical Biology* 99.1 (1982), pp. 31–68. ISSN: 00225193. DOI: `10.1016/0022-5193(82)90388-5`.

[28] Celeste M. Nelson and Mina J. Bissell. "Of extracellular matrix, scaffolds, and signaling: tissue architecture regulates development, homeostasis, and cancer." In: *Annual review of cell and developmental biology* 22 (2006), pp. 287–309. ISSN: 1081-0706. DOI: `10.1146/annurev.cellbio.22.010305.104315`.

[29] François Berthiaume, Timothy J. Maguire, and Martin L. Yarmush. "Tissue engineering and regenerative medicine: history, progress, and challenges." In: *Annual review of chemical and biomolecular engineering* 2 (2011), pp. 403–430. ISSN: 1947-5438. DOI: `10.1146/annurev-chembioeng-061010-114257`.

[30] Mahtab Asadian et al. "Fabrication and Plasma Modification of Nanofibrous Tissue Engineering Scaffolds." In: *Nanomaterials (Basel, Switzerland)* 10.1 (2020), p. 119. ISSN: 2079-4991. DOI: `10.3390/nano10010119`.

[31] Brahatheeswaran Dhandayuthapani et al. "Polymeric Scaffolds in Tissue Engineering Application: A Review." In: *International Journal of Polymer Science* 2011 (2011), pp. 1–19. ISSN: 1687-9422. DOI: `10.1155/2011/290602`.

[32] Annunziata Crupi et al. "Inflammation in tissue engineering: The Janus between engraftment and rejection." In: *European journal of immunology* 45.12 (2015), pp. 3222–3236. DOI: `10.1002/eji.201545818`.

[33] Stephen F. Badylak and Thomas W. Gilbert. "Immune response to biologic scaffold materials." In: *Seminars in immunology* 20.2 (2008), pp. 109–116. ISSN: 1044-5323. DOI: `10.1016/j.smim.2007.11.003`.

[34] L. E. Freed et al. "Biodegradable polymer scaffolds for tissue engineering." In: *Bio/technology (Nature Publishing Company)* 12.7 (1994), pp. 689–693. ISSN: 0733-222X. DOI: `10.1038/nbt0794-689`.

[35] Jun Yin et al. "3D Bioprinting of Low-Concentration Cell-Laden Gelatin Methacrylate (GelMA) Bioinks with a Two-Step Cross-linking Strategy." In: *ACS applied materials & interfaces* 10.8 (2018), pp. 6849–6857. DOI: `10.1021/acsami.7b16059`.

[36] Thomas Distler et al. "3D printed oxidized alginate-gelatin bioink provides guidance for C2C12 muscle precursor cell orientation and differentiation via shear stress during bioprinting." In: *Biofabrication* 12.4 (2020), p. 045005. DOI: `10.1088/1758-5090/ab98e4`.

[37] Ingeborg Elisabeth Carlström et al. "Cross-linked gelatin-nanocellulose scaffolds for bone tissue engineering." In: *Materials Letters* 264 (2020), p. 127326. ISSN: 0167577X. DOI: `10.1016/j.matlet.2020.127326`.

[38] Tobias Kuhnt and Sandra Camarero-Espinosa. "Additive manufacturing of nanocellulose based scaffolds for tissue engineering: Beyond a reinforcement filler." In: *Carbohydrate polymers* 252 (2021), p. 117159. DOI: `10.1016/j.carbpol.2020.117159`.

[39] Filipe V. Ferreira et al. "Porous nanocellulose gels and foams: Breakthrough status in the development of scaffolds for tissue engineering." In: *Materials Today* 37 (2020), pp. 126–141. ISSN: 13697021. DOI: `10.1016/j.mattod.2020.03.003`.

[40] Huize Luo et al. "Advances in tissue engineering of nanocellulose-based scaffolds: A review." In: *Carbohydrate polymers* 224 (2019), p. 115144. DOI: `10.1016/j.carbpol.2019.115144`.

[41] Elsa C. Chan et al. "Three Dimensional Collagen Scaffold Promotes Intrinsic Vascularisation for Tissue Engineering Applications." In: *PloS one* 11.2 (2016), e0149799. DOI: `10.1371/journal.pone.0149799`.

[42] Chanjuan Dong and Yonggang Lv. "Application of Collagen Scaffold in Tissue Engineering: Recent Advances and New Perspectives." In: *Polymers* 8.2 (2016). DOI: `10.3390/polym8020042`.

[43] Julie Glowacki and Shuichi Mizuno. "Collagen scaffolds for tissue engineering." In: *Biopolymers* 89.5 (2008), pp. 338–344. ISSN: 0006-3525. DOI: `10.1002/bip.20871`.

[44] C. Liu, Z. Xia, and J. T. Czernuszka. "Design and Development of Three-Dimensional Scaffolds for Tissue Engineering." In: *Chemical Engineering Research and Design* 85.7 (2007), pp. 1051–1064. ISSN: 02638762. DOI: `10.1205/cherd06196`.

[45] Diana Lim et al. "Bioreactor design and validation for manufacturing strategies in tissue engineering." In: *Bio-Design and Manufacturing* (2021). ISSN: 2096-5524. DOI: `10.1007/s42242-021-00154-3`.

[46] Christoph Meinert et al. "A novel bioreactor system for biaxial mechanical loading enhances the properties of tissue-engineered human cartilage." In: *Scientific reports* 7.1 (2017), p. 16997. DOI: `10.1038/s41598-017-16523-x`.

[47] Shigang Lin and Kibret Mequanint. "Bioreactor-induced mesenchymal progenitor cell differentiation and elastic fiber assembly in engineered vascular tissues." In: *Acta biomaterialia* 59 (2017), pp. 200–209. DOI: `10.1016/j.actbio.2017.07.012`.

[48] J. Rosser and D. J. Thomas. "Bioreactor processes for maturation of 3D bioprinted tissue." In: *3D Bioprinting for Reconstructive Surgery*. Ed. by Daniel Thomas, Zita M. Jessop, and Iain S. Whitaker. Woodhead Publishing Series in Biomaterials Ser. Kent: Elsevier Science, 2017, pp. 191–215. ISBN: 9780081011034. DOI: `10.1016/B978-0-08-101103-4.00010-7`.

[49] Sarah Miho van Belleghem et al. "Overview of Tissue Engineering Concepts and Applications." In: *Biomaterials science*. Ed. by William R. Wagner et al. London et al.: Academic Press, 2020, pp. 1289–1316. ISBN: 9780128161371. DOI: `10.1016/B978-0-12-816137-1.00081-7`.

[50] Norbert Ferencik et al. "Overview Article: Bioreactors Designed for 3D Bioprinted Tissue and Process Parameters." In: *SAMI 2021*. Piscataway, NJ: IEEE, 2021, pp. 000131–000134. ISBN: 978-1-7281-8053-3. DOI: `10.1109/SAMI50585.2021.9378697`.

[51] Alice Pasini et al. "Medium Perfusion Flow Improves Osteogenic Commitment of Human Stromal Cells." In: *Stem cells international* 2019 (2019), p. 1304194. ISSN: 1687-966X. DOI: `10.1155/2019/1304194`.

[52] Jackson G. DeStefano et al. "Effect of shear stress on iPSC-derived human brain microvascular endothelial cells (dhBMECs)." In: *Fluids and barriers of the CNS* 14.1 (2017), p. 20. DOI: `10.1186/s12987-017-0068-z`.

[53] D. A. Chistiakov, A. N. Orekhov, and Y. V. Bobryshev. "Effects of shear stress on endothelial cells: go with the flow." In: *Acta physiologica (Oxford, England)* 219.2 (2017), pp. 382–408. DOI: `10.1111/apha.12725`.

[54] Joyce Bischoff. "Endothelial-to-Mesenchymal Transition." In: *Circulation research* 124.8 (2019), pp. 1163–1165. DOI: `10.1161/CIRCRESAHA.119.314813`.

[55] Ehrhardt Proksch. "pH in nature, humans and skin." In: *The Journal of dermatology* 45.9 (2018), pp. 1044–1052. DOI: `10.1111/1346-8138.14489`.

[56] Jan Hansmann et al. "Bioreactors in tissue engineering - principles, applications and commercial constraints." In: *Biotechnology journal* 8.3 (2013), pp. 298–307. DOI: `10.1002/biot.201200162`.

[57] Junjie Zhao et al. "Bioreactors for tissue engineering: An update." In: *Biochemical Engineering Journal* 109 (2016), pp. 268–281. ISSN: 1369703X. DOI: `10.1016/j.bej.2016.01.018`.

[58] Stephen T. Newman et al. "Process planning for additive and subtractive manufacturing technologies." In: *CIRP Annals* 64.1 (2015), pp. 467–470. ISSN: 00078506. DOI: `10.1016/j.cirp.2015.04.109`.

[59] J. K. Watson and K. M. B. Taminger. "A decision-support model for selecting additive manufacturing versus subtractive manufacturing based on energy consumption." In: *Journal of cleaner production* 176 (2015), pp. 1316–1322. ISSN: 0959-6526. DOI: `10.1016/j.jclepro.2015.12.009`.

[60] Henri Paris et al. "Comparative environmental impacts of additive and subtractive manufacturing technologies." In: *CIRP Annals* 65.1 (2016), pp. 29–32. ISSN: 00078506. DOI: `10.1016/j.cirp.2016.04.036`.

[61] Amanda Su and Subhi J. Al'Aref. "History of 3D Printing." In: *3D printing applications in cardiovascular medicine*. Ed. by James Min et al. London and San Diego: Academic Press, 2018, pp. 1–10. ISBN: 9780128039175. DOI: `10.1016/B978-0-12-803917-5.00001-8`.

[62] Joan Horvath. "A Brief History of 3D Printing." In: *Mastering 3D printing*. Ed. by Joan Horvath. Technology in action. New York, NY: Apress / Springer, 2014, pp. 3–10. ISBN: 978-1-4842-0026-1. DOI: `10.1007/978-1-4842-0025-4{\textunderscore}1`.

[63] Matthew Whitaker. "The history of 3D printing in healthcare." In: *The Bulletin of the Royal College of Surgeons of England* 96.7 (2014), pp. 228–229. ISSN: 1473-6357. DOI: `10.1308/147363514X13990346756481`.

[64] Barry Berman. "3-D printing: The new industrial revolution." In: *Business Horizons* 55.2 (2012), pp. 155–162. ISSN: 00076813. DOI: `10.1016/j.bushor.2011.11.003`.

[65] *DIN EN ISO/ASTM 52900:2018-06, Additive Fertigung_- Grundlagen_- Terminologie (ISO/ASTM DIS_52900:2018); Deutsche und Englische Fassung prEN_ISO/ASTM 52900:2018*. Berlin. DOI: `10.31030/2842544`.

[66] Jahan Zeb Gul et al. "3D printing for soft robotics - a review." In: *Science and technology of advanced materials* 19.1 (2018), pp. 243–262. ISSN: 1468-6996. DOI: `10.1080/14686996.2018.1431862`.

[67] Marius Gensler et al. "3D printing of bioreactors in tissue engineering: A generalised approach." In: *PloS one* 15.11 (2020), e0242615. DOI: `10.1371/journal.pone.0242615`.

[68] Jakub Bryła and Adam Martowicz. "Study on the Importance of a Slicer Selection for the 3D Printing Process Parameters via the Investigation of G-Code Readings." In: *Machines* 9.8 (2021), p. 163. DOI: `10.3390/machines9080163`.

[69] Andrew Gleadall. "FullControl GCode Designer: Open-source software for unconstrained design in additive manufacturing." In: *Additive Manufacturing* 46 (2021), p. 102109. ISSN: 22148604. DOI: `10.1016/j.addma.2021.102109`.

[70] Yuenyong Nilsiam, Paul Sanders, and Joshua M. Pearce. "Slicer and process improvements for open-source GMAW-based metal 3-D printing." In: *Additive Manufacturing* 18 (2017), pp. 110–120. ISSN: 22148604. DOI: `10.1016/j.addma.2017.10.007`.

[71] Marton Gulyas et al. "Software tools for cell culture-related 3D printed structures." In: *PloS one* 13.9 (2018), e0203203. DOI: `10.1371/journal.pone.0203203`.

[72] Balasankar Meera Priyadarshini, Vishwesh Dikshit, and Yi Zhang. "3D-printed Bioreactors for In Vitro Modeling and Analysis." In: *International journal of bioprinting* 6.4 (2020), p. 267. DOI: `10.18063/ijb.v6i4.267`.

[73] Lester J. Smith et al. "FABRICA: A Bioreactor Platform for Printing, Perfusing, Observing, & Stimulating 3D Tissues." In: *Scientific reports* 8.1 (2018), p. 7561. DOI: `10.1038/s41598-018-25663-7`.

[74] Abigail R. Raveling, Sophia K. Theodossiou, and Nathan R. Schiele. "A 3D printed mechanical bioreactor for investigating mechanobiology and soft tissue mechanics." In: *MethodsX* 5 (2018), pp. 924–932. ISSN: 2215-0161. DOI: `10.1016/j.mex.2018.08.001`.

[75] Edgar Peris et al. "Tuneable 3D printed bioreactors for transaminations under continuous-flow." In: *Green Chemistry* 19.22 (2017), pp. 5345–5349. ISSN: 1463-9262. DOI: `10.1039/C7GC02421E`.

[76] Adam J. Janvier, Elizabeth Canty-Laird, and James R. Henstock. "A universal multi-platform 3D printed bioreactor chamber for tendon tissue engineering." In: *Journal of tissue engineering* 11 (2020), p. 2041731420942462. ISSN: 2041-7314. DOI: `10.1177/2041731420942462`.

[77] Jürgen Groll et al. "Biofabrication: reappraising the definition of an evolving field." In: *Biofabrication* 8.1 (2016), p. 013001. DOI: `10.1088/1758-5090/8/1/013001`.

[78] Jia Min Lee et al. "3D bioprinting processes: A perspective on classification and terminology." In: *International journal of bioprinting* 4.2 (2018), p. 151. DOI: `10.18063/IJB.v4i2.151`.

[79] Wei Sun et al. "The bioprinting roadmap." In: *Biofabrication* 12.2 (2020), p. 022002. DOI: `10.1088/1758-5090/ab5158`.

[80] Ibrahim Tarik Ozbolat. *3D bioprinting: Fundamentals, principles and applications*. London, United Kingdom: Academic Press, 2017. ISBN: 9780128030301.

[81] Bon Kang Gu et al. "3-dimensional bioprinting for tissue engineering applications." In: *Biomaterials research* 20 (2016), p. 12. ISSN: 1226-4601. DOI: `10.1186/s40824-016-0058-2`.

[82] Young-Joon Seol et al. "Bioprinting technology and its applications." In: *European journal of cardio-thoracic surgery : official journal of the European Association for Cardio-thoracic Surgery* 46.3 (2014), pp. 342–348. DOI: `10.1093/ejcts/ezu148`.

[83] J. Groll et al. "A definition of bioinks and their distinction from biomaterial inks." In: *Biofabrication* 11.1 (2018), p. 013001. DOI: `10.1088/1758-5090/aaec52`.

[84] Mario Chopin-Doroteo, Edna Ayerim Mandujano-Tinoco, and Edgar Krötzsch. "Tailoring of the rheological properties of bioinks to improve bioprinting and bioassembly for tissue replacement." In: *Biochimica et biophysica acta. General subjects* 1865.2 (2021), p. 129782. DOI: `10.1016/j.bbagen.2020.129782`.

[85] Teng Gao et al. "Optimization of gelatin-alginate composite bioink printability using rheological parameters: a systematic approach." In: *Biofabrication* 10.3 (2018), p. 034106. DOI: `10.1088/1758-5090/aacdc7`.

[86] Naomi Paxton et al. "Proposal to assess printability of bioinks for extrusion-based bioprinting and evaluation of rheological properties governing bioprintability." In: *Biofabrication* 9.4 (2017), p. 044107. DOI: `10.1088/1758-5090/aa8dd8`.

[87] Haley M. Butler et al. "Investigation of rheology, printability, and biocompatibility of N,O-carboxymethyl chitosan and agarose bioinks for 3D bioprinting of neuron cells." In: *Materialia* 18 (2021), p. 101169. ISSN: 25891529. DOI: `10.1016/j.mtla.2021.101169`.

[88] Andrea S. Theus et al. "Bioprintability: Physiomechanical and Biological Requirements of Materials for 3D Bioprinting Processes." In: *Polymers* 12.10 (2020). DOI: `10.3390/polym12102262`.

[89] J. Carlos Gómez-Blanco et al. "Bioink Temperature Influence on Shear Stress, Pressure and Velocity Using Computational Simulation." In: *Processes* 8.7 (2020), p. 865. DOI: `10.3390/pr8070865`.

[90] Francis L. C. Morgan, Lorenzo Moroni, and Matthew B. Baker. "Dynamic Bioinks to Advance Bioprinting." In: *Advanced healthcare materials* 9.15 (2020), e1901798. DOI: `10.1002/adhm.201901798`.

[91] Karen Dubbin, Anthony Tabet, and Sarah C. Heilshorn. "Quantitative criteria to benchmark new and existing bio-inks for cell compatibility." In: *Biofabrication* 9.4 (2017), p. 044102. DOI: `10.1088/1758-5090/aa869f`.

[92] Guy Decante et al. "Engineering bioinks for 3D bioprinting." In: *Biofabrication* 13.3 (2021). DOI: `10.1088/1758-5090/abec2c`.

[93] Deepak Choudhury, Shivesh Anand, and May Win Naing. "The arrival of commercial bioprinters - Towards 3D bioprinting revolution!" In: *International journal of bioprinting* 4.2 (2018), p. 139. DOI: `10.18063/IJB.v4i2.139`.

[94] P. Selcan Gungor-Ozkerim et al. "Bioinks for 3D bioprinting: an overview." In: *Biomaterials science* 6.5 (2018), pp. 915–946. DOI: `10.1039/c7bm00765e`.

[95] A. Ribeiro et al. "Assessing bioink shape fidelity to aid material development in 3D bioprinting." In: *Biofabrication* 10.1 (2017), p. 014102. DOI: `10.1088/1758-5090/aa90e2`.

[96] E. Abelardo. "Synthetic material bioinks." In: *3D Bioprinting for Reconstructive Surgery*. Ed. by Daniel Thomas, Zita M. Jessop, and Iain S. Whitaker. Woodhead Publishing Series in Biomaterials Ser. Kent: Elsevier Science, 2017, pp. 137–144. ISBN: 9780081011034. DOI: `10.1016/B978-0-08-101103-4.00009-0`.

[97] Jessica Nulty et al. "3D bioprinting of prevascularised implants for the repair of critically-sized bone defects." In: *Acta biomaterialia* 126 (2021), pp. 154–169. DOI: `10.1016/j.actbio.2021.03.003`.

[98] Nazzar Tellisi et al. "Three Dimensional Printed Bone Implants in the Clinic." In: *The Journal of craniofacial surgery* 29.8 (2018), pp. 2363–2367. DOI: `10.1097/SCS.0000000000004829`.

[99] Fiona E. Freeman, Ross Burdis, and Daniel J. Kelly. "Printing New Bones: From Print-and-Implant Devices to Bioprinted Bone Organ Precursors." In: *Trends in molecular medicine* 27.7 (2021), pp. 700–711. DOI: `10.1016/j.molmed.2021.05.001`.

[100] Tyler Potyondy et al. "Recent advances in 3D bioprinting of musculoskeletal tissues." In: *Biofabrication* (2020). DOI: `10.1088/1758-5090/abc8de`.

[101] Nureddin Ashammakhi et al. "Advancing Frontiers in Bone Bioprinting." In: *Advanced healthcare materials* 8.7 (2019), e1801048. DOI: `10.1002/adhm.201801048`.

[102] Joseph Vanderburgh, Julie A. Sterling, and Scott A. Guelcher. "3D Printing of Tissue Engineered Constructs for In Vitro Modeling of Disease Progression and Drug Screening." In: *Annals of biomedical engineering* 45.1 (2017), pp. 164–179. DOI: `10.1007/s10439-016-1640-4`.

[103] Falguni Pati et al. "3D printing of cell-laden constructs for heterogeneous tissue regeneration." In: *Manufacturing Letters* 1.1 (2013), pp. 49–53. ISSN: 22138463. DOI: `10.1016/j.mfglet.2013.09.004`.

[104] Shreya Mehrotra et al. "3D Printing/Bioprinting Based Tailoring of in Vitro Tissue Models: Recent Advances and Challenges." In: *ACS Applied Bio Materials* 2.4 (2019), pp. 1385–1405. ISSN: 2576-6422. DOI: `10.1021/acsabm.9b00073`.

[105] D. C. Coleman. "Industrial Growth and Industrial Revolutions." In: *Economica* 23.89 (1956), p. 1. ISSN: 00130427. DOI: `10.2307/2551266`.

[106] Klaus Schwab and Nicholas Davis. *Die Zukunft der Vierten Industriellen Revolution: Wie wir den digitalen Wandel gestalten*. 1. Auflage. München: Deutsche Verlags-Anstalt, 2019. ISBN: 978-3-421-04840-0.

[107] Raymond E Dessy. "Computer networking: A rational approach to lab automation." In: *Analytical Chemistry* 49 (1977).

[108] Nathan Blow. "Lab automation: tales along the road to automation." In: *Nature Methods* 5.1 (2008), pp. 109–112. ISSN: 1548-7091. DOI: `10.1038/nmeth0108-109`.

[109] Elena G. Popkova, Yulia V. Ragulina, and Aleksei V. Bogoviz. "Fundamental Differences of Transition to Industry 4.0 from Previous Industrial Revolutions." In: *Industry 4.0: Industrial Revolution of the 21st Century*. Ed. by Elena G. Popkova, Yulia V. Ragulina, and Aleksei V. Bogoviz. Vol. 169. Studies in Systems, Decision and Control. Cham: Springer International Publishing, 2019, pp. 21–29. ISBN: 978-3-319-94309-1. DOI: `10.1007/978-3-319-94310-7{\textunderscore}3`.

[110] Ivo Schwedhelm et al. "Automated real-time monitoring of human pluripotent stem cell aggregation in stirred tank reactors." In: *Scientific reports* 9.1 (2019), p. 12297. DOI: `10.1038/s41598-019-48814-w`.

[111] G. Silverman. "Automation in the biomedical laboratory." In: *IEEE transactions on bio-medical engineering* 31.12 (1984), pp. 748–752. ISSN: 0018-9294. DOI: `10.1109/TBME.1984.325234`.

[112] Tim Chapman. "Lab automation and robotics: Automation on the move." In: *Nature* 421.6923 (2003), pp. 661, 663, 665–6. ISSN: 0028-0836. DOI: `10.1038/421661a`.

[113] J. Kuncova-Kallio and P. J. Kallio. "Lab automation in cultivation of adherent cells." In: *IEEE Transactions on Automation Science and Engineering* 3.2 (2006), pp. 177–186. ISSN: 1545-5955. DOI: `10.1109/TASE.2006.871482`.

[114] Nadav Noor et al. "3D Printing of Personalized Thick and Perfusable Cardiac Patches and Hearts." In: *Advanced Science* 6.11 (2019), p. 1900344. ISSN: 2198-3844. DOI: `10.1002/advs.201900344`.

[115] Reuven Edri et al. "Personalized Hydrogels for Engineering Diverse Fully Autologous Tissue Implants." In: *Advanced materials (Deerfield Beach, Fla.)* 31.1 (2019), e1803895. DOI: `10.1002/adma.201803895`.

[116] Thomas Lorson et al. "A Thermogelling Supramolecular Hydrogel with Sponge-Like Morphology as a Cytocompatible Bioink." In: *Biomacromolecules* 18.7 (2017), pp. 2161–2171. DOI: `10.1021/acs.biomac.7b00481`.

[117] Chen Hu et al. *A Thermogelling Organic-Inorganic Hybrid Hydrogel with Excellent Printability, Shape Fidelity and Cytocompatibility for 3D Bioprinting*. 2021. DOI: `10.26434/chemrxiv.14447676.v1`.

[118] Lukas Hahn et al. "From Thermogelling Hydrogels toward Functional Bioinks: Controlled Modification and Cytocompatible Crosslinking." In: *Macromolecular bioscience* 21.10 (2021), e2100122. DOI: `10.1002/mabi.202100122`.

[119] Chen Hu et al. "Improving printability of a thermoresponsive hydrogel biomaterial ink by nanoclay addition." In: *Journal of Materials Science* 56.1 (2021), pp. 691–705. ISSN: 0022-2461. DOI: `10.1007/s10853-020-05190-5`.

[120] Chen Hu et al. "Development of a 3D printable and highly stretchable ternary organic-inorganic nanocomposite hydrogel." In: *Journal of materials chemistry. B* 9.22 (2021), pp. 4535–4545. DOI: `10.1039/D1TB00484K`.

[121] Lukas Hahn et al. "An Inverse Thermogelling Bioink Based on an ABA-Type Poly(2-oxazoline) Amphiphile." In: *Biomacromolecules* 22.7 (2021), pp. 3017–3027. DOI: `10.1021/acs.biomac.1c00427`.

[122] Lukas Hahn et al. "ABA Type Amphiphiles with Poly(2–benzhydryl–2–oxazine) Moieties: Synthesis, Characterization and Inverse Thermogelation." In: *Macromolecular Chemistry and Physics* 222.17 (2021), p. 2100114. ISSN: 1022-1352. DOI: `10.1002/macp.202100114`.

[123] Lukas Hahn et al. "Inverse Thermogelation of Aqueous Triblock Copolymer Solutions into Macroporous Shear-Thinning 3D Printable Inks." In: *ACS applied materials & interfaces* 12.11 (2020), pp. 12445–12456. DOI: `10.1021/acsami.9b21282`.

[124] CELLINK. *INKREDIBLE & INKREDIBLE+^{TM} - CELLINK*. 3.05.2021. URL: `https://www.cellink.com/bioprinting/inkredible-3d-bioprinter/`.

[125] *DIN EN ISO 527-1:2012-06, Kunststoffe_- Bestimmung der Zugeigenschaften_- Teil_1: Allgemeine Grundsätze (ISO_527-1:2012); Deutsche Fassung EN_ISO_527-1:2012*. Berlin. DOI: `10.31030/1857060`.

[126] *DIN EN ISO 178:2013-09, Kunststoffe_- Bestimmung der Biegeeigenschaften (ISO_178:2010_+ Amd.1:2013); Deutsche Fassung EN_ISO_178:2010_+ A1:2013*. Berlin. DOI: 10.31030/1931347.

[127] *DIN EN ISO 10993-5:2009-10, Biologische Beurteilung von Medizinprodukten_- Teil_5: Prüfungen auf In-vitro-Zytotoxizität (ISO_10993-5:2009); Deutsche Fassung EN_ISO_10993-5:2009*. Berlin. DOI: 10.31030/1499596.

[128] Alexandre Joel Chorin. "Numerical solution of the Navier-Stokes equations." In: *Mathematics of Computation* 22.104 (1968), pp. 745–762. ISSN: 0025-5718. DOI: 10.1090/s0025-5718-1968-0242392-2.

[129] Peter Constantin and Ciprian Foiaş. *Navier-Stokes equations*. Chicago lectures in mathematics. Chicago, Ill.: Univ. of Chicago Press, 1988. ISBN: 0-226-11548-8. URL: http://www.loc.gov/catdir/enhancements/fy0609/88013122-b.html.

[130] Wilfred D. Stein and Thomas Litman. *Channels, carriers, and pumps: An introduction to membrane transport*. Second edition. Amsterdam: Elsevier, 2014. ISBN: 9780124165830.

[131] Woo Suk Ahn and Maciek R. Antoniewicz. "Metabolic flux analysis of CHO cells at growth and non-growth phases using isotopic tracers and mass spectrometry." In: *Metabolic engineering* 13.5 (2011), pp. 598–609. DOI: 10.1016/j.ymben.2011.07.002.

[132] *DIN EN ISO 14855-1:2013-04, Bestimmung der vollständigen aeroben Bioabbaubarkeit von Kunststoff-Materialien unter den Bedingungen kontrollierter Kompostierung_- Verfahren mittels Analyse des freigesetzten Kohlenstoffdioxides_- Teil_1: Allgemeines Verfahren (ISO_14855-1:2012); Deutsche Fassung EN_ISO_14855-1:2012*. Berlin. DOI: 10.31030/1939267.

[133] S. Lerouge, M. R. Wertheimer, and L'H. Yahia. "Plasma Sterilization: A Review of Parameters, Mechanisms, and Limitations." In: *Plasmas and Polymers* 6.3 (2001), pp. 175–188. ISSN: 10840184. DOI: 10.1023/A:1013196629791.

[134] I. Aguado-Maestro et al. "Are the common sterilization methods completely effective for our in-house 3D printed biomodels and surgical guides?" In: *Injury* 52.6 (2021), pp. 1341–1345. DOI: 10.1016/j.injury.2020.09.014.

[135] Kristof M. Bal et al. "Effect of plasma-induced surface charging on catalytic processes: application to CO 2 activation." In: *Plasma Sources Science and Technology* 27.2 (2018), p. 024001. DOI: 10.1088/1361-6595/aaa868.

[136] C. Hopf, W. Jacob, and A. von Keudell. "Ion-induced surface activation, chemical sputtering, and hydrogen release during plasma-assisted hydrocarbon film growth." In: *Journal of Applied Physics* 97.9 (2005), p. 094904. ISSN: 0021-8979. DOI: 10.1063/1.1883729.

[137] Navnath Kalel, Ashish Darpe, and Jayashree Bijwe. "Low pressure plasma induced surface changes of some stainless steels." In: *Surface and Coatings Technology* 425 (2021), p. 127700. ISSN: 02578972. DOI: 10.1016/j.surfcoat.2021.127700.

[138] Yufan Liu et al. "The stiffness of hydrogel-based bioink impacts mesenchymal stem cells differentiation toward sweat glands in 3D-bioprinted matrix." In: *Materials science & engineering. C, Materials for biological applications* 118 (2021), p. 111387. DOI: `10.1016/j.msec.2020.111387`.

[139] Justin R. Tse and Adam J. Engler. "Stiffness gradients mimicking in vivo tissue variation regulate mesenchymal stem cell fate." In: *PloS one* 6.1 (2011), e15978. DOI: `10.1371/journal.pone.0015978`.

[140] Tingting Xia, Wanqian Liu, and Li Yang. "A review of gradient stiffness hydrogels used in tissue engineering and regenerative medicine." In: *Journal of biomedical materials research. Part A* 105.6 (2017), pp. 1799–1812. DOI: `10.1002/jbm.a.36034`.

[141] Kalyani Nair et al. "Characterization of cell viability during bioprinting processes." In: *Biotechnology journal* 4.8 (2009), pp. 1168–1177. DOI: `10.1002/biot.200900004`.

[142] Selwa Boularaoui et al. "An overview of extrusion-based bioprinting with a focus on induced shear stress and its effect on cell viability." In: *Bioprinting* 20 (2020), e00093. ISSN: 24058866. DOI: `10.1016/j.bprint.2020.e00093`.

8 Supplementary

Code 1: ImageJ Macro XYZ

```
run("Set Scale...", "distance=444 known=1000 unit=µm global");
rename("Original");
run("Duplicate...", "title=Dublikat");
run("Line Width...", "line=5");
run("Colors...", "foreground=red background=black selection=red");
selectWindow("Dublikat");
run("8-bit");
run("Unsharp Mask...", "radius=100 mask=0.90");
setAutoThreshold("RenyiEntropy");
setThreshold(0, 70);
run("Convert to Mask");
run("Set Measurements...", "bounding redirect=None decimal=2");
run("Analyze Particles...", "size=1000-Infinity show=Outlines display
    add");
selectWindow("Dublikat");
run("Close");
selectWindow("Drawing of Dublikat");
run("Close");
selectWindow("Original");
roiManager("Select", 0);
run("Draw", "slice");
```

Code 2: ImageJ Macro Channels

```
run("Set Scale...", "distance=444 known=1000 unit=µm global");
rename("Original");
run("Duplicate...", "title=Dublikat");
run("Line Width...", "line=5");
run("Colors...", "foreground=red background=black selection=red");
selectWindow("Dublikat");
run("8-bit");
run("Unsharp Mask...", "radius=10 mask=0.90");
setAutoThreshold("RenyiEntropy dark");
setThreshold(40, 255);
setOption("BlackBackground", true);
run("Convert to Mask");
run("Set Measurements...", "area shape feret's redirect=None decimal=2"
    );
run("Analyze Particles...", "size=1000.00-Infinity circularity
    =0.20-1.00 show=Outlines display exclude add");
selectWindow("Dublikat");
run("Close");
selectWindow("Drawing of Dublikat");
run("Close");
selectWindow("Original");
roiManager("Select", 0);
run("Draw", "slice");
```

Code 3: Gcode Flower5 geometry (1 layer)

```
G21
G90
M83

G1 Z5.000 F4800.000
G1 X0.000 Y0.000

;XXXXX LAYER START XXXXX
```

```
G1 Z0.4 F4800
G1 X3.75 Y3.75
M760
G1 F600
G4 P100
G1 Y5.75 E1
G3 X-3.75 I-3.75 E1
G1 Y3.75 E1
G1 X-5.75 E1
G3 Y-3.75 J-3.75 E1
G1 X-3.75 E1
G1 Y-5.75 E1
G3 X3.75 I3.75 E1
G1 Y-3.75 E1
G1 X5.75 E1
G3 Y3.75 J3.75 E1
G1 X3.75 E1
M761
G4 P50
G1 X2.75 Y2.75
M760
G1 F600
G4 P100
G1 Y5.75 E1
G3 X-2.75 I-2.75 E1
G1 Y2.75 E1
G1 X-5.75 E1
G3 Y-2.75 J-2.75 E1
G1 X-2.75 E1
G1 Y-5.75 E1
G3 X2.75 I2.75 E1
G1 Y-2.75 E1
G1 X5.75 E1
G3 Y2.75 J2.75 E1
G1 X2.75 E1
M761
G4 P50
G1 X1.75 Y1.75
M760
G1 F600
G4 P100
G1 Y5.75 E1
G3 X-1.75 I-1.75 E1
G1 Y1.75 E1
G1 X-5.75 E1
G3 Y-1.75 J-1.75 E1
G1 X-1.75 E1
G1 Y-5.75 E1
G3 X1.75 I1.75 E1
G1 Y-1.75 E1
G1 X5.75 E1
G3 Y1.75 J1.75 E1
G1 X1.75 E1
M761
G4 P50
G1 X0.75
M760
G1 F600
G4 P100
G1 Y4.75 E1
G1 X-0.75 E1
G1 Y1.75 E1
G1 X0.75 E1
M761
G4 P50
```

```
G1 X-1.75 Y0.75
M760
G1 F600
G4 P100
G1 X-4.75 E1
G1 Y-0.75 E1
G1 X-1.75 E1
G1 Y0.75 E1
M761
G4 P50
G1 Y-1.75 X-0.75
M760
G1 F600
G4 P100
G1 Y-4.75 E1
G1 X0.75 E1
G1 Y-1.75 E1
G1 X-0.75 E1
M761
G4 P50
G1 X1.75 Y-0.75
M760
G1 F600
G4 P100
G1 X4.75 E1
G1 Y0.75 E1
G1 X1.75 E1
G1 Y-0.75 E1
M761
G4 P50
;XXXXX LAYER END XXXXX
G1 Z10
M84
```

Code 4: Arduino Code for Bioreactor Docking Station

```
//Coded by Marius E. Gensler
//Version 29-06-2021

//Renaming and defining PINs
#define RotarySW 0
#define RotaryDT 1
#define RotaryCLK 2
#define StepperEnable 3
#define StepperM0 4
#define StepperM1 5
#define StepperM2 6
#define StepperReset 7
#define StepperSleep 8
#define StepperStep 9
#define StepperDir 10
#define Relay1 11
#define Relay2 12
#define Button 13

//Implementing libraries
#include <AccelStepper.h>
#include <Encoder.h>
#include <Wire.h>
#include <LiquidCrystal_I2C.h>

//Defining settings according to library
AccelStepper stepper = AccelStepper(1, StepperStep, StepperDir);
Encoder Enc(RotaryCLK, RotaryDT);
LiquidCrystal_I2C lcd(0x27, 16, 2);
```

```

//Defining variables
long oldValue;
long newValue;
float pumpSpeed;

//--------------------------------------------------------------
void setup()
{
 //Defining PIN Type
 pinMode(StepperEnable, OUTPUT);
 pinMode(StepperM0, OUTPUT);
 pinMode(StepperM1, OUTPUT);
 pinMode(StepperM2, OUTPUT);
 pinMode(StepperReset, OUTPUT);
 pinMode(StepperSleep, OUTPUT);
 pinMode(Relay1, OUTPUT);
 pinMode(Relay2, OUTPUT);
 pinMode(Button, INPUT_PULLUP);
 pinMode(RotarySW, INPUT_PULLUP);

 //Initial PIN state
 digitalWrite(StepperEnable, LOW);
 digitalWrite(StepperM0, LOW);
 digitalWrite(StepperM1, LOW);
 digitalWrite(StepperM2, HIGH);
 digitalWrite(StepperReset, HIGH);
 digitalWrite(StepperSleep, LOW);
 digitalWrite(Relay1, HIGH);
 digitalWrite(Relay2, HIGH);

 //Initial Motor Settings
 stepper.setMaxSpeed(20000);
 stepper.setSpeed(0);

 //Initializing LCD screen
 lcd.init();
 lcd.backlight();
 lcd.setCursor(0, 0);
 lcd.print("Mode:  PERFUSION");
 lcd.setCursor(0, 1);
 lcd.print("    0 U/min       ");

 Serial.begin(19200);
}

//--------------------------------------------------------------
void loop()
{
 //Run Motor
 stepper.setSpeed(pumpSpeed);
 stepper.runSpeed();

 //Adjusting PumpSpeed with RotaryEncoder
 newValue = Enc.read()/-4;
 if(newValue != oldValue)
 {
   ChangeSpeed();
 }

 //Start MediaExchange when Button is pressed
 if(digitalRead(Button) == LOW)
 {
  MediaExchange();
```

```
 }
}

//--------------------------------------------------------------------
void ChangeSpeed()
{
 //Change PumpSpeed according to Input
 oldValue = newValue;
 lcd.setCursor(0, 1);
 lcd.print("    ");
 lcd.print(newValue);
 lcd.print(" U/min         ");
 pumpSpeed = newValue*53.333;

 //SleepMode when Motor is not used (PowerManagement)
 if(newValue = 0)
 {
  digitalWrite(StepperSleep, LOW);
 }
 else
 {
  digitalWrite(StepperSleep, HIGH);
 }
}

//--------------------------------------------------------------------
void MediaExchange()
{
 //Activate Relay to start old Media Discharge
 digitalWrite(Relay1, LOW);
 lcd.setCursor(0, 0);
 lcd.print("Mode:  DISCHARGE");
 lcd.setCursor(0, 1);
 lcd.print("    running     ");

 //Run Motor to discharge old Media
 stepper.setCurrentPosition(0);
 stepper.moveTo(84200);
 stepper.setSpeed(26*53.333);
 while (stepper.currentPosition() != stepper.targetPosition())
 {
  stepper.runSpeedToPosition();
 }

 //Release Relay to end old Media Discharge
 digitalWrite(Relay1, HIGH);
 lcd.setCursor(0, 1);
 lcd.print("    complete    ");
 delay(1500);

 //Activate Relay to start new Media Refilling
 digitalWrite(Relay2, LOW);
 lcd.setCursor(0, 0);
 lcd.print("Mode:  REFILLING");
 lcd.setCursor(0, 1);
 lcd.print("    running     ");

 //Run Motor to discharge old Media
 stepper.setCurrentPosition(0);
 stepper.moveTo(84200);
 stepper.setSpeed(26*53.333);
 while (stepper.currentPosition() != stepper.targetPosition())
 {
  stepper.runSpeedToPosition();
```

```
 }

 //Release Relay to end new Media Refilling
 digitalWrite(Relay2, HIGH);
 lcd.setCursor(0, 1);
 lcd.print("    complete    ");
 delay(2000);

 //Return to Perfusion Screen
 lcd.setCursor(0, 0);
 lcd.print("Mode:  PERFUSION");
 lcd.setCursor(0, 1);
 lcd.print("    ");
 lcd.print(newValue);
 lcd.print(" U/min       ");
}
```

List of Figures & Tables

List of Figures

List of Tables

Own Publications

Marius Gensler and Anna Leikeim et al. “3D printing of bioreactors in tissue engineering: A generalised approach.” In: *PloS one* 15.11 (2020), e0242615. `DOI: 10.1371/journal.pone`

Acknowledgement

First of all I want to thank my first supervisor Prof. Dr.-Ing. Jan Hansmann for the comprehensive and instructive project in which I was able to conduct my dissertation the last few years. But also for the scientific mentoring at the chair of Tissue Engineering and Regenerative Medicine and his highly personalized and individual leadership during this time. Also I want to thank my second and third supervisors Prof. Dr.-Ing. Aldo R Boccaccini and Prof. Dr. med. Thomas Dandekar for their scientific support and their high valuable input and feedback during all those countless meetings and discussions.

Special thanks go to my direct cooperation partners within the SFB TRR225: Dr. Sahar Salehi, Susanne Heid and Claudia Müller for their hands-on mentality and team-spirit during the project and the direct lab support.
Sincere thanks also to Prof. Dr. Robert Luxenhofer and Lukas Hahn for providing me with their bioink and materials whenever needed, as well as the scientific feedback on the common results.

I am grateful for all those scientists and friends of the whole SFB TRR225-team. Even through Corona-times there always was a high team-sprit and support in any possible way. I happily remember all those project-meetings in Banz Monastery as long as they were possible.
Here I also want to thank the Deutsche Forschungsgesellschaft (DFG) for the funding of the project. Without this kind of support my work would not have been possible.

Greatest thanks to all the colleagues at TERM for the kind and close working relationship and atmosphere. Especially the lab automation and bioreactor people namely Thomas Schwarz, Lukas Königer, Mark Möllmann, Shahbaz Bandesha, Christoph Malkmus, Tobias Schmitz and Dahlia Mahdy did a great job in supporting me in technical and material related topics, as well as the support at the 3D printers and workshop-tasks.

I also want to thank my master and project-related students Tamara Finger, Miriam Komma, Rohan Chakraborty, Chukwudi Okerulu and Leon Volk for their cooperation during the past years and their eager to dive into something new.

Mein herzlichster und größter Dank gilt all Jenen, die sich, abseits von Beruf und Alltag, dazu entschieden haben einen Teil ihres Weges mit mir gemeinsam zu gehen. Danke, dass ihr die Farbe zu meinem sonst sterilen Laboralltag beigesteuert habt.

Jakob, Philipp und Sebastian - Seit vielen Jahren an meiner Seite habt ihr mich die letzten Abschnitte meines Lebens begleitet und geprägt. Ich bin wer ich heute bin vor allem durch euch. Danke für Alles bisher und für das was die Zukunft uns noch bringt.

Johanna und Christina - Egal ob es ein gemeinsamer Spieleabend, ein Glas Wein auf der Mainbrücke oder gemeinsame Kochaktionen waren, mit euch war jede gemeinsame Zeit ein ultimativer Motivations-Booster. Ganz besonderen Dank auch für eure mentale Unterstützung in den letzten Monaten.

Lorenz und Sebastian - Für all die befreienden Ausflüge in die Wildnis. Egal ob Ferún, Miradus oder der Süd-Deutsche Mischwald, mit euch gibt es immer frischen Wind in den Segeln. Und nicht zuletzt auch Danke für die endlosen Disskusionen und Gedankenspiele.

Tara, Wolfgang und Christoph - Für die bedingungslose Rückendeckung im Kampf, sowohl auf Papier als auch auf der Matte.
Außerdem Danke an Christoph für die Unterstützung und den Inupt in elektrotechnischen Belangen und bei der gemeinsamen Fehleranalyse zu sehr späten Stunden.

Ganz besonders Danken möchte ich meinen Eltern Wolfgang und Nicola und meiner Schwester Melina für eure immerwährende Unterstützung in allen Lebenslagen. Egal ob Hoch oder Tief, ihr seid meine letzte Bastion - mein doppelter Boden - wann immer nötig. Besonders in den letzten Monaten wart ihr mein physischer und psychischer, moralischer und motivierender Anker. Danke für eure Unterstützung!

Affidavit

I hereby confirm that my thesis entitled **Simultaneous printing of tissue and customized bioreactor** is the result of my own work. I did not receive any help or support from commercial consultants. All sources and / or materials applied are listed and specified in the thesis.

Furthermore, I confirm that this thesis has not yet been submitted as part of another examination process neither in identical nor in similar form.

97072 Würzburg, 02.02.2022

Place, Date *Signature*

Eidesstattliche Erklärung

Hiermit erkläre ich an Eides statt, Die Dissertation **Simultanes Drucken von Gewebe und angepasstem Bioreaktor** eigenständig, d.h. insbesondere selbstständig und ohne Hilfe eines kommerziellen Promotionsberaters, angefertigt und keine anderen als die von mir angegebenen Quellen und Hilfsmittel verwendet zu haben.

Ich erkläre außerdem, dass die Dissertation weder in gleicher noch in ähnlicher Form bereits in einem anderen Prüfungsverfahren vorgelegt wurde.

97072 Würzburg, 02.02.2022

Ort, Datum *Unterschrift*